WIND TURBINE WAKE CHARACTERIZATION WITH REMOTE SENSING AND COMPUTATIONAL FLUID DYNAMICS

by

MATTHEW LAWRENCE AITKEN

B.S., University of North Carolina, 2006

M.S., North Carolina State University, 2009

A thesis submitted to the

Faculty of the Graduate School of the

University of Colorado in partial fulfillment

of the requirement for the degree of

Doctor of Philosophy

Department of Physics

2014

This dissertation entitled:
Wind Turbine Wake Characterization with Remote Sensing and Computational Fluid Dynamics
written by Matthew Lawrence Aitken
has been approved for the Department of Physics

_____
Dr. Michael H. Ritzwoller

_____
Dr. Julie K. Lundquist

Date_____

The final copy of this dissertation has been examined by the signatories, and we find that both the content and the form meet acceptable presentation standards of scholarly work in the above mentioned discipline.

Abstract

Aitken, Matthew Lawrence (Ph.D., Physics)

Wind Turbine Wake Characterization with Remote Sensing and Computational Fluid Dynamics

Dissertation directed by Assistant Professor Julie K. Lundquist

Because of the dense arrays at most wind farms, the region of disturbed flow downstream of an individual turbine leads to reduced power production and increased structural loading for its leeward counterparts. Currently, wind farm wake modeling, and hence turbine layout optimization, suffer from an unacceptable degree of uncertainty, largely because of a lack of adequate experimental data for model verification. Accordingly, wake measurements were taken in two separate experiments, (1) using the ground-based High Resolution Doppler Lidar (HRDL) developed by the National Oceanic and Atmospheric Administration (NOAA) in the Turbine Wake and Inflow Characterization Study (TWICS) at the National Renewable Energy Laboratory (NREL), and (2) using nacelle-based long-range lidar at a wind farm in the western United States. The vantage point from the nacelle is favorable in that scans can more consistently transect the central part of the wake.

The work presented here outlines a set of quantitative procedures for determining critical parameters from these extensive datasets—such as the velocity deficit, the size of the wake boundary, and the location of the wake centerline—and the results are categorized by ambient wind speed, turbulence, and atmospheric stability. Despite specific reference to lidar, the methodology is general and can be applied to extract wake characteristics from other remote sensor datasets, as well as output from numerical simulations.

In an effort to help advance computational fluid dynamics (CFD) models of wind turbine wake dynamics, experimental results are compared to a large eddy simulation (LES) of a turbine operating in the stable boundary layer using the actuator disk parameterization in the Weather Research and Forecasting (WRF) Model. With the wake characteristics described above as metrics for model verification, the simulations show good agreement with the observations. Moreover, new features—namely rotor tilt and drag from the nacelle and tower—are added to the existing actuator disk framework in WRF. The inclusion of rotor tilt causes the vertical location of the wake center to shift upward, as confirmed by experimental measurements. Continued improvement to the actuator disk model in WRF will help lead to optimized turbine siting and controls at wind farms.

Dedication

To my family

דור הלך ודור בא והארץ לעולם עמדת

Je me souviens

Acknowledgments

No member of a crew is praised for the rugged individuality of his rowing.
–Ralph Waldo Emerson

I would like to start by thanking my adviser, Julie Lundquist, for her continuous guidance and support throughout my tenure at the University of Colorado. It would not be an exaggeration to say that this undertaking would have been impossible without her vision, leadership, and expertise. I am grateful to Michael Ritzwoller, Robert Banta, Judah Levine, and Dmitri Uzdensky for agreeing to serve on my committee and for their discerning commentary, which was instrumental in improving the text contained herein. Thanks also to my fellow students in the Lundquist group, particularly my officemates Brian Vanderwende and Michael Rhodes, for enduring frequent brainstorming sessions and for helping to shape my thinking in many areas.

I would also like to recognize NRG Systems, Inc.—and Evan Osler, in particular—for their technical support of the Windcube lidar. Special thanks also to the research group led by Gene Takle at Iowa State University (ISU) for their assistance in Iowa, and to both ISU and Jerry Hatfield of the National Laboratory for Agriculture and the Environment for supplying various flux station measurements.

It is my distinct honor to thank Yelena Pichugina, Alan Brewer, Raul Alvarez, and Scott Sandberg of the National Oceanic and Atmospheric Administration (NOAA)

for their efforts in collecting, processing, and interpreting the High-Resolution Doppler Lidar (HRDL) data from the Turbine Wake and Inflow Characterization Study (TWICS). Much credit goes to Kelley Hestmark, a recent graduate of the University of Colorado, for her assistance with the initial TWICS data analysis. I am also immensely grateful for the help of Balaji Rajagopalan from the University of Colorado, who graciously offered indispensable advice regarding parameter estimation and inverse problems. Many thanks also to Neil Kelley, formerly of the National Renewable Energy Laboratory (NREL), for helping to design TWICS and to Andrew Clifton at NREL for several valuable conversations along the way. The work presented here benefited tremendously from the keen scientific insight of both Branko Kosović at the National Center for Atmospheric Research (NCAR) and Jeffrey Mirocha at Lawrence Livermore National Laboratory (LLNL).

Regarding the nacelle-based lidar campaign, I wish to thank the wind farm operator for their generosity in collecting and sharing the data and for many helpful discussions during the analysis. The simulations corresponding to this experiment utilized the Janus supercomputer, which is supported by the National Science Foundation (award number CNS-0821794), the University of Colorado Boulder, the University of Colorado Denver, and the National Center for Atmospheric Research. The Janus supercomputer is operated by the University of Colorado Boulder. Support for the

work presented here was generously provided by the U.S. Department of Energy's Wind and Hydropower Technologies Program, under the direction of the Office of Energy Efficiency and Renewable Energy.

With the exception of my parents, nobody has had more of an outsize influence on my personal and professional development than my uncle, Ronald Rudolph, whose own example—along with my father's—helped to inspire my passion in cleantech and sustainability. His lending of *A Brief History of Time* by Stephen Hawking and *The Making of the Atomic Bomb* by Richard Rhodes served to initiate my original interest in physics. He also persuaded me to attend the University of Colorado and proceeded to introduce me to Julie, in addition to various other luminaries in the energy space. As a chip off the avuncular block, albeit an imperfect one, I am greatly indebted for his inspiration and unremitting encouragement.

Mom and Dad, thank you for always being there for me and for affording me both the ability and opportunity to choose my own path. I'd be lucky to be half the parents that you are. I am fortunate to have two brothers, Myles and Graham, who are the funniest and most genuinely pure-hearted people I know, and whose standard I constantly strive to follow. It gives me great pleasure to thank my grandparents for their endless support and sagacious advice throughout my life and academic career. Thanks so much to all of the wonderful and valuable friends I have made in Colorado—

Adam Kaufman, Brandon Ruzic, Lisa McCormick, Ian Jaray, Emily Leedom-Hearst, the poker crew, and so many others—for reminding me how to have fun and stay sane. And thank you, Dana, for your devoted care and for managing to somehow put up with me. Of the many discoveries during grad school, you were easily the best.

Contents

List of Tables

List of Figures

Chapter 1

Introduction: Climate Change and Energy

Everything needs to change, so everything can stay the same.
–Giuseppe Tomasi di Lampedusa

In this chapter, I aim to illuminate what has been termed the "super wicked" nature of the issues surrounding climate change (Levin et al. 2012), yet still inspire hope in practical solutions that will allow us to avoid its most dire consequences. In a deviation from standard scientific practice, I will occasionally include my own personal opinions, where appropriate. In addition to direct attributions, I would like to note that my perspective has been shaped by writers such as David Roberts of *Grist*, Paul Komor and Roger Pielke, Jr. of the University of Colorado, Michael Shellenberger and Ted Nordhaus of the Breakthrough Institute, Kevin Bullis of *MIT Technology Review*, Thomas Friedman, Eduardo Porter, Andy Revkin, and Matthew Wald of *The New York Times*, and many others. Moreover, with typical American arrogance, I will focus the discussion mainly on the United States, which, as the world's wealthiest country and second-largest emitter of greenhouse gases, has a moral obligation to lead when it comes to climate change mitigation and adaption. Nevertheless, there is an implicit

understanding that climate change is a *global* problem that requires engagement from multiple actors in all countries.

With these caveats in mind, let us begin by adopting the main conclusions reached in the Fourth Assessment Report (AR4) published by the Intergovernmental Panel on Climate Change (IPCC) in 2007, namely that (1) "warming of the climate system is unequivocal, as is now evident from observations of increases in global average air and ocean temperatures, widespread melting of snow and ice and rising global average sea level," (2) "most of the observed increase in global average temperatures since the mid-20th century is very likely due to the observed increase in anthropogenic greenhouse gas (GHG) concentrations," (3) "unmitigated climate change would, in the long term, be likely to exceed the capacity of natural, managed and human systems to adapt," and (4) "many impacts [of climate change] can be reduced, delayed or avoided by mitigation" (Pachauri and Reisinger 2007). There is no single solution to the adverse implications of climate change, but rather a large set of appropriate responses generally categorized by two distinct, yet complementary, strategies: mitigation—or protecting nature from society—and adaptation—or protecting society from nature (Stehr and von Storch 2005). In both areas, immediate and aggressive action is urgently needed to minimize the risk of severe climate change impacts.

Despite the paramount importance of adaptation, this introductory chapter will focus on mitigation, i.e., actions that limit the magnitude and rate of long-term global warming through the stabilization or reduction of atmospheric GHG concentrations. Amongst several climate change mitigation strategies—such as energy efficiency and conservation, advanced biofuels, forest management, landfill methane recovery, sustainable agricultural techniques, carbon dioxide removal, geoengineering, and population control—I shall concentrate specifically on the switch to low-carbon energy sources in the electricity sector, to provide context and justification for the wind energy research presented in subsequent chapters. An emphasis will be placed on renewable energy (in general, the phrase "renewable energy" here will tend to exclude hydroelectric), with tacit recognition that renewables are to be complemented by an extensive portfolio of technologies, including responsibly-produced natural gas, advanced nuclear power, energy storage, and the smart grid, among others.

Happily, most—if not all—of the costs associated with mitigation may be offset by supplementary benefits, such as improved public health and environmental quality as a result of reduced air and water pollution, increased energy security, reduced pressure on water resources and natural ecosystems, provision of modern energy services to populations currently without access, and job creation in a variety of sectors and at multiple skill levels. (Note that the best way to build support for action to combat

global warming may in fact be the emphasis of such tangible and immediate benefits for local communities, which provided the underpinning for early successes in the environmental movement, such as the Clean Air Act, the Clean Water Act, the Superfund Act, and the establishment of the Environmental Protection Agency itself.) By definition, renewables are inexhaustible (practically speaking), unlike finite resources such as coal and natural gas. Moreover, the adoption of renewable energy technologies would result in local tax revenue to support public services and in more stable energy prices because of reduced vulnerability to fossil fuel price fluctuations. The grid could potentially be more reliable and resilient because renewable energy systems tend to be distributed and modular, and therefore less prone to extensive failure than large, centralized power plants. Distributed renewables would also mean avoided investments in and energy losses from transmission (EPA 2011).

In addition to carbon dioxide, the combustion of fossil fuels results in the emission of sulfur oxides, nitrogen oxides, and particulates, harmful pollutants that contribute to a variety of public health and environmental problems, such as acid rain, smog, and other air quality concerns. Various other environmental problems, e.g. methane leakage and mining runoff, can be traced to fossil fuel extraction. The inequitable distribution of fossil fuels—Asia has 56 percent of the world's population but just 30 percent of total recoverable coal reserves, for example—has led to international

tensions and constraints on economic development in resource-scare nations. Many countries and regions are known to exhibit the so-called "resource curse," in which dependence on revenue from natural resources, particularly fossil fuels, results in a considerable decline in economic development and political freedom. While geographically limited of course, renewable "fuels," e.g. wind, sunlight, water, biomass, are much more evenly distributed than fossil fuels. Therefore, switching to renewables would reduce—although not eliminate—the problems associated with access to and availability of energy (Komor 2004).

Then again, there are several obstacles preventing the diffusion of clean energy technologies (cleantech), the most significant being cost and intermittency. Currently, no renewable energy technology can compete strictly on an economic basis with traditional energy sources, mainly because renewable energy is still an emerging industry and because the market has failed to internalize the hidden costs associated with fossil fuels. Accordingly, for a wholesale shift in generation to alternative energy sources, either (1) cleantech prices must decrease because of economies of scale or technological improvements from R&D, or (2) fossil fuels must become more expensive because of supply constraints or a price on carbon, whether via a carbon tax or cap-and-trade system. According to the most recent estimates, proved coal (gas) reserves—i.e., resources that are economically recoverable under existing conditions—are expected to

be sufficient for meeting about 110 (60) years of global demand (BP 2013). Because reserves may change as a result of new discoveries or technological advances and because consumption is not constant, there is considerable uncertainty in predicting the end of the fossil fuel age. Nevertheless, the fact remains that coal and natural gas reserves are unlikely to be depleted any time in the immediate future. (Alert readers may have noticed that petroleum, conspicuous by its absence, was intentionally excluded from the preceding discussion, as an insignificant fraction of electricity is generated from oil, especially in the United States.) Moreover, setting a meaningful price on carbon is likely to prove exceedingly difficult, at least in the near term. Voters and businesses, and therefore their elected (or purchased, as the case may be) representatives, have resisted, and almost certainly will continue to resist, measures designed to raise energy prices, especially if it means paying now to solve distant problems for the benefit of future generations and electorates.

Still, even if grid parity—the point at which the levelized *cost* of alternative energy sources (see Section 1.1.3) is less than or equal to that of power already on the grid—were realized, the inherent *value* of renewables is constrained by intermittency, an additional challenge that must be overcome through the development of economical energy storage technologies, improvements in weather forecasting, and integration of capacity over large regions. Furthermore, because renewable "fuels" are free, renewable

energy projects will still be more difficult to finance even at grid parity, owing to their comparatively higher upfront capital costs (Beck and Martinot 2004).

Unfortunately, most political efforts to date, on both the federal and international level, have fallen short of curbing growth in GHG emissions and encouraging sufficient deployment of renewable energy. As noted by the World Bank (2009), the existing "global regime has so far failed to spur countries to cooperate on research and development or to mobilize significant funding for the technology transfer and deployment needed for low-carbon development." Adopted in 1997, the Kyoto Protocol to the United Nations (UN) Framework Convention on Climate Change set binding international limits on the GHG emission of industrialized countries. Yet, because Kyoto did not require emission commitments from emerging economies—including larger countries such as China and India—the U.S. Senate, fearing serious harm to the domestic economy, failed to ratify the treaty. To date, the European Union Emission Trading Scheme (EU ETS)—created in response to Kyoto—has done little to curb emissions because an over-allocation of permits has depressed carbon prices, thereby providing little incentive to invest in cleaner technologies. Accordingly, Kyoto has failed to lower global emissions, which actually increased 25% in the dozen years after its ratification (World Bank 2009). The 2009 UN climate change conference in Copenhagen, intended to develop a wider-ranging successor to Kyoto, was an

unmitigated disaster, in which the collapse of negotiations yielded an inconsequential accord "taken note of" by the participating nations. And as evidenced by the failure of the U.S. Senate to pass the American Clean Energy and Security Act of 2009, which would have established a cap-and-trade system similar to the EU ETS, the passage of climate change legislation or a comprehensive national energy policy (or any other meaningful legislation, for that matter) is nearly impossible in today's deeply divided U.S. Congress.

There are several reasons for the lack of substantive action on climate to date. Power is concentrated in the hands of wealthy individuals and organizations with a vested interest in maintaining the status quo. (The author Upton Sinclair once proclaimed, "It is difficult to get a man to understand something when his salary depends upon his not understanding it.") The U.S. is paralyzed by political polarization and international climate negotiations by distrust and dysfunction. Human beings evolved to respond to immediate danger, and not incremental threats such as climate change. We are poor judges of risk, particularly over the long term. The ubiquitous availability of cheap fossil fuels is the foundation of the global economy, so switching to alternative energy sources will be neither quick nor easy. As noted by David Roberts of *Grist*, "we are stuck between the impossible and unthinkable" (Roberts 2013b), meaning that without ambitious action on a massive scale we are quite likely to face calamitous

consequences, and yet such action does not seem particularly plausible given the current state of affairs. To make matters worse, every year of delay in implementing measures to limit the global temperature rise to about 2 °C adds $500 billion to the cost of mitigation, according to estimates by the International Energy Agency (2009). Similarly, a recent study found that the transitional costs for keeping warming below 2 °C would be three times higher if efforts began in 2030 as opposed to 2015 (Luderer et al. 2013).

Yet, despite procrastination by the world at large, and the U.S. in particular, there has still been progress. Brilliant innovations and a marked shift in public opinion are by no means guaranteed, but there is still room for fierce, pragmatic optimism even in light of the many stumbling blocks, as I hope to demonstrate in the following sections. For example, carbon dioxide emissions in the United States are at a 20-year low and fell 12% in a span of just five years after peaking in 2007 as a result of fuel-switching (i.e., coal to gas), renewables, efficiency, and the recent recession (Zindler et al. 2013). In 2012, coal—easily the dirtiest source of energy—represented 37% of electricity generation in the U.S., down from a share of 52% in 1998 and 48% as recently as 2008 (U.S. Energy Information Administration 2013b). The eminently quotable Winston Churchill might as well have been speaking about climate change when he quipped, "the United States invariably does the right thing, after having exhausted every other alternative."

Although the division of this chapter into distinct sections would seem to indicate otherwise, the economic, political, and technological aspects of climate change mitigation are interdependent challenges with a large degree of overlap. Progress in any one area makes progress easier in the other two. As noted by David Roberts, "if clean energy technology becomes cheaper and more powerful, it broadens support for more ambitious policy; properly constructed policy can accelerate clean energy tech development and/or deployment, which in turn creates political constituencies; and sufficiently smart and powerful political constituencies can scare politicians and investors away from dirty energy and toward clean energy" (Roberts 2013a). Moreover, the ordering of these sections is no accident: fundamentally, the resistance to action on climate change is about money. To overcome this opposition, a sustained and persistent political movement is needed to push governments into developing policies that will accelerate the transition to inexpensive and sustainable energy systems. Careful triangulation and wishful thinking are not acceptable solutions. To paraphrase Andy Revkin of *The New York Times*, what we need is nothing short of an energy revolution.

1.1 Economics

If you want to understand opposition to climate action, follow the money.

–Paul Krugman

Negative externalities—the costs associated with economic activity incurred by uninvolved parties—often lead to market failures in which scarce resources are no longer efficiently allocated, thereby justifying the case for possible government intervention. Corrective measures may include taxes to discourage unwanted behavior or subsidies for alternative activities with fewer adverse effects. It is important to recognize that the externalities associated with the burning of fossil fuels, like all externalities, are reciprocal in nature: the emission of carbon and other pollutants is certainly harmful for a variety of reasons, but emitters are also penalized if pollution is prohibited. If actors were entirely rational and free from constraints, any such problem could technically be resolved through the negotiation of private agreements. However, because private negotiations are often impractical, especially in the case of large-scale environmental pollution, intervention by the state is the best (and really, only) way to achieve economically efficient outcomes (Coase 1960).

1.1.1 Market-based mechanisms

Because the free market has failed to internalize the social cost associated with GHG pollution, a price on carbon—either via a tax or cap-and-trade scheme—would be needed to create the financial incentive for consumers to switch to environmentally preferable energy technologies. A carbon tax imposes a direct fee on each unit of emissions; setting the proper tax level is crucial: too low and it is easier to simply opt

for paying the tax and continuing to pollute, but too high and economic growth may be severely constricted. By contrast, a cap-and-trade system sets a maximum level of pollution and distributes emissions permits among firms. After an initial allocation or auction, firms that need to produce more emissions must purchase permits from those that produce less. Effectively, buyers pay a charge for polluting, while sellers are rewarded for reducing emissions. Theoretically, emission reduction is achieved by firms that can do so most cheaply, and in this way, the price on carbon is established by the market (Goulder and Schein 2013).

As market-based mechanisms, both taxes and cap-and-trade schemes are generally regarded as more economically efficient than subsidies or command-and-control regulations in achieving environmental goals (Metcalf 2009). Both approaches are different means to the same end, at least hypothetically, with each characterized by its own advantages and disadvantages. A carbon tax provides certainty about emission prices, whereas cap-and-trade provides certainty about emission quantity. Historically, taxes have proved harder to enact, but would likely be easier to implement. A carbon tax raises revenues, which can be used to lower other taxes or to invest in cleantech R&D. Conversely, most emissions permits to date have been freely allocated, or grandfathered, to persuade firms to accept emissions controls (Taschini et al. 2013), leading to windfall profits and perhaps explaining the supposed political favorability of

cap-and-trade. [Note that a carbon tax may be more workable than conventional wisdom would indicate: Rex Tillerson, the chairman and chief executive of ExxonMobil, which previously funded organizations advocating climate change skepticism, threw his support behind a carbon tax of at least $20/ton (Mufson 2012).] One disadvantage of a carbon tax is that it is extraordinarily difficult to accurately measure the social costs of externalities and in turn determine the optimum tax level. And unlike a carbon tax, cap-and-trade inherently adjusts to inflation and swings in economic activity without additional legislative or regulatory action; for example, during recessions or periods of slow economic growth, the emissions cost automatically decreases under a cap-and-trade scheme. On the other hand, without a price floor or ceiling, the price of carbon may be subject to wild volatility—as has been the case with the EU ETS—making long-term planning difficult for businesses and reducing the incentive for behavioral change (Goulder and Schein 2013).

Political factors complicate the implementation of both approaches, in that the price of carbon will not be set at the most efficient level according to economic theory, but rather at a level that is politically feasible. Governments tend to write complex tax laws filled with loopholes and exemptions, and trading schemes are similarly subject to manipulation and profiteering by companies seeking to game the system. Moreover, both approaches suffer from the issue of additionality, i.e., whether emissions reductions

are attributable solely to the tax or cap, or to other factors, such as an economic recession (Bento et al. 2012). Nevertheless, imposing some sort of price on carbon is certainly preferable to the status quo.

In theory, this price, whether determined by a carbon tax or cap-and-trade system, would be equal to the so-called social cost of carbon (SCC), a measure of the benefits gained by avoided emissions. Typically, the SCC is stated in terms of a marginal cost, i.e., the cost (in dollars) of emitting an additional metric ton of carbon at a given point in time. Monetizing the benefits of environmental regulation is inherently difficult, especially when trying to determine the cost of damages well into the future. SCC estimates are determined using complex models encompassing various assumptions, choices, and value judgments about climate science, economics, and technological development. Not surprisingly, a review of over 100 studies found estimates of the SCC to be highly variable, ranging from $10 to $350 per metric ton, with a mean value of $43 and standard deviation of $83 per metric ton (Parry et al. 2007). Although certainly not an exact measure of climate change damages, the SCC can still be useful in assessing the benefits associated with emissions reductions.

While most studies roughly agree on the magnitude of climate change impacts, the discrepancy in SCC estimates stems largely from the assumed discount rate, which determines the present value of future benefits resulting from contemporary

investments. Usually, the rate is set somewhere between 3–6% to account for the fact that money is worth more today than tomorrow because people tend to get richer with time (*The Economist* 2006). Low rates give greater weight to future generations, while higher rates imply more uncertainty about the realization of future benefits, making funding for the project less likely. Low discount rates are sometimes used to justify the moral stance that our generation should do almost whatever it takes to eliminate GHG emissions (Stern 2006). On the other hand, high discount rates on the order of 5% or greater reflect a certain type of business-oriented logic, namely that spending to mitigate climate change should yield at least the same rate of return as any other capital investment. In other words, the SCC should represent the opportunity cost of alternative investments, such as education or healthcare. [The U.S. federal government currently estimates the SCC in 2015 as between $12 and $58 per metric ton in 2007 dollars, assuming discount rates of 5% and 2.5%, respectively (Interagency Working Group on Social Cost of Carbon 2013).] Given limited resources, the current state of politics, and recent history, this business logic is likely to prevail, at least in the foreseeable future, resulting in an accepted SCC value on the lower end of the spectrum, if anything (Porter 2013b).

Indeed, any determination of the SCC is subject to what Roger Pielke, Jr. has termed the iron law of climate policy: "when policies focused on economic growth

confront policies focused on emissions reductions, it is economic growth that will win out every time" (Pielke, Jr. 2010). Climate policies must be made compatible with economic growth as a precondition for their success; calls for austerity and sacrifice will, with limited exceptions, fall on deaf ears. People may be willing to pay some price for achieving emissions reductions, but they are only willing to go so far. Especially in the U.S., the iron law will likely limit the politically viable price on carbon and prevent complete internalization of the negative impacts of carbon emissions. Still, even a politically constrained carbon price could raise up to $60 billion in annual revenues to fund investment in cleantech innovation or otherwise subsidize the deployment of low-carbon energy technologies (Aldy et al. 2008).

1.1.2 Energy subsidies

In the absence of market-based control mechanisms, subsidization may be a more politically workable, yet less economically efficient, alternative. Subsidies support certain technologies which may not be the least expensive method for reducing external costs. For example, subsidies for wind and solar tend to reduce the price of energy and therefore increase demand and ultimately consumption, counteracting initiatives for energy efficiency. Moreover, subsidies effectively add to the deficit if the government does not raise taxes or reduce spending in other areas. With subsidies, the market could

also potentially be rewarded for decisions that may have been made independently (Kosmo 1987).

These drawbacks notwithstanding, the federal government has long provided financial support for the development and production of energy technologies in the form of tax preferences, grants, loan guarantees, and direct spending programs. Subsidies have been used to enhance national security by reducing dependence on foreign oil imports and to minimize environmental damage from energy consumption. From 1916 to 1970, federal energy tax policy was devoted almost entirely to increasing production from domestic oil and gas reserves, and there were no incentives promoting the use of renewables or energy efficiency. In light of large budget deficits, heightened awareness of environmental issues, and the oil crisis resulting from the embargo in 1973 and Iranian Revolution in 1979, tax preferences for fossil fuels were reduced and a number of incentives were implemented to promote alternative energy and efficiency. Nevertheless, the overwhelming majority of tax expenditures continued to benefit the oil and gas industry well into the 1980s, and most of the tax incentives for renewables enacted under the Energy Tax Act of 1978 were allowed to expire during the Reagan administration. Support for renewables was revived in the 1990s, however, with the Energy Policy Act of 1992 establishing a production tax credit (PTC) for electricity generated from wind and biomass. Unfortunately, the PTC has been allowed to expire

several times only to be extended again for a short period, leading to boom-and-bust cycles of aid and withdrawal (see Fig. 1.1). Currently, other clean energy technologies, such as solar, also enjoy temporary tax credits of their own, and the majority of federal incentives now go to renewables, although permanent tax provisions continue to benefit fossil fuels and nuclear (Sherlock 2011; Dinan and Webre 2012).

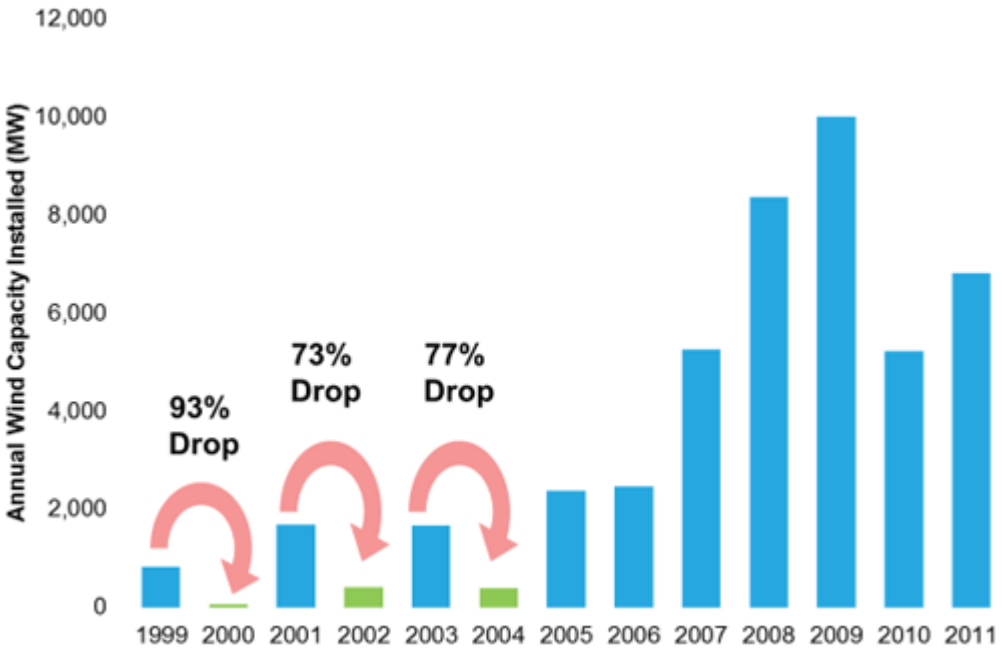

Fig 1.1. Historic impact of PTC expiration on annual U.S. wind installation. Source: American Wind Energy Association.

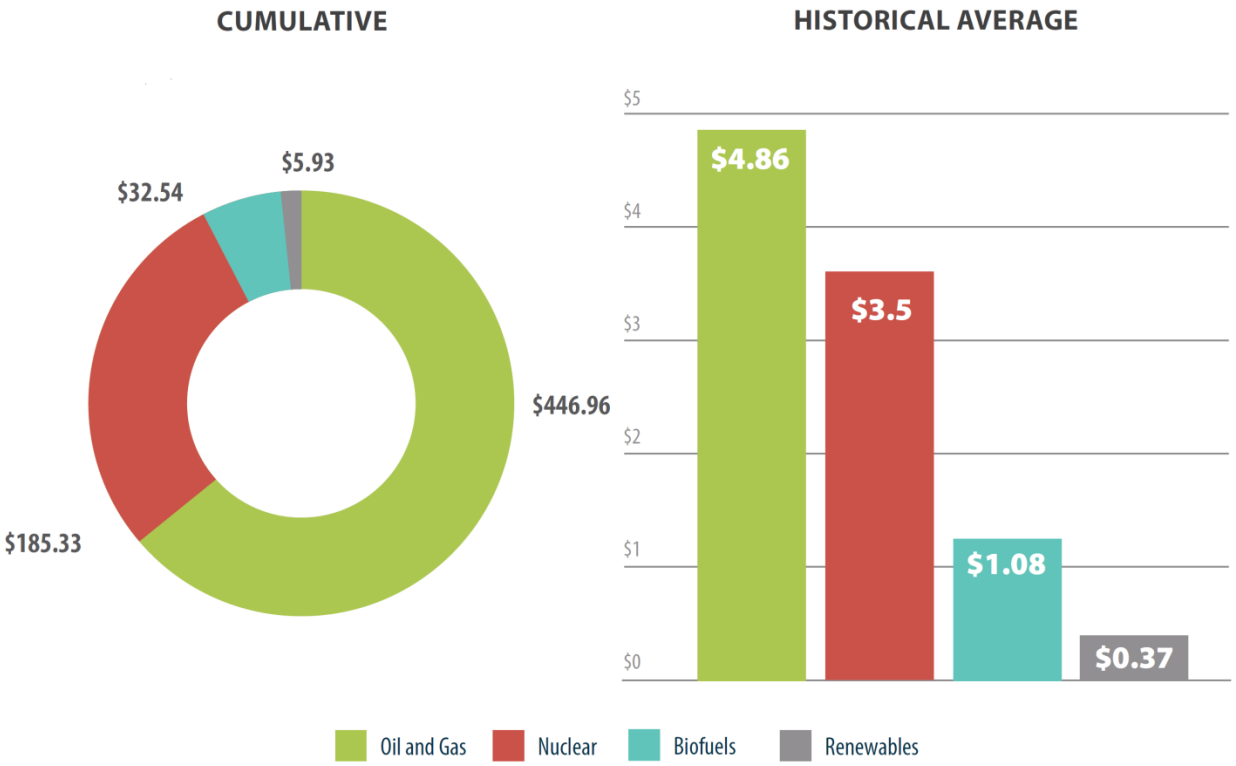

Fig. 1.2. Cumulative (left) and annual average (right) federal energy subsidies in billions of 2010 dollars since 1918. Reproduced from The Pew Charitable Trusts (2013).

Given historical support for conventional energy sources, then, cleantech subsidies therefore represent a shift in priorities and not an unprecedented intervention. Because the overwhelming majority of total tax incentives have gone to benefit fossil fuels, energy subsidies should be shifted away from mature and established industries toward the cleantech sector to help level the playing field. According to the International Energy Agency (2011), "subsidies in green energy technologies that are not yet competitive are justified in order to give an incentive to investing into technologies with clear environmental and energy security benefits." Rather than set at fixed

amounts with short time horizons, subsidies ought to last long enough to provide sufficient certainty for investments by the private sector—say, 5–10 years—and gradually phase out as renewables achieve cost competitiveness with conventional energy technologies. Well-designed policies should drive technological innovation and industry maturation to advance clean energy toward subsidy independence.

1.1.3 Achieving grid parity

Because subsidies cannot (and should not) last forever, renewables must succeed in a competitive market. A convenient measure for summarizing the overall competitiveness of various generating technologies is the levelized cost of energy (LCOE),

$$\text{LCOE} = \frac{\sum_{i=1}^{n}(I_i + M_i + F_i)(1+r)^{-i}}{\sum_{i=1}^{n} E_i(1+r)^{-i}}, \tag{1.1}$$

where I_i represents the investment expenditures in year i, M_i the operations and maintenance (O&M) expenditures in year i, F_i the fuel expenditures in year i, E_i the electricity generation in year i, r the discount rate, and n the lifetime of the system in years. For renewable technologies, which have no fuel costs and relatively small O&M costs, the LCOE is most sensitive to the overnight capital cost of generation capacity. On the other hand, fuel costs can significantly affect the LCOE for conventional generation sources, especially natural gas (U.S. Energy Information Administration 2013a). Table 1.1 lists the estimated U.S. average unsubsidized LCOE of new generation

resources for plants entering service in 2018 (a year chosen because of the long lead time for some technologies to come on line), while Table 1.2 denotes the regional variations in those levelized costs. Despite historically low natural gas prices, onshore wind is nearly cost-competitive with gas even without tax credits, making it perhaps the most promising renewable energy technology, at least in the near term. Still, substantial investment in R&D is needed for clean energy technologies to reach grid parity with conventional sources on an unsubsidized basis.

Table 1.1. Estimated average unsubsidized LCOE (2011 $/MWh) of new generation resources for plants entering service in 2018. Reprinted from U.S. Energy Information Administration (2013a).

Plant type	Capacity factor (%)	Capital cost	Fixed O&M	Variable O&M (including fuel)	Transmission investment	Total LCOE
Dispatchable technologies						
Coal	85	65.7	4.1	29.2	1.2	100.1
Natural gas combined cycle	87	15.8	1.7	48.4	1.2	67.1
Natural gas combustion turbine	30	44.2	2.7	80.0	3.4	130.3
Nuclear	90	83.4	11.6	12.3	1.1	108.4
Geothermal	92	76.2	12.0	0.0	1.4	89.6
Biomass	83	53.2	14.3	42.3	1.2	111.0
Non-dispatchable technologies						
Wind – onshore	34	70.3	13.1	0.0	3.2	86.6
Wind – offshore	37	193.4	22.4	0.0	5.7	221.5

Solar PV	25	130.4	9.9	0.0	4.0	144.3
Solar thermal	20	214.2	41.4	0.0	5.9	261.5
Hydro	52	78.1	4.1	6.1	2.0	90.3

Table 1.2. Regional variation in unsubsidized LCOE (2011 $/MWh) of new generation sources for plants entering service in 2018. Reprinted from U.S. Energy Information Administration (2013a).

Plant type	Minimum	Average	Maximum
Dispatchable technologies			
Coal	89.5	100.1	118.3
Natural gas – combined cycle	62.5	67.1	78.2
Natural gas – combustion turbine	104.0	130.3	149.8
Nuclear	104.4	108.4	115.3
Geothermal	81.4	89.6	100.3
Biomass	98.0	111.0	130.8
Non-dispatchable technologies			
Wind – onshore	73.5	86.6	99.8
Wind – offshore	183.0	221.5	294.7
Solar PV	112.5	144.3	224.4
Solar thermal	190.2	261.5	417.6
Hydro	58.4	90.3	149.2

It is important to note that direct comparison of LCOE across all technologies may be somewhat misleading, as plant investment decisions are affected by various regional characteristics, such as the existing load profile and resource mix. Another important consideration is power plant capacity factor, which is the ratio of actual energy output over a given time period to the maximum potential output were the plant

to operate continuously at full nameplate capacity. Because load must always be balanced to follow demand, dispatchable technologies with high capacity factors tend to be more valuable to a system than non-dispatchable ones that depend on the availability of intermittent resources. Moreover, utilities may pursue portfolio diversification because of the inherent uncertainty in future fuel prices, as well as tax credits and other policies. For these reasons, a perhaps more appropriate metric for economic decisions regarding capacity additions is avoided cost, or the cost a utility incurs to generate electricity that is otherwise displaced by a new generation project. A comparison of levelized cost and avoided cost indicates whether or not the value of project exceeds the cost; such comparisons can also be used to determine the most economical project amongst multiple technologies. Notably, in its most recent proposal to the Colorado Public Utility Commission, Xcel Energy identified 450 MW of wind and 170 MW of solar as the most cost-effective resources (including subsidies), representing the first time renewables were chosen strictly on an economic basis rather than to simply meet the state renewable portfolio standard (U.S. Energy Information Administration 2013a; LaMonica 2013).

Much progress has been made in recent years to drive down the cost of renewables, particularly wind and solar. Through economies of scale and research sponsored by the government and private sector, the (subsidized) price of wind has

plummeted by an order of magnitude in the past three decades, from $550/MWh in 1980 to about $50/MWh in 2012. Historically, wind power capacity in the United States has doubled about every 2.5 years. In 2012, wind energy became the primary source of newly added generation capacity in the U.S. for the first time, representing 43% of all new electric additions (Tillemann et al. 2013).

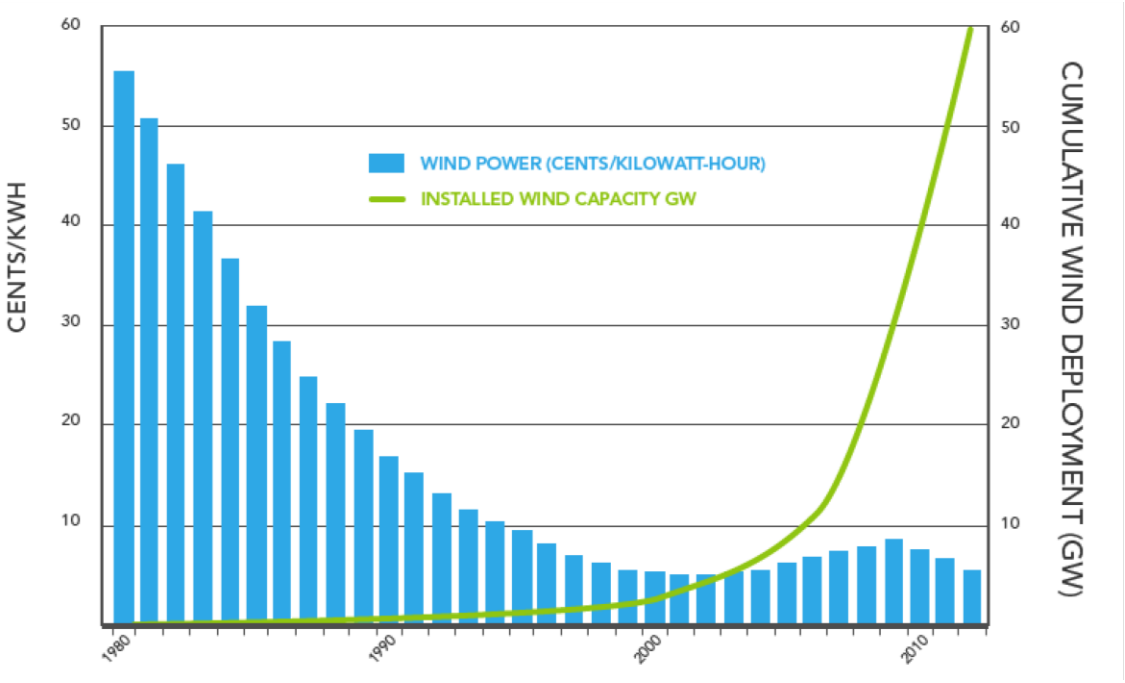

Fig 1.3. Deployment and cost of U.S. wind power 1980–2012. Reproduced from Tillemann et al. (2013).

Moreover, rooftop solar panels today cost about 1% of what they did 35 years ago, and in just the past five years alone, solar photovoltaic (PV) module prices have fallen from $3.40/W to $0.80/W. Similar to Moore's law for integrated circuits, Swanson's law says that solar PV module prices tend to drop 20% for every doubling of

cumulative shipped volume; effectively, solar prices are cut in half about every three years. There is also tremendous potential, particularly in the U.S., to bring down so-called balance-of-system (BOS) costs, which derive from permitting and installing solar PV systems. The U.S. Department of Energy SunShot Initiative aims to streamline building codes, zoning laws, permitting rules, and business processes for installing solar systems, in an effort to reduce BOS costs, which, at $3.34/W, are more than five times that in Germany. If recent price trends persist, wind and solar could reach grid parity by the end of this decade, if not before (Tillemann et al. 2013; Swanson 2006).

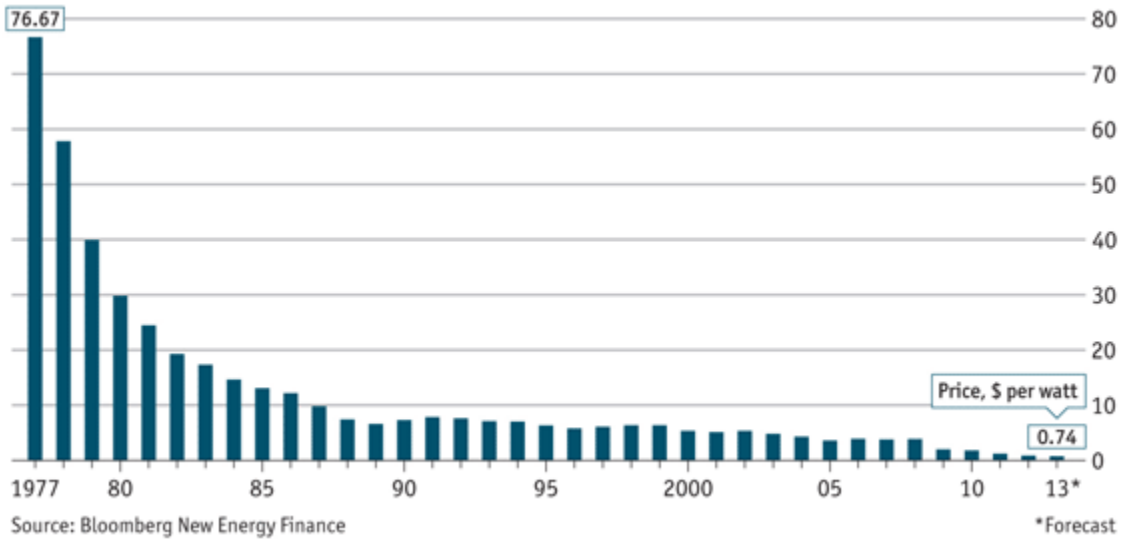

Fig 1.4. The Swanson effect: price of crystalline silicon photovoltaic cells in dollars per Watt. Reproduced from Carr (2012).

1.2 Policy

Men argue. Nature acts.

–Voltaire

In theory, the free market is the most powerful and efficient system for allocating resources because competition arising from aggregate supply and demand ensures that superior goods and services are provided to consumers at the lowest possible cost. However, even a perfunctory reading of history would show that the free market often fails to protect the well-being of the general public as well as that of the environment. Just a few examples of market failures include slavery; child labor; monopolies; the exploitation of workers via low wages, long hours, and hazardous labor conditions in the late 19th and early 20th centuries; ozone depletion; and pollution in general (Cowen 1988). The Stern Review on the Economics of Climate Change commissioned by the British government labeled climate change as the "greatest market failure the world has seen" (Stern 2006). Indeed, the uncertain and distant impacts of climate change are unlikely to significantly sway decision-making in the private sector, which is concerned, for the most part, with maximizing short-term profits.

Of course, government regulation is no more perfect than the free market, and centralized control can often lead to unintended consequences despite good intentions. Subsidies and other supportive policies reduce the incentive for cost reduction and are

inconsistent with the general trend in industrialized countries toward the restructuring of electricity markets. Moreover, subsidies reflect the outcome of political negotiations and not actual costs; improperly designed policies can lead to insufficient supply or windfall profits for producers. While helpful in initially scaling up nascent industries, subsidies are not sustainable over the long term, nor should they be. Market intervention can create dependent and powerful constituencies, and indefinite subsidies could lead to the perception of the cleantech industry as just another despised special interest (Komor 2004).

The key, then, is striking the right balance between free markets and regulatory oversight, allowing private business to flourish while still protecting public interests. As noted by Komor (2004), "There exists a natural tension between policy and markets—policy defined as explicit government actions in pursuit of a specific outcome, and markets defined as the functioning of a competitive and lightly regulated or unregulated economic system. The challenge for renewable energy policy is to devise policies that work with the market and intervene as little as possible while still successfully promoting the outcome of increased use of renewables. The ideal choice is not between one or the other, but rather the right spot on the continuum from complete central control to a totally unregulated market." Above all else, policy must be stable to provide

the certainty necessary for businesses to make long-term investments that will ultimately drive down costs.

It is also important to recognize that the electricity sector, as it exists today, is anything but a free market. The production, transmission, and distribution of electricity are already regulated in most countries, and most energy sources have long received subsidies in the form of R&D funding and direct tax credits (Komor 2004), as noted in Section 1.1.2. Programs to promote renewable energy technologies therefore represent a shift in priorities and not an unprecedented intervention. There are several possible policy approaches, each of which has its own strengths and weaknesses. With no clear single best option, a combination of mechanisms may in fact prove to be the most effective. Policies should help to create and support markets for renewable energy and should be tailored for individual technologies. For example, applied research and policies that stimulate deployment may be more suitable for fairly mature technologies, such as hydropower and onshore wind, whereas more basic R&D may prove more appropriate for less advanced or completely new technologies.

This point may be further illuminated by considering both the urgency and scale of mitigating climate change. To wit, fossil fuels are the bedrock of the modern global economy, but business-as-usual is likely to result in ruinous consequences. And there simply are not enough remaining resources to raise living standards for the billions of

people living in extreme poverty with fossil fuels alone. In light of this reality, we must quickly transition to scalable and sustainable energy systems, meeting the basic needs of the global population while simultaneously driving carbon emissions as close to zero as possible. While technically achievable with existing technologies, these technologies are still too expensive to be practical at large scale. Yet, we also do not have time to wait for completely new technological breakthroughs to be successfully commercialized. We must rapidly install existing technologies, while also improving those technologies and developing newer, better ones. We need both deployment *and* innovation.

To be fair, deployment policies may be effective yet inefficient, in that they result in considerable new renewable capacity, but potentially at a high cost to the consumer. Moreover, public investment in R&D is no panacea, as breakthrough technologies are impossible to predict in advance, especially by a central authority. This is not to say, however, that renewable energy policy has no place. Despite the disadvantages of government intervention, the cost of inaction would be far greater.

1.2.1 Public policy landscape

Similar to previous restructuring of the telecommunications and airline industries, the U.S. electricity sector has enjoyed increasing deregulation since the Energy Policy Act of 1992. Although still heavily regulated in much of the U.S., electricity markets in fifteen states and the District of Columbia have replaced a

monopoly system of utilities with competing sellers, the goal being to reduce both wholesale and retail electricity prices (U.S. Energy Information Administration 2013c). While the promotion of social or environmental goals may prove more difficult with reduced regulatory control, newly opened markets have allowed for differentiated retail products and branding opportunities for utilities.

In fact, electricity deregulation has paved the way for so-called green power marketing, in which renewable energy is sold in the competitive marketplace amongst multiple suppliers and service offerings. By allowing consumer preferences for environmentally preferred sources to be reflected in market transactions, green power marketing has the potential to expand the availability of those sources without governmental intrusion and despite cost considerations (Komor 2004). The voluntary renewable energy market in the U.S. more than tripled in size from 2006–2011, with total sales approaching 40 million MWh in 2011 (Heeter et al. 2012). However, even with surveys indicating 80% support for renewable energy, just one quarter of respondents would spend $5–10 extra each month to partially power their home with renewable energy. And only one in six consumers is aware of the green power options from their electricity provider, even though such options are available to almost one half of the population. In actuality, just 7% of the population reports buying at least some renewable energy for their home (Natural Marketing Institute 2011). With support for

environmental goals broad yet shallow, sound policy is essential for promoting cleantech deployment and driving down costs.

One of the more popular and successful policy approaches, especially in the U.S, has been the renewable portfolio standard (RPS), which establishes a compliance market by requiring utilities to provide a specified fraction of their electricity from renewable sources (Komor 2004). Colorado, for example, has one of the strongest RPS mandates in the country, in which 30% of electricity sales must derive from renewable generation by 2020. Portfolio standards are simple and enjoy extensive political support from environmentalists and free market enthusiasts alike; although there is no national clean energy standard, 30 states and the District of Columbia have adopted RPS mechanisms (DSIRE 2013). (Politicians often prefer regulations with obvious benefits and hidden costs to those with hidden benefits and obvious costs, perhaps explaining the attractiveness of this approach.) The RPS establishes a guaranteed demand for renewable electricity, while relying almost entirely on private markets for its implementation, leading to lower costs through competition, efficiency, and innovation. Cheaper technologies (e.g., wind) tend to be favored over more expensive ones (e.g., solar), which, depending on perspective, may be considered an advantage or disadvantage. To counteract this effect, some states include carve-outs in their RPS,

requiring that a small percentage of electricity be generated with specific technologies (DSIRE 2013).

Similarly, feed-in tariffs spur investment in clean energy technologies by requiring utilities to purchase electricity from renewable generators at a set price, guaranteed by a long-term contract (usually 15–20 years) and thus ensuring a reasonable rate of return. More common internationally, feed-in tariffs are mandated by law in just a handful of states in the U.S. (Komor 2004). Although well-designed feed-in tariffs have proved generally effective in promoting renewable energy in Europe, Spain suspended its feed-in tariff program for new projects in 2012 because excessively generous premiums led to far more investment than intended, and thus unmanageable costs for consumers (Wang 2012).

Additional policy approaches at the state level include the Regional Greenhouse Gas Initiative (RGGI), a cap and trade system established by nine northeastern states for reducing GHG emissions 10% below 1990 levels by 2020 (Holt et al. 2007). Twenty states and the District of Columbia have established long-term GHG emissions targets. In particular, an executive order issued by Governor Bill Ritter in 2008 sets the GHG emissions goal for the state of Colorado at 20% below 2005 levels by 2020 and 80% below 2005 levels by 2050 (EPA 2013). To help achieve this goal, the Clean Air–Clean Jobs Act passed in 2010 mandates the replacement of 900 MW of coal-based power

generation with facilities fueled by natural gas or other low-emitting sources by 2017 (Proctor 2012). In just one example of action at the municipal level, the city of Boulder has committed to adhere to the GHG emissions goals established by the Kyoto Protocol, and in 2006, Boulder voters passed the first tax in the U.S. exclusively designated for climate change mitigation. Moreover, the city council has called for reducing GHG emissions 80% by 2050 (City of Boulder 2013).

On the federal side, the Department of Energy has been authorized to offer more than $10 billion in loan guarantees for renewable energy, energy efficiency, and advanced transmission projects, in an effort to encourage early commercial use of new or significantly improved technologies. As mentioned in Section 1.1.2, several federal tax credits are also in place to support corporate investment in clean energy: a production tax credit (PTC) in the amount of 2.3 cents/kWh for wind, biomass, and geothermal and 1.1 cents/kWh for landfill gas, municipal solid waste, qualified hydroelectric, marine, and hydrokinetic energy; and also an investment tax credit (ITC) equal to 30% of expenditures for solar, fuel cells, and small wind and 10% for geothermal and combined heat and power (DSIRE 2013).

In the absence of comprehensive legislation from Congress on climate or clean energy, President Obama has directed the Environmental Protection Agency (EPA) to use its existing authorities under the Clean Air Act to develop GHG emission standards

for electricity generation. With the average gas (coal) plant emitting about 1200 (1800) pounds of carbon dioxide per MWh, EPA has proposed limiting new gas-fired (coal-fired) power plants to 1000 (1100) pounds of carbon dioxide per MWh. EPA is also scheduled to propose guidelines for existing generation facilities by June 2014 and to finalize them a year later (McCarthy 2013; Shear 2013). The rules are expected to effectively outlaw the construction of new coal-fired power plants and would likely require existing fossil fuel stations to install costly carbon capture and sequestration systems. In addition, President Obama's climate action plan unveiled in June 2013 "commits to expand major new and existing international initiatives, including bilateral initiatives with China, India, and other major emitting countries" for reducing GHG emissions (Executive Office of the President 2013). Although market-based mechanisms are generally considered to be more efficient than command-and-control regulation, the measures undertaken by the Obama White House are entirely justified and appropriate given current political gridlock—on both the domestic and international level—and the urgency of the climate crisis.

1.2.2 Politics and social change

Political power is the fulcrum upon which the lever of public policy rests. Top-down laws and regulations are frequently catalyzed by people working for change from the bottom up. From abolition to women's suffrage to civil rights to environmentalism

to marriage equality, history clearly demonstrates that social transformation is built upon a vibrant foundation of grassroots activism. The widespread shift to clean energy similarly depends on popular demand by a broad base of various constituencies—young people, colleges, cleantech companies, religious institutions, farmers and ranchers, utilities, businesses, the military, and environmental organizations. Auspiciously, in addition to advocacy by various environmental organizations to facilitate civic engagement and collective action—e.g., the National Resources Defense Council, 350.org, the Union of Concerned Scientists, the Sierra Club, Ceres, the Environmental Defense Fund, the Center for Climate and Energy Solutions, and Friends of the Earth—there is ample evidence of support for renewable energy among the general population.

For instance, six U.S. colleges and universities, along with several cities—including Seattle, San Francisco, Portland, and Boulder—and the United Church of Christ, have committed to pursue fossil fuel divestment (Fossil Free 2013). While unlikely to directly impact the valuation of financial markets, divestment does help to erode corporate reputations, raise public awareness, and build support for legislation. Moreover, freed up capital can be reinvested in energy efficiency measures and clean energy stocks (Ansar et al. 2013). Almost 700 schools are signatories to the American College and University Presidents' Climate Commitment (ACUPCC), which provides the higher education community with a framework for implementing carbon emission

reductions. In particular, my almae matres, the University of North Carolina and North Carolina State University, have climate action plans to achieve carbon neutrality by 2050, while the University of Colorado has committed to reducing carbon emissions 80% by that same year (ACUPCC 2013).

Such college initiatives reflect the views of young people in general: a poll conducted for the League of Conservation Voters found that three-quarters of Americans under the age of 35 have negative perceptions of climate change deniers and that four-fifths support President Obama's recently announced climate action plan. Even a majority of young Republicans would be less likely to vote for a politician who opposed the president's plan (Goldenburg 2013). In addition to shifting conservative values, the Global Climate Coalition (GCC)—a group of companies from the oil, automotive, and manufacturing industries which led an aggressive lobbying and public relations campaign to undermine the validity of climate science—disbanded in 2002, and many previously skeptical corporations have since changed their position. In fact, several major oil and automobile companies—including former members of the GCC, such as BP, General Motors, and Shell Oil—have partnered with the Center for Climate and Energy Solutions (C2ES) to actually back efforts for climate change mitigation (Revkin 2009). As eroded opposition from previously resistant groups leads to acquiescence and eventual support, the values behind social movements often become

unopposed elements of mainstream politics after prolonged struggles, and climate action seems to be following a similar course.

What is more, the World Business Council for Sustainable Development (WBCSD), an association of about 200 major multinational companies, advocates halving worldwide GHG emissions by 2050 based on 2005 levels (WBCSD 2013). Insurers, particularly the reinsurance companies that bear much of the ultimate risk in the industry, have taken a similar position (Porter 2013a). In its climate change policy statement, the trade group Reinsurance Association of America (RAA) notes that, "With a fundamental role in assisting individuals and businesses to manage risk, it is prudent for the insurance industry to acknowledge the changing climate as well as the risks it poses to all areas of its business. Furthermore, policymaking and corporate risk management strategies should include consideration of measures for adaptation to, and mitigation of, the potential adverse impacts of climate change" (RAA 2008).

Indeed, sustainability initiatives are becoming standard practice for some of the largest and most profitable companies in the world, with 60% of the Fortune 100 and Global 100 setting a renewable energy commitment, a GHG emissions reduction target, or both (David Gardiner & Associates 2012). Businesses may adopt clean energy and energy efficiency measures to reduce costs, increase return on investment, pursue branding opportunities, and avoid the uncertainty associated with volatile fossil fuel

prices. In just one example, Walmart has improved its fleet fuel efficiency by 69% since 2005 and reduced GHG emissions 13% between 2005 and 2010. Currently, 21% of Walmart's electricity is generated from renewable sources, and the company aims to eventually be supplied 100% by renewables. As the world's largest retailer, Walmart has also put pressure on its 100,000 suppliers to improve their environmental performance (Walmart 2013). In what is probably the most striking and noteworthy act of all in the business community, News Corporation—the parent company of Fox News Channel and *The Wall Street Journal* headed by the not-so-progressive Rupert Murdoch—achieved carbon neutrality in 2011 for the claimed benefit of its bottom line and corporate image (Rudolf 2011). (John Locke is well known for having claimed, "the actions of men are the best interpreters of their thoughts.") Of course, greenwashing—falsely spinning a perception of environmental friendliness—is a legitimate concern, and many supposedly green companies may donate money to political candidates who vote in opposition to environmental issues, yet trends still point towards increasing corporate sustainability and social responsibility.

Of the 126 teams in the five major professional sports—football, basketball, baseball, hockey, and soccer—38 use renewable energy for at least some of their needs and 68 have energy efficiency programs. Eighteen venues have installed solar panels, the most notable of which is Pocono Raceway, meeting 100% of its energy needs with an

onsite solar facility consisting of 40,000 solar panels. Lincoln Financial Field, the home of the Philadelphia Eagles, covers about 30% of its energy usage with 11,000 onsite solar panels and offsets the rest by purchasing renewable energy credits. The St. Louis Cardinals have reduced energy consumption at Busch Stadium by 24% in just three years, and the Seattle Mariners have realized $1 million in annual savings by decreasing energy use at Safeco Field. The sports industry is big business and one of the most culturally influential sectors in the country, with teams serving as role models for individuals and other businesses to emulate (Mihoces 2013).

As the largest single consumer of energy in the United States, the federal government is also leading by example to shape the energy landscape for the country as a whole. The Energy Policy Act of 2005 required federal agencies to obtain 7.5% of electricity from renewable energy sources by 2013. Executive Order 13423 signed by President Bush in 2007 requires federal agencies to reduce energy intensity 30% by 2015 as compared to 2003 levels. The Energy Independence and Security Act of 2007 mandates that new federal buildings and major renovations to existing buildings must be completely carbon-neutral by the year 2030. In 2009, President Obama signed Executive Order 13514, which, among a variety of sustainability goals, calls for reducing government GHG emissions 28% by 2020 as compared to 2008 levels (ACORE and AEE

2012). These government initiatives create substantial demand for clean energy technologies, helping to provide a vital anchor for the industry.

Similarly, with the capacity to make long-term investments and absorb large upfront capital costs, the military has a unique ability to create mass markets and drive innovation in cleantech. Viewing fossil fuel dependence as a strategic risk, the Department of Defense (DoD) is deeply committed to transforming its energy system. Protecting fuel convoys is one of the most dangerous jobs in the military, with one casualty for every 24 missions in Afghanistan in 2007. Moreover, volatile fuel prices make planning difficult and the cost of transporting gasoline into remote areas can be as high as $400 per gallon (Roberts 2012). By contrast, renewable energy offers concrete functional advantages for military operations by reducing supply chain vulnerability and eliminating commodity costs. In fact, the military has begun to adopt energy efficiency measures and renewable technologies, such as portable solar panels, in an effort to replace diesel generators that would ordinarily supply power to outposts, thus precluding the need for regular fuel convoys (Department of Defense 2010). DoD has committed to fulfill 25% of its energy needs with renewables by 2025, aiming to attract $7 billion in private sector investment over the next decade for the construction of renewable energy power plants. These types of strong public-private partnerships are crucial for the rapid deployment of cleantech at scale. As an early adopter, DoD can

help create a market for the next generation of technologies needed to support the nation's energy infrastructure, much in the same way it has served to catalyze the development of other fundamental innovations in the past, such as jet engines, GPS, microchips, and the Internet (ACORE and AEE 2012).

Moreover, the United States military, as an institution under civilian control in a representative democracy, is a reflection of domestic society as a whole. The armed forces represent the norms and values that a country seeks to project to the outside world. Because the military tends to be slightly more conservative than civilian society, changes to military culture are often indicative of deep-rooted progressive movements and inevitable societal transformation. Whether ending racial segregation as per President Truman's executive order in 1948 (Garamone 2008), authorizing full gender-integrated basic training in 1994 (Chapman 2008), openly integrating homosexuals in 2011, or allowing women to serve in combat roles starting in 2015 (CBS 2013), the evolution of values within the military has often mirrored broader changes in civilian customs. Furthermore, as one of the few remaining institutions to still receive bipartisan political support and the trust of the American populace, the military has inimitable potential to impact public opinion by championing clean energy. With advocacy of the military an almost sacrosanct principle in American politics, especially amongst

conservatives, general enthusiasm for conventional energy sources may begin to wane as the military's interests diverge away from fossil fuels and towards renewables.

1.3 Technology

We are like tenant farmers chopping down the fence around our house for fuel when we should be using nature's inexhaustible sources of energy—sun, wind, and tide. I'd put my money on the sun and solar energy. What a source of power! I hope we don't have to wait until oil and coal run out before we tackle that.

–Thomas Edison

In a practical sense, low-carbon energy sources will only be deployed at a meaningful scale once unsubsidized costs fall below that of fossil fuels. With stabilization of GHG concentrations requiring considerable reductions in global carbon intensity, there is tremendous need for expanded research and development in clean energy technologies. Unfortunately, worldwide public funding of energy research has been, for the most part, flat or declining for the past few decades and currently sits at about half of 1980 levels (Metz et al. 2007). U.S. energy R&D funding, in particular, averages just over $4 billion per year, far less than R&D investments in other areas popularly considered to be national priorities, such as health ($34 billion), defense ($81 billion), and space ($19 billion)—see Fig. 1.5. Numerous leaders, such as the President's Council of Advisors on Science and Technology and 34 Nobel laureates, have called for energy R&D funding to be doubled or even tripled above current levels (Jenkins et al.

2012). In a similar vein, the electricity sector, which is heavily regulated and capital intensive, also tends to avoid risk and innovation: utility spending on R&D averages just 0.1% of revenues compared to 3.5% for private firms across all industries (Augustine et al. 2011).

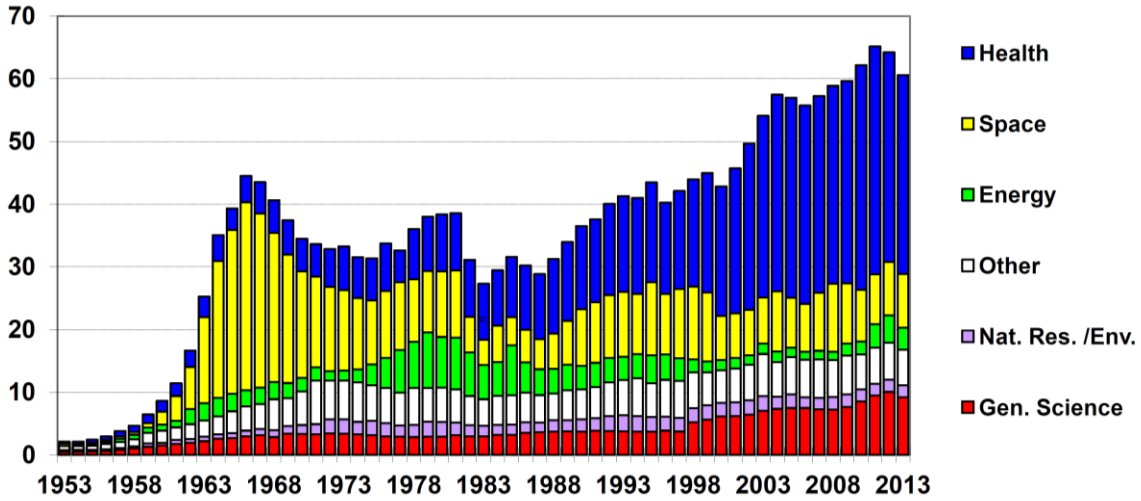

Fig. 1.5. History of U.S. R&D funding by function, in billions of 2012 dollars. Reprinted courtesy of the American Association for the Advancement of Science (AAAS).

With little incentive for privately financed research, then, public support for clean energy R&D is of paramount importance, especially in early stages. Direct government investments have fueled the development of various revolutionary technologies, such as interchangeable parts in manufacturing, railroads, hybrid crops, jet engines, microchips, the Internet, GPS, and many pharmaceutical drugs (Jenkins et al. 2010). Although certainly guilty of having backed its fair share of failures, most notably Solyndra, the government similarly has a long history of investing in cutting-edge

energy technologies. For example, initial demonstration of hydraulic fracturing in shale by DOE in the late 1970s and the federal production tax credit for unconventional gas from 1980–2002 helped spur the current shale gas bonanza (Shellenberger et al. 2012). Moreover, nuclear power was also developed with strong and consistent government support: the boiling water reactor was first demonstrated at Idaho National Laboratory and the pressurized water reactor at Oak Ridge National Laboratory. Financial incentives, such as loan guarantees and limitations on liability in the case of serious accidents, have served to further buoy the nuclear industry (Jenkins et al. 2010).

In terms of renewable energy, the Department of Energy invests in both incremental improvements to existing technologies and the development of more original innovations. The Office of Energy Efficiency and Renewable Energy (EERE) distributes funds for research to advance traditional clean energy sources, such as biomass, geothermal, hydropower, solar, and wind (EERE 2013). On the other hand, the Advanced Research Projects Agency-Energy (ARPA-E) is tasked with funding and commercializing transformational energy technologies that might not otherwise be pursued by industry because of a high risk of failure. ARPA-E helps bridge the valley of death—the funding gap between initial concept and working prototype—for a variety of clean energy technologies, from solid-state energy harvesting to carbon capture to power flow controllers. By nature, many of the ventures backed by ARPA-E will eventually

flop, but innovation often means a series of failures punctuated by occasional triumphs. As Winston Churchill said, "success is often nothing more than moving from one failure to the next with undiminished enthusiasm." To date, ARPA-E has funded almost 300 projects, five of which have generated spin-off companies or successful initial public offerings. A group of 11 projects have leveraged $39 million of ARPA-E funding into $200 million of private investment (ARPA-E 2013).

Barring unexpected breakthroughs, however, wind and solar are the two technologies poised for the biggest growth based on recent trends in volume and price. Although certainly geographically constrained, wind and solar resources are also far more ubiquitous than, say, geothermal and hydropower, for which most of the best sites have already been developed. With countless markets in which to grow, from rooftop to utility-scale generation, solar will most likely dominate over the long term owing to its modular nature. Solar has a unique advantage in that it can leverage improvements in other sectors—such as materials, computing, and nanotechnology—and solar generation also peaks at midday when energy demand is greatest. Still, a number of technological advances and steep cost reductions will need to be realized for solar to reach true grid parity. In the meantime, wind is the most cost-effective renewable energy technology and foremost challenger to fossil fuels. In fact, Jacobson (2009) placed wind first among nine electric power sources in a ranking of solutions to climate change, environmental

pollution, and energy security, with additional consideration given to impacts on water supply, land use, wildlife, and resource availability. Although revolutionary discoveries are unlikely at this point, further research is still required to improve efficiencies and drive down costs for wind to compete on an unsubsidized basis.

In addition to aerodynamic loads, electrical conversion and generation, grid integration, manufacturing, and materials, current R&D priorities for wind include resource characterization, turbine-to-turbine interactions at utility-scale wind farms, computational fluid dynamics (CFD) modeling, control systems, and forecasting. In particular, light detection and ranging (lidar), a remote sensing technology made increasingly viable with advances in optical fibers and other components by the telecommunications industry (Harris et al. 2006), has a broad array of applications in wind energy research. For example, the accuracy of numerical weather prediction models may be improved by assimilating lidar observations of wind speed and direction (Frehlich 2013). Moreover, the incorporation of lidar in turbine control systems is expected to both increase energy output and reduce structural fatigue damage (Harris et al. 2006). Compared to conventional techniques, resource assessment campaigns using laser anemometry reduce the uncertainty in annual energy production, thereby lowering borrowing costs and increasing the return on investment for wind farm developers (Boquet et al. 2010). Following a brief introduction to wind lidar, subsequent chapters

will focus specifically on the use of lidar measurements in wind turbine wake characterization and in CFD wake model verification, with the ultimate goal being to limit turbine-to-turbine interactions, thus optimizing plant power performance and minimizing the cost of energy.

Chapter 2

Wind Lidar Physics

You don't need a weatherman to know which way the wind blows.

–Bob Dylan

Developed in the 1960s shortly after the invention of the laser, light detection and ranging (lidar) has only recently become practical for widespread use in wind energy thanks to the improvement of laser and fiber optic technologies pioneered by the telecommunications industry over the past few decades (Cariou 2011). The following chapter serves to introduce the theory and principles of lidar operation to provide context for the applications presented in subsequent chapters.

2.1 The optical Doppler effect

The basis of wind lidar is the Doppler effect, whereby the speed of an object is determined by measuring the frequency shift between a transmitted and received wave. If the object does not move directly toward or away from the observer, then the measured speed is the component along the line-of-sight (LOS) connecting the observer and object. In particular, wind speed can be determined by reflecting electromagnetic radiation from particles advected by moving air masses, a process known as backscatter.

In the case of a monostatic lidar system, the relative frequency shift is proportional to u/c, the ratio of the wind speed u to the speed of light $c = 3 \times 10^8$ m s^{-1}. Because wind speeds near the surface of the Earth are on the order of 1–10 m s^{-1}, sophisticated techniques are required to accurately measure the Doppler shift of scattered radiation. Even in the case of powerful sources, the diffuse reflection due to scattering yields very weak return signals, which must be analyzed for both frequency and distance traveled (Werner 2005).

If the emitted light has frequency f_0 and the relative speed between the lidar transmitter and aerosol particle along the LOS is u, then the apparent frequency of the light on the aerosol particle is given by

$$f = f_0(1 + u/c). \tag{2.1}$$

The light is reemitted, or backscattered, at this frequency, and then is detected by the lidar receiver to be shifted to frequency

$$f = f_0(1 + 2u/c) \tag{2.2}$$

because the particle is moving while scattering. The wind velocity is usually defined such that movement toward (away from) the lidar leads to a positive (negative) frequency shift, and therefore positive (negative) LOS velocity (Werner 2005).

2.2 Lidar performance

Superimposed upon the collective movement of air masses are the random thermal motions of molecules and aerosols. At standard temperatures near the Earth's surface, the thermal velocity of molecules is widely distributed and, on average, much greater than typical wind speeds, owing to their relatively small mass. On the other hand, aerosol particles with higher masses and diameters on the order of 1–10 μm are characterized by narrow thermal velocity distributions with peaks several orders of magnitude below typical wind speeds. Relative to the widths of the respective distributions, the frequency shift of a lidar signal is much greater in the case of aerosol scattering, and therefore more amenable to measurement (see Fig. 2.1). Because the aerosol contribution to the return signal is better suited for frequency analysis, the choice of lidar wavelength λ depends not just on the expected magnitude of the return signal, but also on the expected ratio of aerosol-to-molecular backscatter. Whereas the molecular signal is proportional to λ^{-4}, the aerosol signal is proportional to something between λ^{-2} and λ^{-1}, depending on the chosen wavelength and particle properties. Thus, although the aerosol return generally decreases with increasing wavelength, higher wavelengths result in a more favorable aerosol-to-molecular backscatter ratio (Werner 2005).

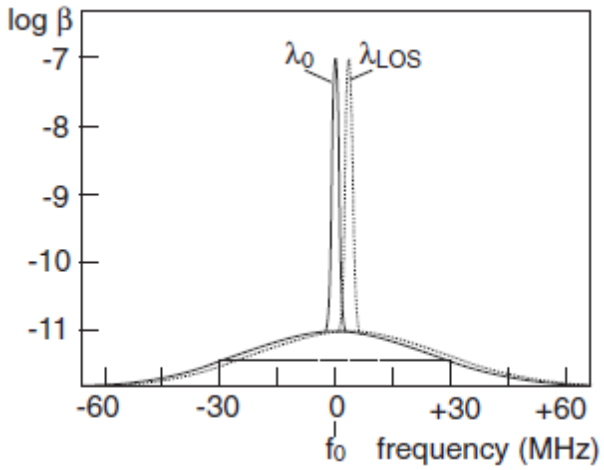

Fig. 2.1. Representation of an original (solid) and wind-shifted (dotted) frequency distribution. A narrow spike due to aerosols is superimposed upon the broad molecular peak. Reprinted from Werner (2005).

Consequently, wind lidar typically employs lasers operating in the near-infrared part of the spectrum at wavelengths between 1.4 and 2.2 μm. Whereas molecular number densities are mostly stable and uniform, aerosol concentration—and therefore aerosol backscatter—is much more variable, being influenced by weather, pollution, and other environmental factors (Fujii and Fukuchi 2005), as will be explored further in Chapter 3. Lidar performance is also affected by extinction, which is a function of both aerosol and molecular absorption and scattering and the concentration of these atmospheric constituents. Molecular absorption tends to be fairly negligible for wavelengths in the near infrared (Fujii and Fukuchi 2005).

Because the signal-to-noise ratio (SNR) is inversely proportional to the beam area, the lidar should be focused to minimize the beam diameter over the entire

measurement range to ensure the best possible accuracy. Atmospheric turbulence causes wave distortion that degrades heterodyne efficiency, and therefore the telescope aperture must be smaller than the coherence diameter of the beam, which limits the size of the telescope to about 10 cm at ground level in most areas (Cariou 2011). In coherent detection, which is described in the section below, noise originates from three sources: shot noise (statistical fluctuations due to the particle nature of light when the optical intensity is fairly low), detector noise (dark current, thermal noise, etc...) and relative intensity noise (RIN) resulting from the instability in the power level of the laser (Cariou 2011).

2.3 System architecture and measurement techniques

Although there exist several approaches for the remote optical measurement of wind speed, only pulsed Doppler lidar with coherent (or heterodyne) detection—being the method of choice in the work that follows—shall be elaborated here. In heterodyne detection, the return signal is mixed with that of a local oscillator (LO), and the resulting beat frequency is a measure of the Doppler shift. In general, heterodyne-detection lidar consists of a high-power pulsed transmitter laser (TE) with frequency f_0, a continuous-wave local oscillator with frequency f_{LO}, a locking loop (LL) connecting the two lasers, two heterodyne detectors in which the LO signal is mixed with the outgoing pulse (D1) and with the incoming return signal (D2), and signal processing system. A

schematic is shown in Fig. 2.2. Pulses are typically normally distributed and last on the order of several hundred nanoseconds. The return signal contains speckle resulting from constructive and destructive interference of waves scattered by randomly distributed particles in the atmosphere. Performance is improved by fixing the laser beam and accumulating the signal from several thousand shots to average out this speckle (Werner 2005).

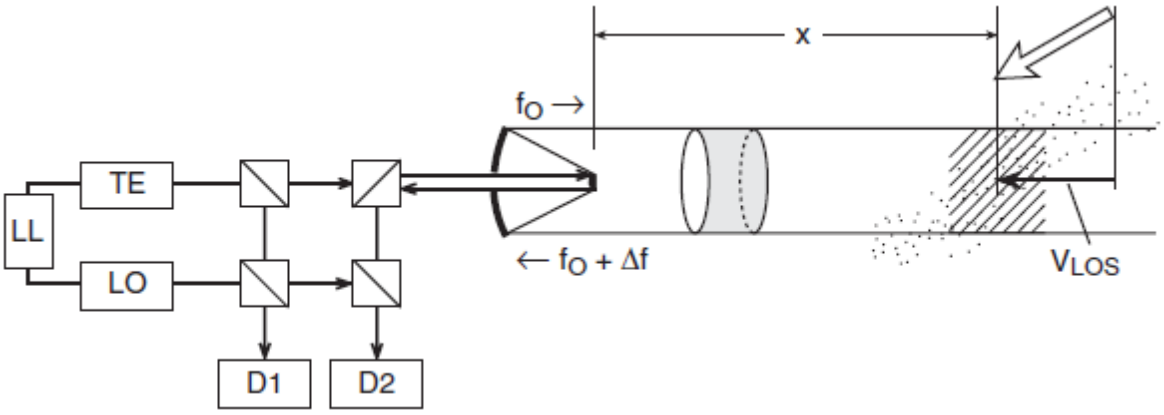

Fig. 2.2. Schematic of a heterodyne-detection Doppler lidar. Reprinted from Werner (2005).

To distinguish the difference between positive and negative Doppler shifts, an offset, or intermediate, frequency f_i is added to the LO signal: $f_{\text{beat}} = |f - (f_0 + f_i)| = |(f_0 + \Delta f) - (f_0 + f_i)| = |\Delta f - f_i|$, such that $\Delta f = f_i \pm f_{\text{beat}}$. Note that without the offset frequency, the beat frequency would be equal to the absolute value of the Doppler shift Δf, precluding the determination of the sign of the LOS velocity. The maximum downshift is limited by the value of f_i since negative frequencies obviously cannot be

measured, while the maximum upshift is limited by the Nyquist frequency, equal to one-half the sampling frequency of the signal processing system (Cariou 2011).

2.4 Scanning techniques and vector wind estimation

By assuming homogeneity of the wind field over the sensed volume, the three-dimensional wind vector can be inferred by employing appropriate scanning techniques with a single lidar. (Of course, the most accurate approach for obtaining a vector wind measurement is to view a given point in space from at least three directions, although the use of multiple lidar systems is often impractical because of cost and other logistics.) For example, the velocity-azimuth display (VAD) technique involves taking many measurements at very fine azimuthal resolution while scanning the beam in a conical fashion, as depicted in the lower part of Fig. 2.3.

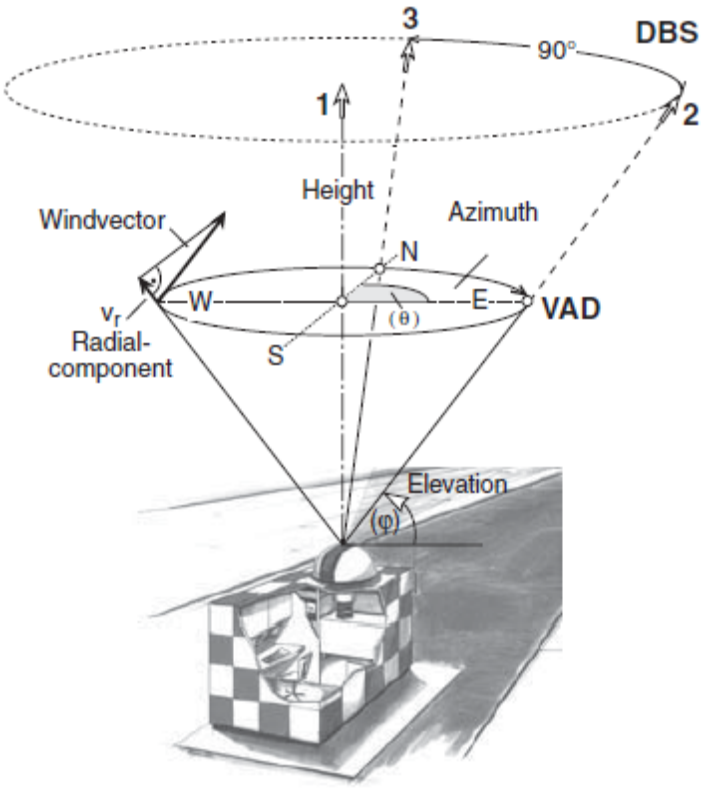

Fig. 2.3. Schematic of Doppler lidar scanning techniques. Reprinted from Werner (2005).

Fig. 2.4 shows an example of the LOS velocity signal for a particular range gate plotted as a function of azimuth angle. In the case of a homogenous atmosphere, the measurements approximate a sinusoid because only the LOS component of the flow is resolved by the lidar at each point in space.

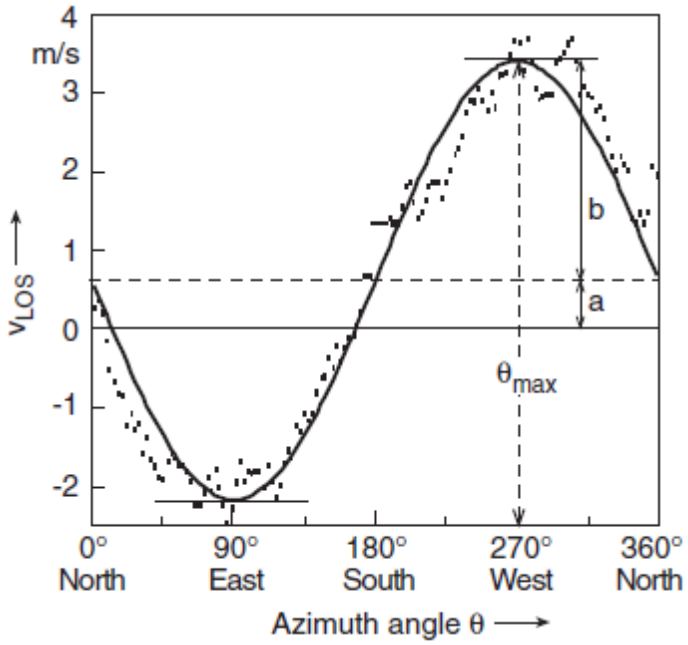

Fig. 2.4. Example fit to LOS velocity measurements for the determination of wind speed and direction. Reprinted from Werner (2005).

Assuming homogeneity, the LOS measurement is given by

$$u_{\mathrm{LOS}} = -u \sin\theta \cos\phi - v \cos\theta \cos\phi - w \sin\phi \,, \tag{2.3}$$

where u is the west-east component of the wind vector, v is the south-north component, w is the vertical component, ϑ is the azimuth angle of the beam measured clockwise from north, and φ is the elevation angle of the beam. By fitting a function of the form

$$u_{\mathrm{LOS}} = a + b\cos(\theta - \theta_0) \,, \tag{2.4}$$

the three-dimensional wind vector is obtained as

$$\mathbf{u} = (u, v, w) = (-b \sin\theta_0 / \cos\phi, -b \cos\theta_0 / \cos\phi, -a / \sin\phi) \,, \tag{2.5}$$

yielding the horizontal wind speed $(u^2 + v^2)^{1/2} = b/\cos\varphi$ and horizontal wind direction ϑ_0. A separate fit is performed for each range gate so that the wind speed and direction

may be calculated at multiple height intervals. The goodness-of-fit of the statistical model depends not only on instrumental parameters—such as the pulse repetition frequency and pulse width—but also on environmental factors such as turbulence, surface roughness, and atmospheric stability (Werner 2005).

At least three independent LOS velocity measurements are necessary for constructing the three-dimensional wind vector from a conical scan. As opposed to the VAD technique, Doppler beam swinging (DBS) involves the use of a small number of measurements (3–4 perhaps) in each scan. The DBS scan in Fig. 2.3, for example, shows two measurements separated by 90° in azimuth, along with a third along the vertical (Werner 2005). (The vertically-profiling Windcube lidar designed by Leosphere and used in Chapters 3 and 4 takes four measurements at azimuthal intervals of 90°.) For both VAD and DBS scans, the choice for the elevation angle of the beam is a tradeoff between accuracy and homogeneity. The assumption of a uniform wind field—which is also important for the detection of wind turbine wakes, as discussed in later chapters—is more valid the narrower the cone, yet the projection of the wind vector along each beam is less representative of the actual flow since the wind is usually more or less horizontal (Cariou 2011).

2.5 Measurement resolution and precision

In pulsed systems, the laser delivers cyclic bursts of high energy whose duration Δt determines the spatial resolution. The delay between the transmitted and backscattered pulses from an object at range r is given by $t = 2r/c$. Differentiating this equation shows that the minimum discernible depth interval is $\Delta r = \mathrm{c}\Delta t/2$. With pulse durations of some several hundred nanoseconds, spatial resolution is typically on the order of 10–100 m. Ideally, the pulse repetition frequency should be as high as possible, but the time between pulses must be at least the round trip time of flight to and from the maximum range of the instrument, to avoid ambiguity between successive return signals (Cariou 2011).

The precision with which the frequency, and therefore velocity, can be measured is a function of the backscattered power collected by the receiver, which depends on various instrument and environmental parameters, such as optical efficiency, pulse energy, aperture size, target range, atmospheric extinction, aerosol concentration, and number of averaged shots N. In a well-designed receiver, the SNR approaches the quantum limit governed by fluctuations in the signal itself (Fujii and Fukuchi 2005). Assuming that the time for which the backscatter from an ensemble of atmospheric aerosol particles remains coherent is infinite, the minimum velocity precision for a lidar of wavelength λ is given by the Cramér-Rao lower bound (CRLB)

$$\sigma_{\mathrm{CRLB}} = \frac{\lambda}{2\Delta t \mathrm{SNR}} \sqrt{\frac{2(1+\mathrm{SNR})}{N}}. \tag{2.6}$$

In an actual lidar, additional uncertainty arises from the finite correlation time τ_c

$$\sigma_{sat} = \frac{\lambda}{2\sqrt{N} 4\pi\tau_c}, \tag{2.7}$$

such that the total velocity precision is

$$\sigma = \sqrt{\sigma_{\mathrm{CRLB}}^2 + \sigma_{sat}^2}. \tag{2.8}$$

The CRLB is used in Chapter 4 to determine the velocity precision of the High Resolution Doppler Lidar (HRDL) developed by the National Oceanic and Atmospheric Administration (NOAA). In the chapter that follows, we examine the performance of the commercially-available Windcube lidar and the corresponding relevance to wind energy.

Chapter 3

Wind Lidar Performance

If we knew what it was we were doing, it wouldn't be called "research," would it?
–Albert Einstein

3.1 Introduction

The importance of reliable vertical wind profiles for both resource assessment and evaluation of turbine performance continues to rise with the rapidly escalating use of wind power in both domestic and worldwide energy production. Meteorological towers used to collect wind data, however, are usually constructed no higher than 60 m in the United States for reasons concerning structural stability, cost, and zoning regulations. With hub heights of 80 to 100 m and rotor diameters of 80 m or more, modern wind turbines are so tall that *in situ* instrumentation mounted on met towers can rarely probe the atmosphere across even the lower half of the rotor disk. And while turbine nacelles may be equipped with cup and sonic anemometry, hub-height point measurements are not representative of the wind speeds over the entire swept area of the rotor (Wagner et al. 2009). As a result, remote sensing techniques, such as lidar and sodar, will play an increasingly prominent role in the measurement of atmospheric

conditions at wind farms. In particular, the Leosphere Windcube, a pulsed coherent Doppler wind lidar, is capable of measuring wind speeds within a claimed uncertainty of 0.1 m s^{-1} at ten different altitudes greater than 40 m above ground level (AGL). Yet the availability of wind speed measurements, quantified by the carrier-to-noise ratio (CNR) of the instrument, is dependent upon weather conditions such as aerosol backscatter, turbulence, humidity, and precipitation. By examining the impact of these four parameters on CNR, this work presented here aims to determine the most appropriate circumstances for implementing wind lidar in the assessment of turbine performance. Despite particular reference to the Windcube, the results presented here may serve to guide characterization of other lidar systems, such as Natural Power's ZephIR and SgurrEnergy's Galion, as well.

3.2 Background and previous work

In optical remote sensing, it is possible to image features on the order of the signal wavelength or larger. Typically operating in the visible or near-infrared range, lidar is highly sensitive to aerosols and has many applications in atmospheric research and meteorology. Wind lidar, in particular, relies on deflection by small airborne objects, a process known as backscattering. In coherent detection lidar, e.g. the Windcube, a portion of the scattered radiation is collected by the lidar receiver, and the returned signal is mixed with a local oscillator beam and then detected with a

photodetector. The resulting beat signal is a radio frequency (RF) photocurrent whose frequency is a direct measure of the Doppler shift, which in turn is used to calculate wind speed. Lidar data availability is specified by CNR, defined as the ratio of the mean RF signal power to the mean noise power (Fujii and Fukuchi 2005). In the case of very weak signal strength, velocity estimates are dominated by random outliers and consequently subject to significant estimation error. If CNR falls below a pre-determined threshold, the uncertainty in the velocity estimate is deemed too large for the data to be useful and no measurement is recorded (Frehlich 1996). For example, the Windcube automatically disregards all measurements for which CNR is less than -22 dB, although this default setting may be adjusted in the expert version of the controlling software. Henceforth, Windcube data is considered to be "available" if CNR is greater than -22 dB. Schematics and details concerning Windcube operation can be found in brochures published by the manufacturer, available at http://www.leosphere.com/file/leosphere_windcube.pdf and http://www.lidarwindtechnologies.com/pdf/windcube.pdf.

Neglecting the loss due to atmospheric refractive turbulence, the parameter dependence of coherent lidar CNR is derived from the lidar equation in Fujii and Fukuchi (2005)

$$\mathrm{CNR} = \eta \frac{T^2 E_x}{h\nu B} \frac{c\beta}{2} \frac{A_r}{R^2} \tag{3.1}$$

where η represents an overall efficiency factor, T is atmospheric extinction, E_x is laser pulse energy, h is Planck's constant, ν is the transmitted laser beam frequency, B is the receiver noise-equivalent bandwidth, c is the speed of light, β is backscatter coefficient as measured by the lidar, A_r is aperture area, and R is target range. The collection efficiency of a coherent focused lidar, such as the Windcube, is maximized for scattering at the focus point and falls off with distance as the target is moved away from this location. Although UV (infrared) extinction may be dominated by ozone (carbon dioxide and water vapor) absorption, extinction is much weaker at selected infrared wavelengths—the wavelength of the Windcube laser is 1.54 μm, for example—that avoid molecular absorption features. In fact, the one-way near-infrared extinction is on the order of 0.2 dB km^{-1} in the planetary boundary layer (Fujii and Fukuchi 2005). At a given height, then, Windcube CNR is expected to be linearly proportional to aerosol backscatter since all other parameters are approximately constant.

While extinction due to molecular absorption is mostly negligible, the additional loss due to refractive turbulence can be quite severe. The reduction factor ψ is defined as the ratio of CNR in the presence of turbulence to CNR in the absence of turbulence. Yura (1979) found that, for a focused coaxial system, the reduction factor is given by

$$\psi = \left[1 + \left(\frac{a_2}{\rho_R}\right)^2\right]^{-1} \tag{3.2}$$

where a_2 is the $1/e^2$ intensity radius (the distance at which the beam intensity has dropped by a factor of $1/e^2$ from its center value) and ρ_R is the round-trip coherence length, defined as

$$\rho_R = 0.627(k^2 C_n^2 z)^{-3/5} \tag{3.3}$$

for uniform turbulence conditions. Here, k is the wavenumber of the signal, C_n^2 is the refractive index structure parameter, and z is propagation distance. High values of C_n^2 on the order of 10^{-13} to 10^{-12} $m^{-2/3}$ are indicative of a strongly turbulent atmosphere; for lower values on the order of 10^{-16} to 10^{-15} $m^{-2/3}$, atmospheric optical turbulence is considered negligible over optical paths of less than 2 km (Tunick 2003). Fig. 3.1 shows the theoretical reduction factor vs. C_n^2 for the Windcube at 40 m AGL. Although nearly unaffected for weak and moderate turbulence levels, CNR can be reduced by 20 to 80 percent in the strong turbulence regime.

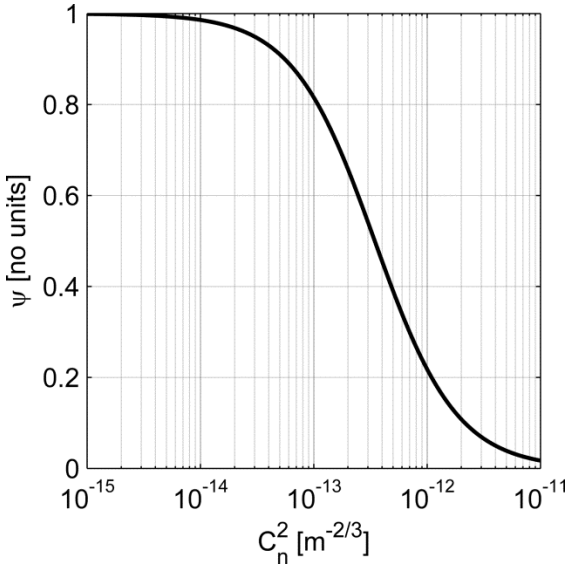

Fig. 3.1. Theoretical estimate of CNR reduction factor vs. C_n^2 for the Windcube at 40 m AGL; see Eqs. (3.2) and (3.3).

Aerosol scattering is a complex function of refractive index and particle size, both of which depend on relative humidity (RH). Although the refractive index tends to decrease with increasing humidity, this effect is small and is dominated by the swelling of hygroscopic particles near the saturation point. Wulfmeyer and Feingold (2000) found that scattering remains nearly constant for low to moderate levels of humidity and increases rapidly for RH > 0.8. It is also possible for the lidar signal to scatter from water droplets, enhancing CNR during precipitation events but also causing a false indication of vertical wind speed.

In summary, the primary atmospheric conditions expected to influence CNR, and thus lidar performance, are aerosol backscatter, atmospheric refractive turbulence, relative humidity, and precipitation. The effects of each are examined using the two datasets described in the following section; observations are presented in Section 3.4.

3.3 Data and methods

A Windcube lidar was deployed in late summer 2010 as part of the Skywatch Observatory, a set of meteorological instruments on the roof (approximately 15 m AGL) of the Duane Physics building at the University of Colorado at Boulder, elevation 1663 m. Backscatter was measured at a vertical resolution of 10 m from ground level to 7690

m AGL using a Vaisala CL31 ceilometer, which has an operational wavelength of 910 nm and was also located on the roof, approximately 5 m east of the Windcube. Similar to the Windcube, the ceilometer consists of a vertically-pointing laser and a co-located receiver. Short laser pulses are sent through the atmosphere, and a small component of the light is scattered by aerosols, water droplets, and low-level clouds and then returned to the receiver. The strength of the returned signal is recorded and its timing is transformed into a spatial range using the speed of light, thus producing a vertical profile of backscatter within the atmosphere. Measurements of lidar CNR and ceilometer backscatter were collected at heights of 40, 50, 60, 80, 100, 120, 140, 160, 180, and 200 m throughout August 2010; see Fig. 3.2. (Please note that all further references to backscatter measurements should be understood to come from the ceilometer.) Lidar and ceilometer data were taken at rates of 1 Hz and 0.0625 Hz, respectively, and then averaged over two-minute intervals for comparison.

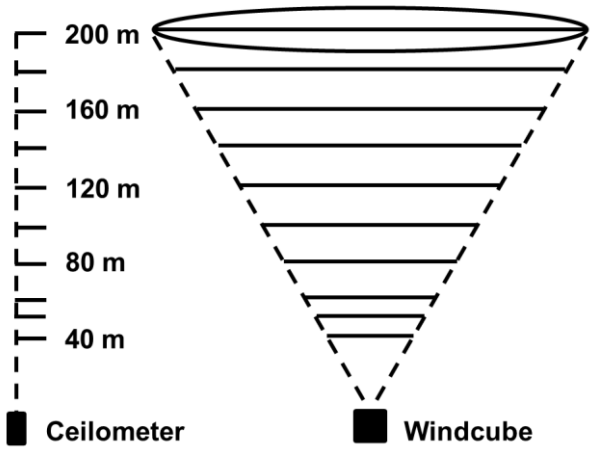

Fig. 3.2. Measurement heights for the experimental setup in Boulder. Dashed lines indicate laser beam directions, while solid lines indicate altitudes at which measurements were collected.

In addition, a second dataset was collected with the Windcube at the same altitudes during a deployment at a wind farm in central Iowa in late June and early July 2010. A flux station 142 m due west of the Windcube collected measurements of wind speed, temperature, and absolute humidity at 20 Hz. Wind speed and temperature were measured at 6.45 m AGL with a Campbell Scientific CSAT3 sonic anemometer, while absolute humidity measurements were collected by a LI-COR LI-7500 gas analyzer at this same height. Precipitation and relative humidity were also measured at this same flux station with a Campbell Scientific TE525 tipping bucket rain gauge at 3 m AGL and a Vaisala HMP45 probe at 9 m AGL, respectively. A sketch of the flux station measurements is provided in Fig. 3.3.

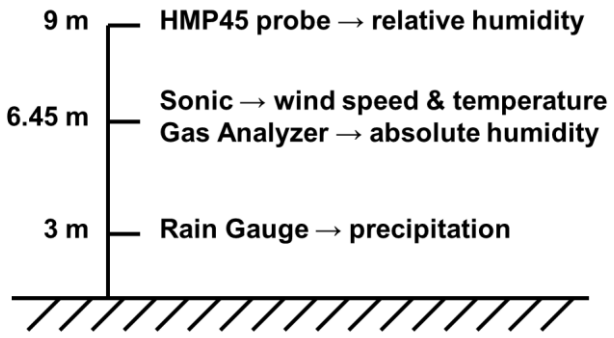

Fig. 3.3. Flux station measurements in Iowa.

These data were used to determine momentum flux, heat flux, and latent heat flux over thirty-minute averaging periods; in turn, the refractive index structure parameter was then calculated and compared to the lowest-available CNR measurement at 40 m AGL. Following Andreas (1988), C_n^2 is given by

$$C_n^2 = z^{-2/3}(At_* + Bq_*)^2 g(\zeta) \tag{3.4}$$

where z is altitude, A and B are wavelength-dependent coefficients, and $\zeta = z/L$ is the stability parameter. Here, the length scale is the Obukhov length

$$L = \frac{u_*^2 \bar{T}}{\gamma \kappa}\left(t_* + \frac{0.61\bar{T}}{\rho + 0.61\bar{Q}} q_*\right)^{-1} \tag{3.5}$$

where γ is the acceleration of gravity, $\varkappa = 0.4$ is von Kármán's constant, $\bar{T}$ and $\bar{Q}$ are representative values of temperature and absolute humidity in the surface layer, and ρ is the density of moist air. The temperature and humidity scales are defined as

$$t_* = -\frac{\overline{w't'}}{u_*} \tag{3.6}$$

$$q_* = -\frac{\overline{w'q'}}{u_*} \tag{3.7}$$

respectively, where u_* is the friction velocity, w is vertical wind velocity, and primes indicate turbulent fluctuations from the mean, while the similarity function is

$$g(\zeta) = \begin{cases} 4.9(1 - 6.1\zeta)^{-2/3} & \text{for } \zeta \leq 0 \\ 4.9\left(1 + 2.2\zeta^{-2/3}\right) & \text{for } \zeta > 0 \end{cases} \tag{3.8}$$

3.4 Results

As discussed previously, lidar performance is expected to be influenced by aerosol backscatter, atmospheric refractive turbulence, humidity, and precipitation. The effects of these parameters are examined in the following subsections.

3.4.1 Aerosol backscatter

From Section 3.2, CNR is expected to be linearly proportional to the backscatter coefficient at fixed altitude in the absence of turbulence. In Fig. 3.4, CNR and β at 100 m AGL are compared for the week 22 August 2010 to 29 August 2010 in Boulder; note the logarithmic scale on the horizontal axis, as CNR is measured in dB. The correlation coefficient is 0.7, indicating a fairly high degree of linear dependence between the variables. Outliers are likely due to variations in atmospheric conditions, such as turbulence and humidity.

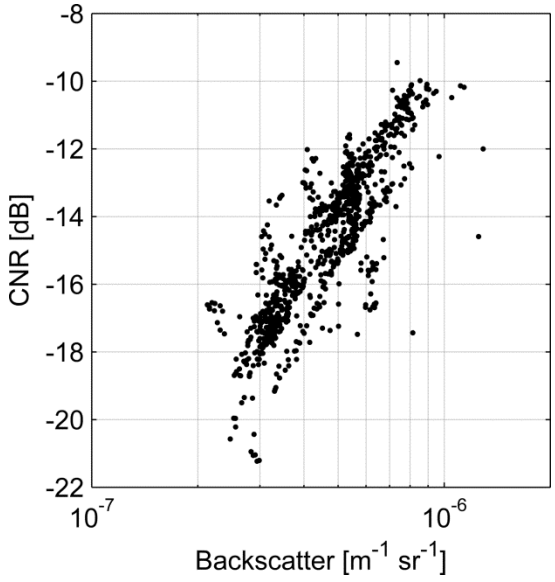

Fig. 3.4. Scatterplot of CNR vs. backscatter at 100 m AGL. Data are for 22–29 August 2010.

Accordingly, the maximum available altitude (MAA) of the Windcube, defined as the highest altitude for which CNR > -22 dB at a given measurement time, should be influenced by the amount of aerosol backscatter. For each Windcube measurement during the month of August 2010, the MAA was determined along with the corresponding backscatter coefficient at that height. The points in Fig. 3.5 represent the average level of backscatter corresponding to each MAA, and the error bars indicate the standard deviation of each set; the rightmost point actually represents all altitudes greater than or equal to 200 m, thus the larger standard deviation for this point than the rest. To verify the trend in Fig. 3.5, one must consider both the average CNR at each MAA and the range-dependent collection efficiency of the Windcube (see Fig. 3.6)—which Lindelöw (2007) modeled using the results of Sonnenschein and Horrigan

(1971)—since from Eq. (3.1) backscatter varies as $\beta \sim (\mathrm{CNR}/\eta)R^2$. Indeed, Fig. 3.7 shows that the left- and right-hand sides of this proportionality are linearly related for the ten distinct MAAs, with a correlation coefficient of 0.932.

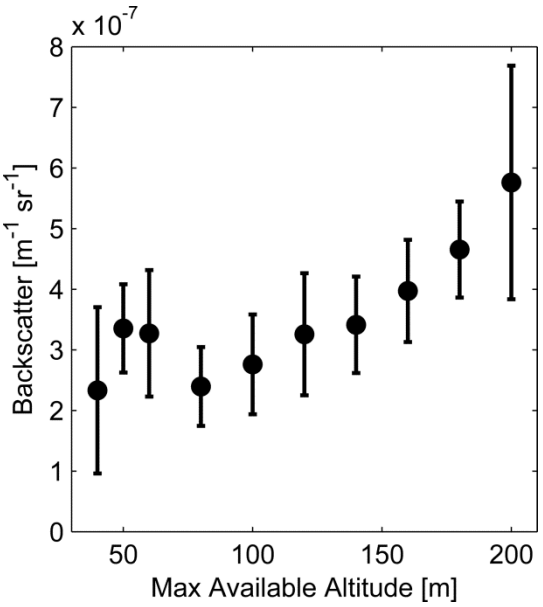

Fig. 3.5. Average level of backscatter corresponding to each MAA for August 2010 in Boulder, Colorado. Error bars indicate the standard deviation of each set.

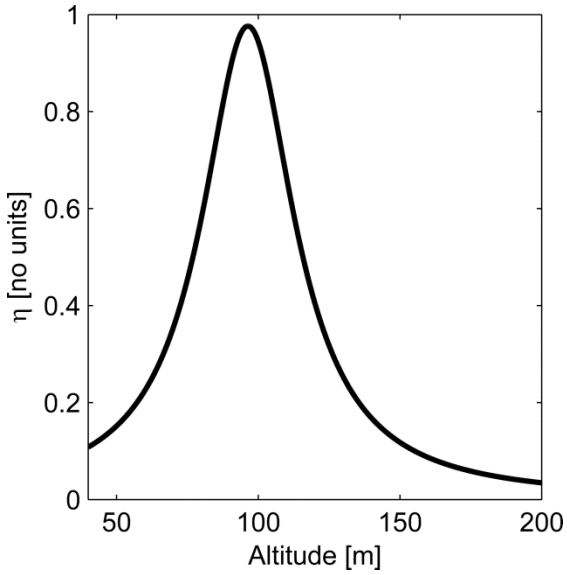

Fig. 3.6. Modeled Windcube collection efficiency vs. altitude.

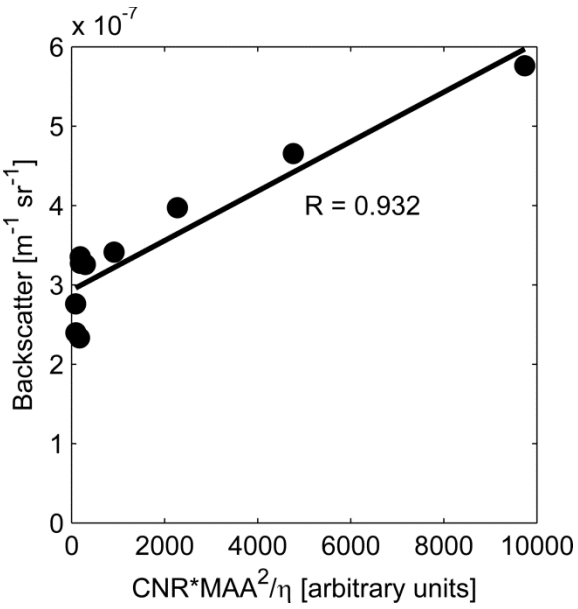

Fig. 3.7. Average ceilometer backscatter vs. average Windcube CNR and modeled collection efficiency for each maximum available altitude. The best-fit line is also shown.

To relate lidar performance to air quality assessments, note that optical backscatter and $PM_{2.5}$, a measurement of the concentration of atmospheric particles less than 2.5 μm in diameter, have been found to be highly correlated in the lowest 200 m of the boundary layer (Charles et al. 2007). A similar relationship is thus expected between CNR and $PM_{2.5}$. Hourly measurements of $PM_{2.5}$ at a resolution of 1 μg m^{-3} were available for the first two weeks of August in Boulder from an air monitoring station located approximately 500 m due north of the Windcube and operated by the Colorado Department of Public Health and Environment. Indeed, as indicated in Fig. 3.8, greater concentrations of particulate matter correspond to higher levels of CNR, in general.

Notably, Fig. 3.9 shows that, on average, a concentration of just 2-3 μg m^{-3} is required for a maximum range of 120 m, a height corresponding to the top of the rotor disk of a typical modern wind turbine. By comparison, the average annual $PM_{2.5}$ concentration for 766 monitoring stations across the United States has hovered between 11 and 13 μg m^{-3} over the last decade, and just 10% of sites measured average annual concentrations of less than 8 μg m^{-3} in that time span (U.S. Environmental Protection Agency 2010). While particulate matter concentrations obviously vary with location and time, these results suggest that the Windcube is generally well-suited for wind energy applications throughout much of the United States.

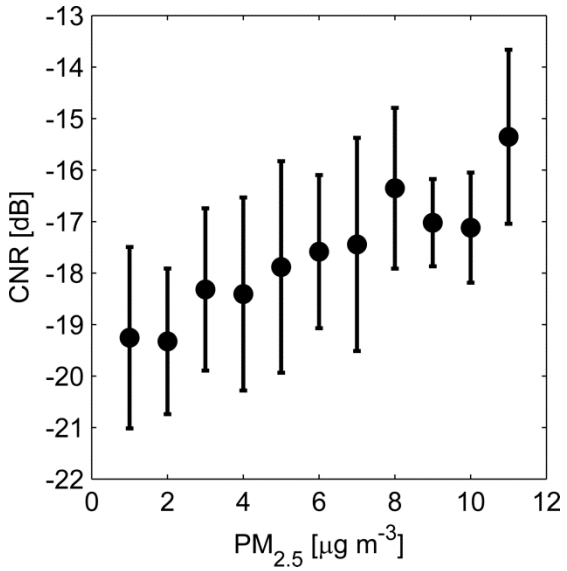

Fig. 3.8. Average CNR at 40 m AGL corresponding to each level of $PM_{2.5}$ for the first two weeks of August 2010 in Boulder, Colorado. Error bars indicate the standard deviation of each set.

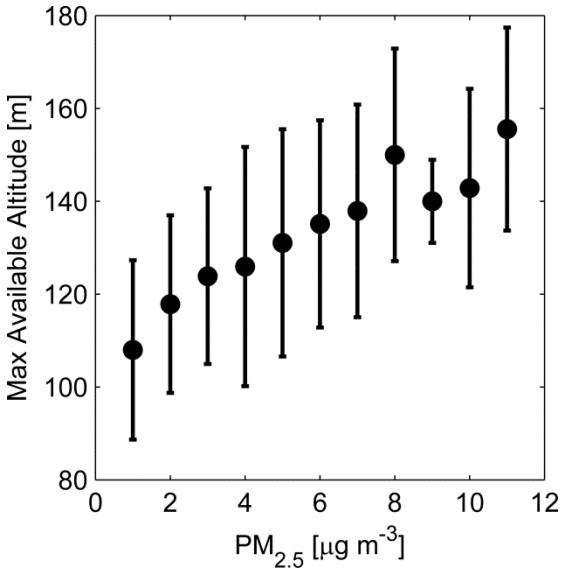

Fig. 3.9. Average MAA corresponding to each level of $PM_{2.5}$ for the first two weeks of August 2010 in Boulder, Colorado. Error bars indicate the standard deviation of each set.

Also noteworthy is that the Boulder dataset exhibits a regular diurnal cycle in CNR, inducing a diurnal pattern in the MAA of the Windcube. The diurnal variation of CNR at 40 m AGL was averaged over the days of August 2010 in Boulder and can be seen in Fig. 3.10. Typically reaching a local minimum in early morning around 06:00 LT, CNR increases as aerosols are lifted with the development of convective conditions after sunrise. Countering this effect is the increase of the boundary layer height, which tends to lower aerosol concentration with the entrainment of cleaner air from above, and thus CNR reaches a peak in mid- to late-morning. The local maximum around 15:00 LT is due to rain, a common occurrence in mid-afternoon for the local climate. The last local maximum near 17:30 LT is likely the result of increased vehicular aerosol

emissions during rush hour. Although the height of the boundary layer diminishes after sunset, anthropogenic aerosol production also decreases and aerosols close to the surface are lost by sedimentation, leading to lower CNR. This diurnal cycle—due to variations in local anthropogenic activity, meteorological conditions, boundary layer height, and removal mechanisms—is typical of urban areas (Gomes 2008). A similar pattern is apparent for the average diurnal variation of MAA in Fig. 3.11, which indicates how high the Windcube can be expected to operate throughout the course of the day. On average, the MAA in summertime Boulder ranges from about 140 m AGL in early morning to about 180 m AGL just before noon, well above the reach of modern turbine blades.

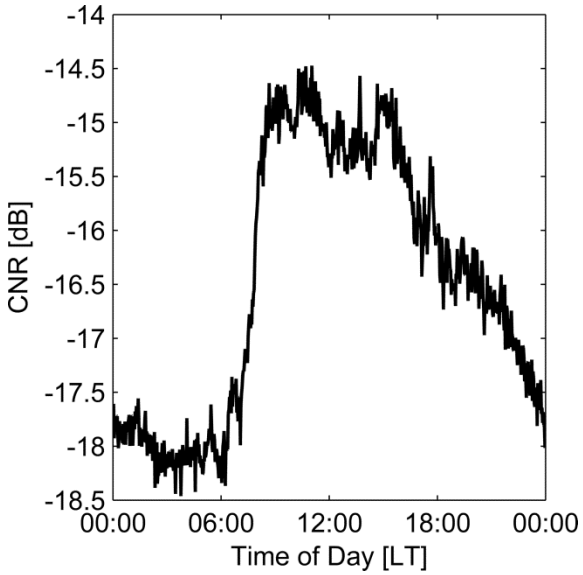

Fig. 3.10. Average CNR diurnal cycle at 40 m AGL for August 2010 in Boulder, Colorado.

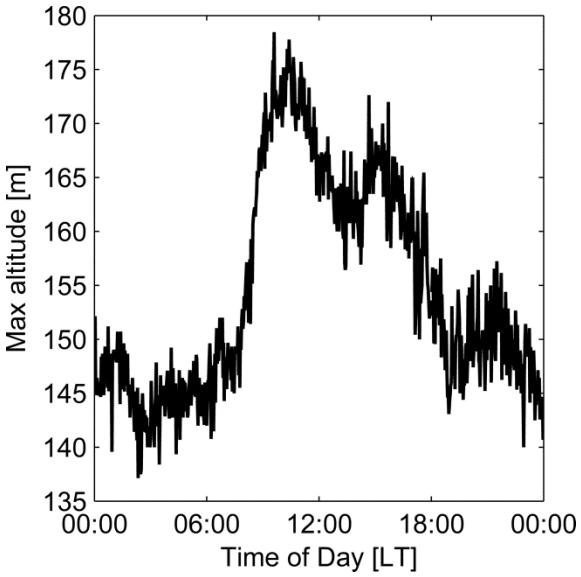

Fig. 3.11. Average diurnal cycle of MAA for August 2010 in Boulder, Colorado.

3.4.2 Atmospheric refractive turbulence

While aerosol backscatter exerts the primary influence on CNR, strong levels of atmospheric refractive turbulence can cause signal degradation. Unfortunately, independent flux measurements for quantifying the effect of atmospheric refractive turbulence on lidar performance were only available during the field campaign in Iowa. From Fig. 3.1, CNR should only noticeably decrease in strongly turbulent conditions, say $C_n^2 > 5\times10^{-14}$ m$^{-2/3}$, a situation that occurred less than one percent of the time in Iowa. Because refractive turbulence levels were most often weak or moderate, there is no discernible relationship between the two variables, as indicated in Fig. 3.12. Despite the fact that the lowest-available CNR measurement at 40 m AGL is compared to C_n^2 at 9

m, refractive turbulence is expected to be even weaker at 40 m based on several boundary layer models (Lawson and Carrano 2006).

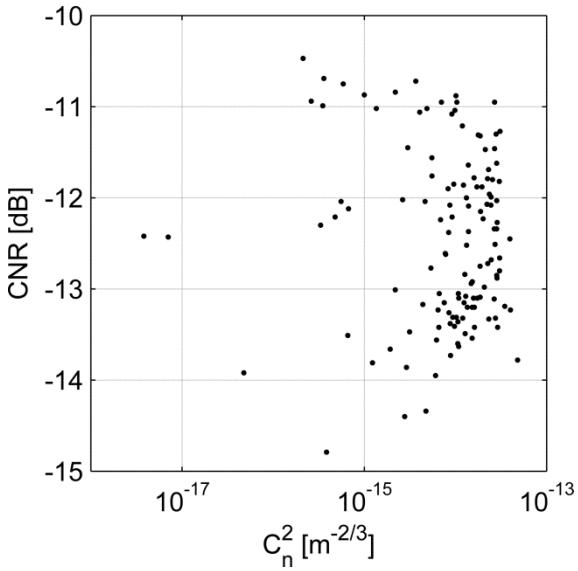

Fig. 3.12. Scatter plot of CNR at 40 m AGL vs. C_n^2 at 9 m from 1 to 4 July 2010 at a wind farm near Ames, Iowa.

3.4.3 Humidity and precipitation

Fig. 3.13 shows the effect of RH on CNR during the Iowa field deployment. The bold black line is a nonlinear regression of the form CNR = $a(1 - \mathrm{RH})^b$, following the regression for backscatter vs. RH used in Im et al. (2001). Here, a = -16 and b = 0.07. There is almost no correlation for RH $<$ 0.8, but CNR does increase above this level of humidity, thus confirming the results in Wulfmeyer and Feingold (2000); the increase is especially sharp near saturation. During August 2010 in Boulder, which has a high

desert climate, RH was never greater than 0.9 even during precipitation events: CNR and RH were almost completely uncorrelated for this time period.

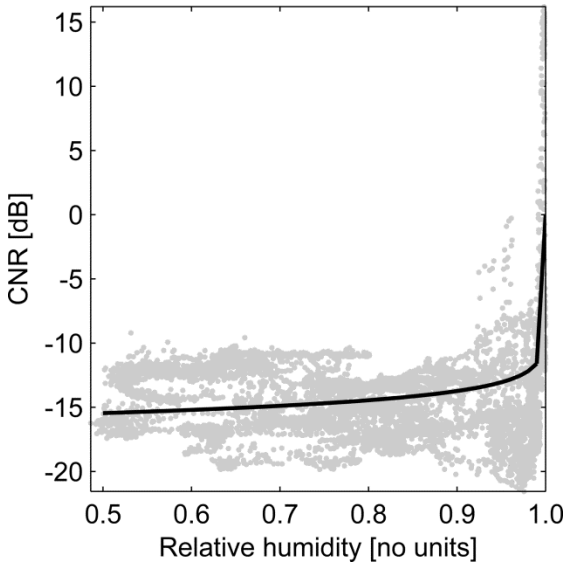

Fig. 3.13. Scatter plot of CNR at 40 m AGL vs. RH at 9 m AGL. Data are from 28 June to 9 July 2010, excluding periods of measurable precipitation, at a wind farm near Ames, Iowa. The bold black line indicates the best-fit curve.

One possible advantage of lidar over sodar technologies is that sodar is known to collect erroneous measurements during precipitation events. Although the manufacturer suggests that the Windcube is capable of taking measurements during periods of rain, Fig. 3.14 indicates that measurements of vertical velocity are likely invalid; horizontal velocity measurements may be uncontaminated (Albers and Janssen 2008). During precipitation events, w ranges between 1 to 5 m s^{-1}, which is of the same order as the terminal velocity of a raindrop (Foote and du Toit 1969) and almost certainly too large to be actual vertical wind speed, as no microbursts or similar type of meteorological

phenomena were reported to be in the area at the time according to forecast discussions released by the National Weather Service. Similarly, previous studies, such as Gottschall and Courtney (2010), have found it necessary to filter out Windcube data in the presence of rain. Thus, rain may interfere with operation of the Windcube, and measurements of vertical velocity during precipitation events must be evaluated with caution.

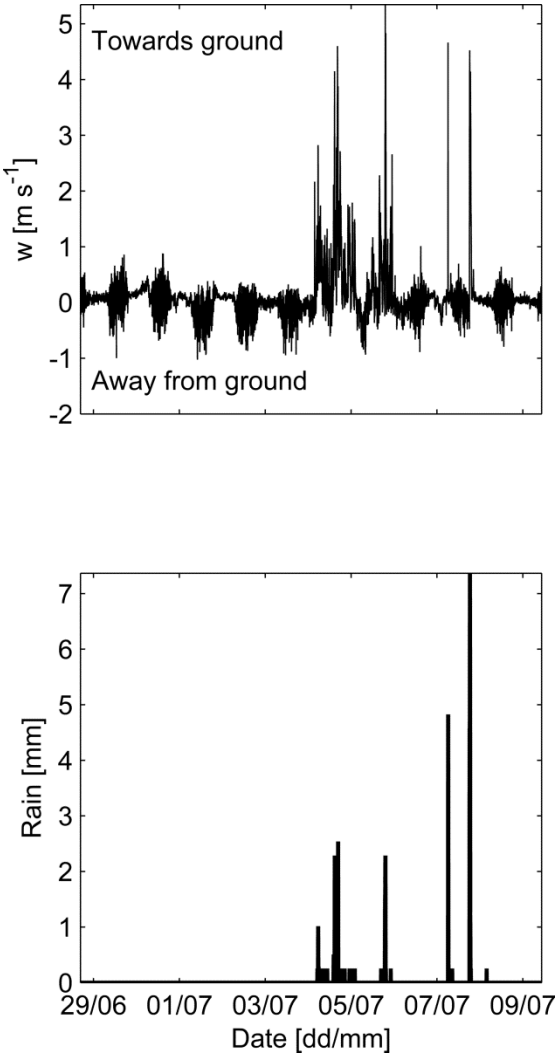

Fig. 3.14. Comparison of (top) Windcube-measured vertical wind speed at 40 m AGL and (bottom) precipitation during the Iowa field deployment. Positive vertical winds are toward the ground. Each tick mark on the horizontal axis corresponds to midnight of the respective date.

3.4.4 Summary of data availability

A comparison of data availability at different heights for the Boulder and Iowa field deployments can be seen in Fig. 3.15; note that the data availability in Iowa is higher at all altitudes. Additionally, the fractional occurrence of a particular MAA was calculated by dividing the number of measurements for which that height was the maximum available by the total number of Windcube measurements in the given dataset. Fig. 3.16 compares the occurrence of each MAA in Boulder and Iowa. The Windcube could "see" at or above 200 m only about 20% of the time in Boulder, whereas measurements were available at or above this height over half the time in Iowa.

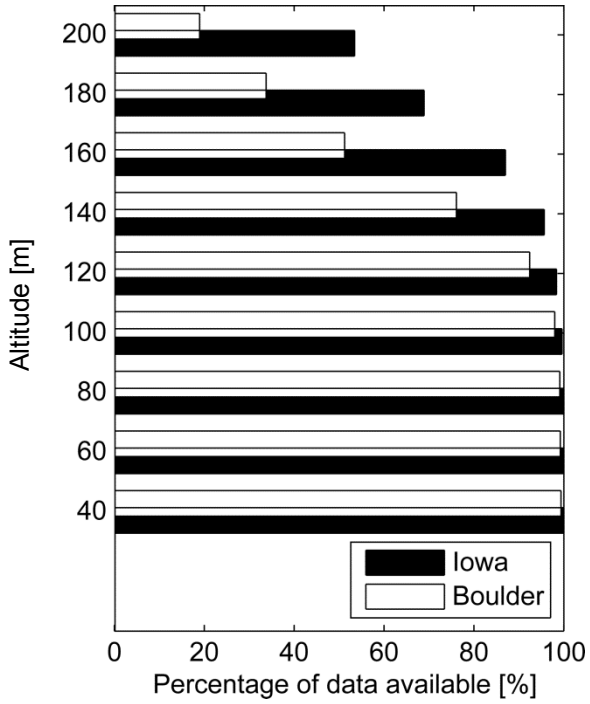

Fig. 3.15. Histogram comparing data availability at different altitudes for the Boulder and Iowa field deployments.

The mean $PM_{2.5}$ concentrations during the month of August 2010 in Boulder and during the Iowa field deployment were 5.7 μg m^{-3} and 8.2 μg m^{-3}, respectively, suggesting that the improved Windcube performance in Iowa can probably be explained by higher concentrations of particulate matter. While humidity was also higher in Iowa than in Boulder, $PM_{2.5}$ is expected to be the dominant influence on optical backscatter, and hence on CNR. The greater amount of data availability in Iowa cannot necessarily be attributed to the effects of humidity with such a limited dataset, especially since $PM_{2.5}$ and humidity tend to be negatively correlated (Sharma et al. 2005).

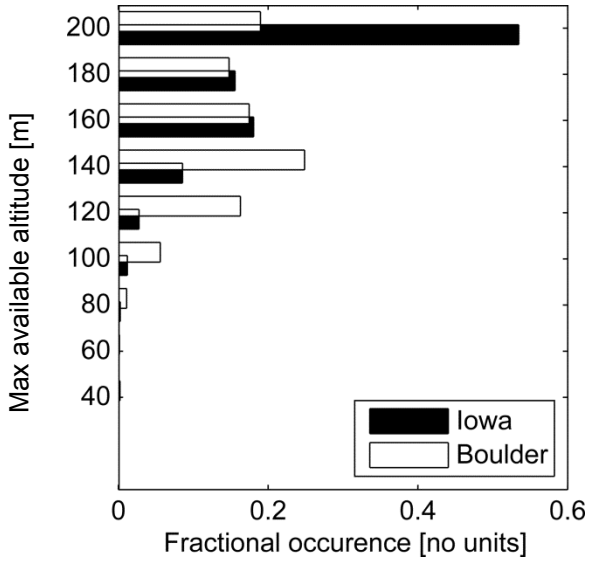

Fig. 3.16. Histogram comparing maximum available Windcube altitude for the Boulder and Iowa field deployments.

3.5 Conclusion

To determine situations of acceptable data availability, the theoretical parameter dependence of lidar CNR has been investigated in the field using a Windcube. The four most significant factors found to influence lidar performance are: aerosol backscatter, atmospheric refractive turbulence, humidity, and precipitation. In summary, Windcube CNR tends to be higher during the day than at night and is linearly proportional to aerosol backscatter, which is highly correlated to $PM_{2.5}$ in the lowest part of the boundary layer. Because CNR is proportional to the inverse of the square of propagation distance, more backscatter is needed at higher altitudes for suitable data return. Accordingly, it should be possible to monitor Windcube performance during

future field deployments by using a ceilometer to measure vertical aerosol concentrations and the height of the boundary layer. Although the loss due to atmospheric refractive turbulence can be quite severe in theory, such strongly turbulent conditions did not occur in the present datasets even though data were taken in mid-summer daytime, and therefore this effect could not be discerned. While practically uninfluenced by low levels of humidity, CNR increases sharply near the saturation point. Windcube performance is adversely affected by precipitation, as rainfall is measured instead of vertical wind speed.

Overall, the results show that lidar can be expected to reliably provide profiles of wind speed, direction, and turbulence intensity at altitudes within a typical wind turbine rotor disk. The average hub height and rotor diameter of wind turbines installed in 2009 in the United States was 78.8 m and 81.6 m, respectively (Wiser and Bolinger 2010), meaning that measurements between about 40 to 120 m above the surface will be required for accurate resource assessment and evaluation of turbine performance at modern wind farms. In particular, for the Windcube considered in this study, data was available up to 120 m AGL more than 90% of the time both in Boulder and at a wind farm in the Great Plains. Given that the mean $PM_{2.5}$ concentrations during both experiments were below the national annual average, this type of lidar seems a

promising candidate for widespread use in the wind energy industry, especially at humid sites characterized by relatively high concentrations of particulate matter.

Author contributions

The bulk of this chapter is reproduced from Aitken et al. (2012). M.L.A. wrote the manuscript and performed the data analysis. J.K.L. designed the experiment and provided general supervision of the research. Both M.E.R. and J.K.L. revised the manuscript. All authors helped to acquire the field data and to interpret the results.

Chapter 4

Wind Turbine Wake Characterization with Scanning Remote Sensors

All models are wrong, but some are useful.

–George E. P. Box

4.1 Introduction

Wind turbines convert energy from the freestream, resulting in a volume of disturbed flow behind the rotor characterized by reduced wind speed and increased turbulence. The velocity deficit (VD) in this wake region diminishes with distance, as faster-moving air outside is gradually entrained. Even so, a turbine in the lee of and proximate to another produces less power and experiences higher fatigue loads than it would otherwise. As utility-scale turbines rarely exist in isolation, detailed knowledge of the mean flow and turbulence structure inside wakes is necessary for correctly modeling both power production and turbine loading at modern wind farms; see, for example, Porté-Agel et al. (2011), Churchfield et al. (2012), and Fitch et al. (2012).

To this end, the Turbine Wake and Inflow Characterization Study (TWICS) was conducted in the spring of 2011 to quantify various wake features downstream of a

multi-MW turbine located at the National Wind Technology Center (NWTC), a research and development facility operated by the U.S. Department of Energy's National Renewable Energy Laboratory (NREL) just south of Boulder, Colorado. Full-scale measurements of wake dynamics are hardly practical or even possible with conventional sensors, such as cup anemometers mounted on meteorological (met) masts. Accordingly, the High Resolution Doppler Lidar (HRDL) developed by the Earth System Research Laboratory (ESRL) of the National Oceanic and Atmospheric Administration (NOAA) was employed to investigate wake characteristics under various atmospheric conditions. HRDL remotely senses line-of-sight (LOS) wind velocities u_{LOS} and has been used in several previous studies of boundary layer dynamics (Grund et al. 2001; Banta et al. 2002; Newsom and Banta 2003; Tucker et al. 2009; Pichugina et al. 2012). Note that complementary TWICS analysis is provided in Smalikho et al. (2013), in particular a study of the relationship between turbulent energy dissipation rate and wake length.

Due in large part to the limited availability of field test data for model verification, wind farm wake modeling—and hence the optimization of wind turbine layouts—has suffered from an unacceptable degree of uncertainty to date, particularly in complex terrain (Barthelmie et al. 2010). The advent of innovative measurement techniques involving scanning remote sensors (Käsler et al. 2010; Bingöl et al. 2010;

Trujillo et al. 2011; Clive et al. 2011; Hirth et al. 2012; Hirth and Schroeder 2013; Iungo et al. 2013) suggests the need for new approaches to identify and characterize wind turbine wakes. Here, a set of quantitative procedures is developed for determining various wake features—such as the velocity deficit, the size of the wake boundary, and the location of the wake centerline—that are designed to be broadly applicable to other remote sensor datasets and also to output from computational fluid dynamics (CFD) simulations of wind turbines. In what follows, Section 4.2 provides a brief overview of the theory and empirical observation of wind turbine wake aerodynamics. In Section 4.3, the experimental setup and post-processing wake detection algorithms are described. Main results are presented in Section 4.4, in which wake characteristics are categorized by ambient wind speed, atmospheric stability, and ambient turbulence. A summary and recommendations for future studies are offered in Section 4.5.

4.2 Background and previous work

4.2.1 Wind turbine wake dynamics

Studies of wind turbine wakes often distinguish between the near and far wake regions, with the dividing line loosely taken to be a few rotor diameters (D) downstream (Vermeer et al. 2003). In the near wake, the velocity deficit profile in the transverse and vertical directions depends on the amount of lift produced along the span of the blade. Very little lift is generated at the blade root because of a suboptimal airfoil cross-section

and the connection to the hub, and also at the end of the blade because of tip vortices. Maximum lift, on the other hand, is generated near 75% blade span, and consequently the velocity deficit profile contains two local minima that correspond roughly to these points along the blades. Farther downwind, in the far wake, turbulent mixing results in the merging of the two troughs to form a single trough, which is approximately Gaussian in shape (Magnusson 1999).

4.2.2 Velocity deficit

Results from previous field experiments vary because of differences in inflow conditions, atmospheric stability, and surface roughness, but in general, velocity deficits are greatest in the near wake and gradually diminish downstream from the turbine in the far wake. Wakes tend to dissipate more rapidly when the ambient flow is turbulent because of more efficient mixing between the wake and the surrounding air (Baker and Walker 1984; Magnusson and Smedman 1994). Additionally, velocity deficits are greatest when the wind speed is below rated because of variation in the turbine thrust coefficient (Elliott and Barnard 1990; Magnusson and Smedman 1994; Helmis et al. 1995; Barthelmie et al. 2007). Previous measurements of the velocity deficit versus longitudinal distance downstream of the turbine, henceforth denoted by x, are summarized in Fig. 4.1. The fit to the data is made assuming that VD follows a power law (Högström et al. 1988; Frandsen et al. 2006),

$$\mathrm{VD}(x) = \mathrm{VD}_0 \left(\frac{x}{D}\right)^n, \tag{4.1}$$

with $\mathrm{VD}_0 = (56 \pm 4)\%$ being the velocity deficit at $x = 1\mathrm{D}$ and $n = -0.57 \pm 0.05$ an exponent controlling the attenuation of the velocity deficit with downstream distance. Interestingly, the aggregate best-fit value $n = -0.57$ nearly matches the value of the scaling exponent predicted by classical fluid mechanics similarity theory at infinite Reynolds number, which says the deficit should scale as $(x/\mathrm{D})^{-2/3}$ (Johansson et al. 2003).

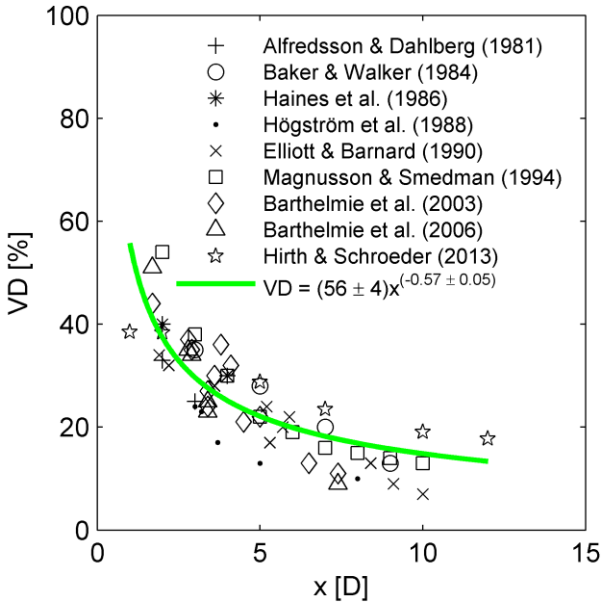

Fig. 4.1. Velocity deficit as a function of downstream distance, as measured by previous field experiments.

Crespo et al. (1988) observed both numerically and experimentally that the point of maximum velocity deficit is located below the turbine axis, because of tower shadow, shear of the incoming flow, and the presence of the ground. Other investigators have

asserted that maximum velocity deficits occur below hub height (Elliott and Barnard 1990), at hub height (Kambezidis et al. 1990), and above hub height (Magnusson and Smedman 1994; Helmis et al. 1995); the velocity deficit profile has a maximum "near" hub height in Barthelmie et al. (2003). This discrepancy probably arises from differences in rotor tilt, stability conditions, and terrain among the experiments. It will be shown in this chapter and in Chapter 6 that the rotor tilt of modern utility-scale turbines causes the vertical location of the wake centerline to shift upward with downstream distance, similar to the way the wake is deflected horizontally in the case of yaw error.

4.2.3 Wake size and expansion rate

In addition to velocity deficit, optimal siting of individual turbines within wind farms hinges on accurately characterizing wake size and expansion rate. From now on, width (w) and height (h) indicate the size of the wake in the lateral and vertical directions, respectively. In the near wake, the wake enlarges because of mass continuity, as the velocity deficit reaches a maximum at some nonzero distance behind the turbine. Farther downstream, turbulent mixing induces entrainment of the faster ambient flow, and the resulting momentum transfer causes the velocity deficit to decrease and the wake to expand. Here, the wake growth rate depends upon not just mechanical turbulence generated by the rotor, but also upon atmospheric buoyant and shear-

generated turbulence. Moreover, due to the presence of the ground, the growth rate of the wake in the vertical direction is less than that in the lateral direction.

The term "wake width" is subjective, and various definitions exist within the literature. Here, the wake width is taken to be the 95% confidence interval of the Gaussian velocity deficit profile, which is analogous to the definition in Hansen et al. (2012) using power deficits. Wake width observations from previous field experiments can be seen in Fig. 4.2. Elliott and Barnard (1990) base their estimation of wake width on the wind speed profile in some cases, and on the turbulence intensity profile in others. The wake widths for Magnusson and Smedman (1994) and Trujillo et al. (2011) are inferred from figures in those papers using the 95% confidence interval criterion. The fit to the data is made assuming that w follows a power law (Högström et al. 1988; Frandsen et al. 2006),

$$w(x) = w_0 \left(\frac{x}{D}\right)^m , \tag{4.2}$$

with $w_0 = (1.3 \pm 0.1)\mathrm{D}$ being the wake width at $x = 1\mathrm{D}$ and $m = 0.33 \pm 0.05$ an exponent controlling the expansion of the wake with downstream distance. Again, it is interesting to note that the aggregate best-fit value $m = 0.33$ closely matches the value of the scaling exponent predicted by similarity theory at infinite Reynolds number, which says the boundary should scale as $(x/\mathrm{D})^{1/3}$ (Johansson et al. 2003).

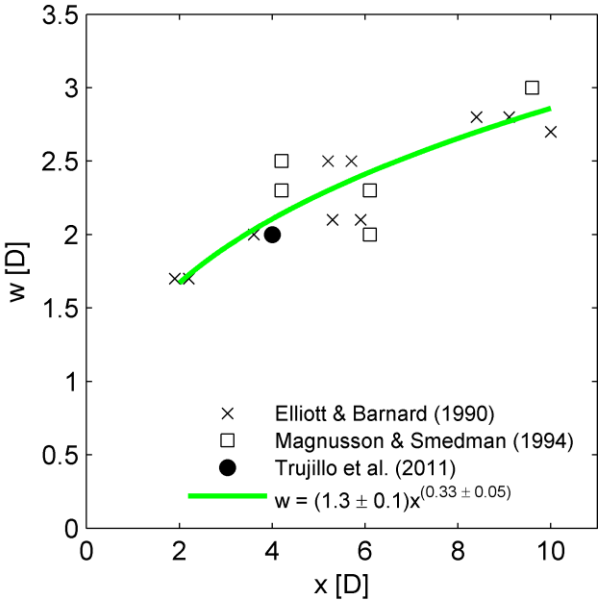

Fig. 4.2. Wake width as a function of downstream distance, as measured by previous field experiments.

4.3 Data and methods

Covered mostly with short grasses, the NWTC is located near the base of the foothills of the Rocky Mountains, to the east-southeast of Eldorado Canyon. During the winter and spring, the canyon funnels strong winds directly to the site, with a predominant wind direction of about 290° (Banta et al. 1995; Banta et al. 1996; Clifton and Lundquist 2012). The strong directionality of the flow justified the use of HRDL, which measures LOS velocities and remained at a fixed location during the experiment. Positioned 880 m at a bearing of approximately 310° from the turbine of interest, HRDL could best resolve winds blowing from this direction. In addition to HRDL, a Leosphere/NRG Windcube v1 vertically-profiling lidar (see Chapter 3) provided

supplementary measurements of the turbine inflow conditions, and observations from an 80-m met tower were used to calculate the bulk Richardson number Ri_B, a metric of atmospheric stability. The layout of the instrumentation is depicted in Fig. 4.3, and specifications for HRDL and the wind turbine are given in Tables 4.1 and 4.2, respectively. Note that the turbine rotor diameter $D = 101$ m and the hub height $H = 80$ m. Nearly 100 hours of wake measurements were collected over a period spanning from 5 April 2011 to 3 May 2011.

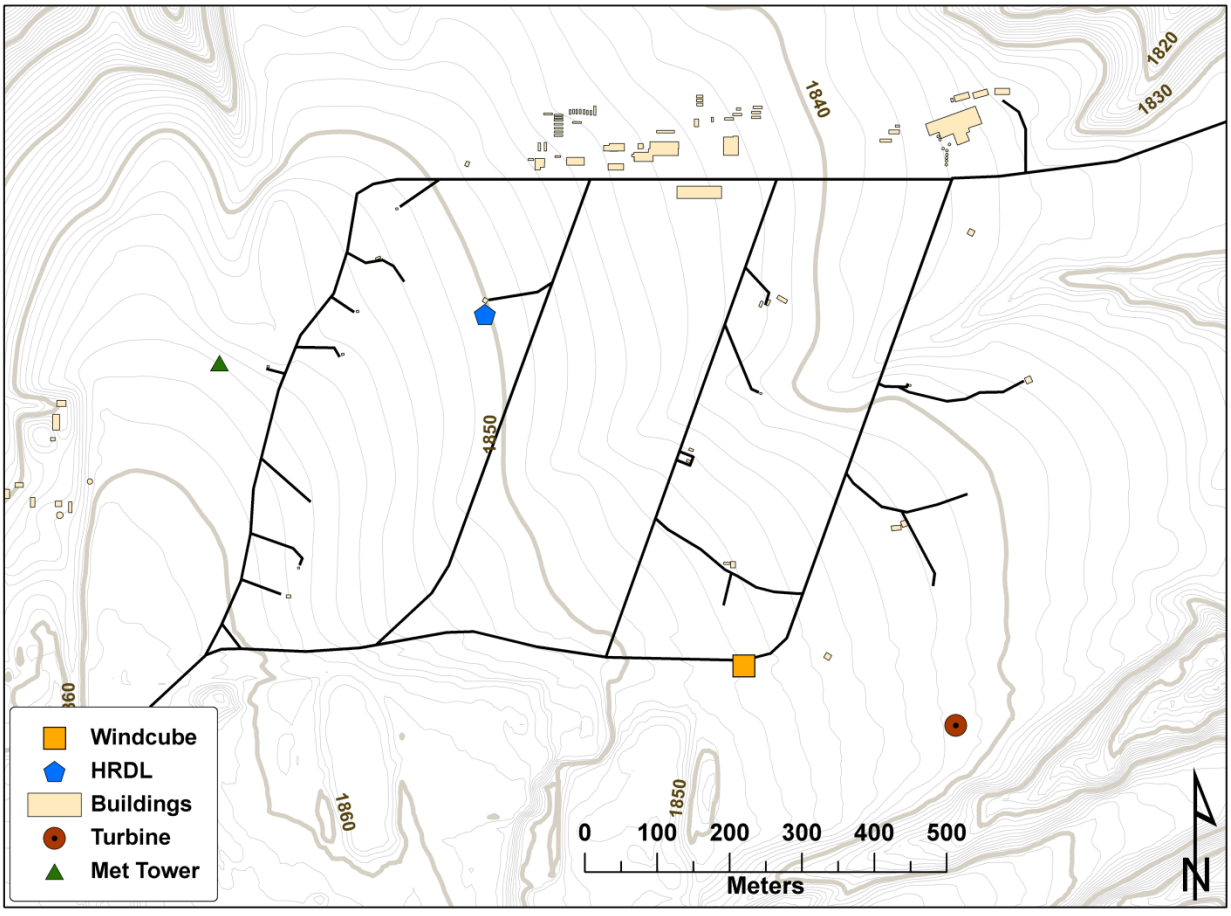

Fig. 4.3. Map of the NWTC, with the instrumentation and turbine indicated by the symbols described in the legend. Courtesy of Joe Smith and Steve Haymes at NREL.

Table 4.1. High Resolution Doppler Lidar technical specifications.

Wavelength	2.0218 μm
Pulse energy	1.5 mJ
Pulse rate	200 Hz
Pulse width	200 ns
Scan	Upper hemisphere
Range resolution	30 m
Time resolution	0.02 s
Velocity precision	5 cm s^{-1}
Minimum range	0.2 km
Maximum range	2- 9 km (typically 3 km)
Laser	Tm:Lu, YAG diode-pumped, injection-seeded laser

Table 4.2. Wind turbine technical specifications.

Diameter (D)	101 m
Hub height (H)	80 m
Rated power	2.3 MW
Cut-in wind speed	3–4 m s^{-1}
Rated power at	12–13 m s^{-1}
Cut-out wind speed	25 m s^{-1}
Rotor tilt	6 deg

Wind resource characteristics for the site, as measured at 80 m by the Windcube over the course of the field campaign, are shown in Fig. 4.4. The Weibull fit to the wind speed distribution (Justus et al. 1978) in Fig. 4.4a has scale parameter $\lambda = 7.20$ and

shape parameter $k = 1.46$. The histogram and wind rose in Figs. 4.4b and 4.4c indicate that most of the strong winds came from the west-northwest, corresponding nearly to the line-of-sight from HRDL to the turbine; the fit to the wind direction data in Fig. 4.4b is a finite von Mises mixture distribution (Masseran et al. 2013) with three modes at 7°, 175°, and 287°. In Fig. 4.4d, the turbulence intensity I is defined as the ratio of the horizontal wind speed standard deviation to the mean horizontal wind speed, taken over a 10-min interval. Turbulence intensity was calculated only for wind speeds greater than 4 m s^{-1}. The log-normal fit to the turbulence intensity distribution (Larsen 2001) has location parameter $\mu = -1.73$ and scale parameter $\sigma = 0.49$. The mean wind speed and turbulence intensity during the course of the experiment were 6.5 m s^{-1} and 0.20, respectively. By comparison, Elliott et al. (2009) measured 80-m turbulence intensities between 0.09–0.13 at seven sites in the midwestern United States, where much of the nation's wind power capacity is located.

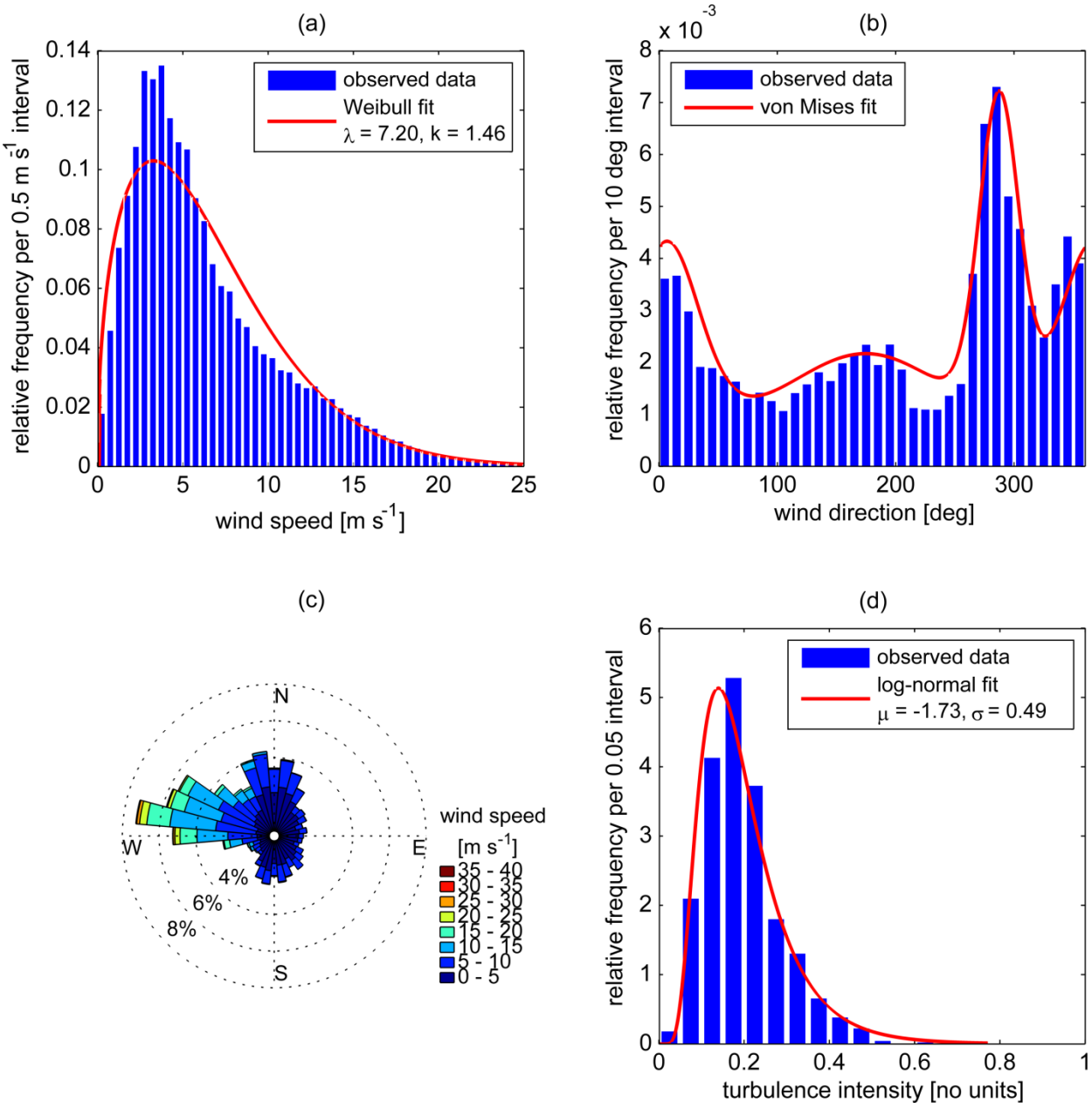

Fig 4.4. Site wind resource characteristics for the NWTC during the period 5 April 2011 to 3 May 2011, as measured at 80 m by the Windcube: (a) wind speed, (b) wind direction, (c) wind rose, and (d) turbulence intensity.

4.3.1 High-resolution Doppler lidar

The signature instrument in TWICS was HRDL, a pulsed coherent Doppler lidar with 30-m range resolution and 5 cm s^{-1} velocity precision, depending on atmospheric and operating conditions. Following the terminology used in radar display, sweeping the azimuth angle of the beam while holding the elevation angle fixed is known as a plan position indicator (PPI) scan. In contrast, a range-height indicator (RHI) scan involves sweeping the elevation angle while holding the azimuth angle fixed. At low elevation angles, PPI scans yield close approximations of horizontal wind speed near the surface, while RHI scans provide vertical cross sections of the radial wind field. By employing a well-collimated beam, HRDL does not suffer from antenna side lobe contamination, allowing wind profile measurements to be taken very close to the surface and to other obstacles (Grund et al. 2001).

These scanning techniques were used to examine the structure of the wake behind the turbine. Sample pseudocolor plots of HRDL-measured LOS velocity for both PPI and RHI scans, in which wakes appear as regions of cooler colors, are shown in Figs. 4.5 and 4.6, respectively. During the study, a PPI scan typically involved holding the elevation angle constant at a value between 3–4°, while sweeping the azimuth through an angle of about 30°, centered on the turbine, at a rate of roughly 1.5° s^{-1}. Normally lasting approximately 20 s, a full sector sweep usually included measurements

at about 30 discrete azimuth angles. By contrast, a typical RHI scan involved holding the azimuth angle constant at a value within ±3° from the line connecting HRDL to the turbine, while sweeping the elevation angle at a rate slightly less than 1° s^{-1} from 0° to between 10–15°. Because of the geometry of ground-based remote sensing, the altitude at which PPI scans sample the flow increases with range, such that measurements are eventually taken above the wake at some distance far behind the turbine, depending on the elevation angle. Moreover, RHI scans may not always intersect the wake, especially at longer range gates, because of wake meandering and variations in wind direction and turbine yaw. The scans were, however, designed to capture as much of the wake as possible, given these geometric constraints.

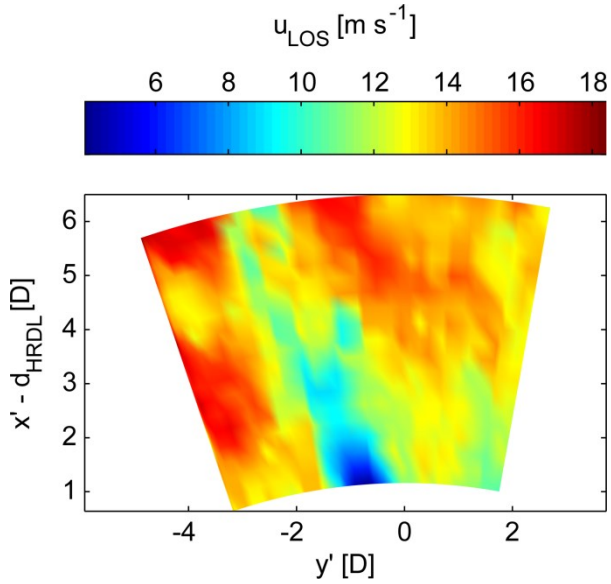

Fig. 4.5. Sample pseudocolor plot of HRDL-measured LOS velocity for a single PPI sweep. The wake is visible as the streak of blue behind the turbine, which is located outside the figure at the point (0,0). The scan here was taken from 18:20:18 to 18:20:37 LT on 14 April 2011 with a beam elevation angle of 3.5 deg.

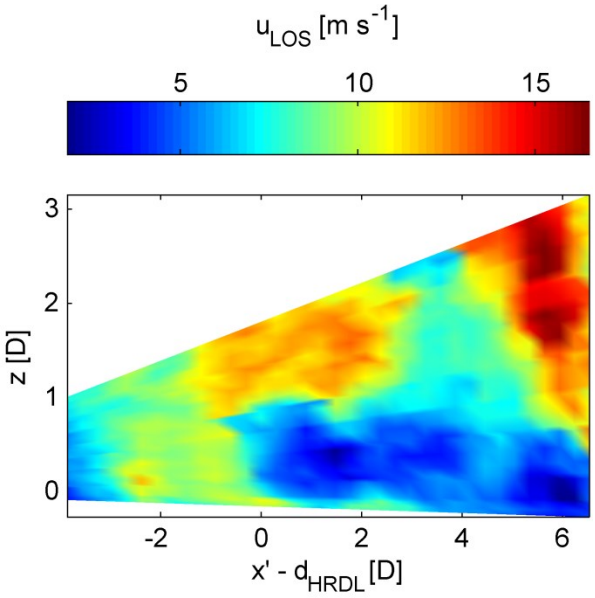

Fig. 4.6. Sample pseudocolor plot of HRDL-measured LOS velocity for a single RHI sweep. The wake is visible as the streak of blue behind the turbine, which is located at $x' - d_{\mathrm{HRDL}} = 0$. The scan here was taken from 16:49:38 to 16:49:52 LT on 14 April 2011 with a beam azimuth angle of 0.3 deg to the left of the x'-axis.

In addition to measuring properties of the wake, HRDL was well-positioned to quantify the variability of the inflow to the turbine. The spatial turbulence intensity I_{space} is defined as the ratio of the wind speed standard deviation to the mean wind speed, calculated over a given region of space, which is taken here to be the annular sector of each scan with radii spanning from 4D to 2D upwind of the turbine. These distances are chosen to correspond to the standard range for measuring freestream winds in the determination of wind turbine power performance (International Electrotechnical Commission 2005). Fig. 4.7a shows an example of the LOS velocity

measurements within this region, using the same PPI scan as the one depicted in Fig. 4.5. To estimate I_{space} in the case of the PPI scans, horizontal homogeneity of the wind field over the sensed area is assumed, with uniform wind speed u and direction φ, as is typical for wind lidar; see, for example, Chapter 2 and Frehlich et al. (2006). When the LOS velocity signal is displayed as a function of azimuth angle ϑ, a plot like the one shown in Fig. 4.7b is obtained, since $u_{\mathrm{LOS}} = u\cos(\vartheta - \varphi)$. A weighted nonlinear regression scheme (Box et al. 2005) is used to fit this equation to the data, in which each weight is equal to the reciprocal of the variance of the measurement. Velocity precision is estimated using the Cramér-Rao lower bound (Rye and Hardesty 1993), because HRDL operates close to this theoretical limit in both high and low signal-to-noise ratio (SNR) conditions (Grund et al. 2001). The spatial turbulence intensity is then calculated by dividing the root mean square deviation (RMSD) of the fit by the modeled wind speed u. In this particular example, RMSD = 5.24 m s^{-1} and u = 15.4 m s^{-1}, such that I_{space} = 34%. To be clear, the fit here is intended to establish an average wind speed within the inflow region, so that the variation about that average may be quantified, analogous to the way turbulence intensity is normally calculated over a temporal interval. In addition to indicating the turbulence within the flow, the amplitude of the spatial wind fluctuations is an important factor in determining the

minimum velocity deficit that can be captured by the wake detection algorithms described in Section 4.3.4.

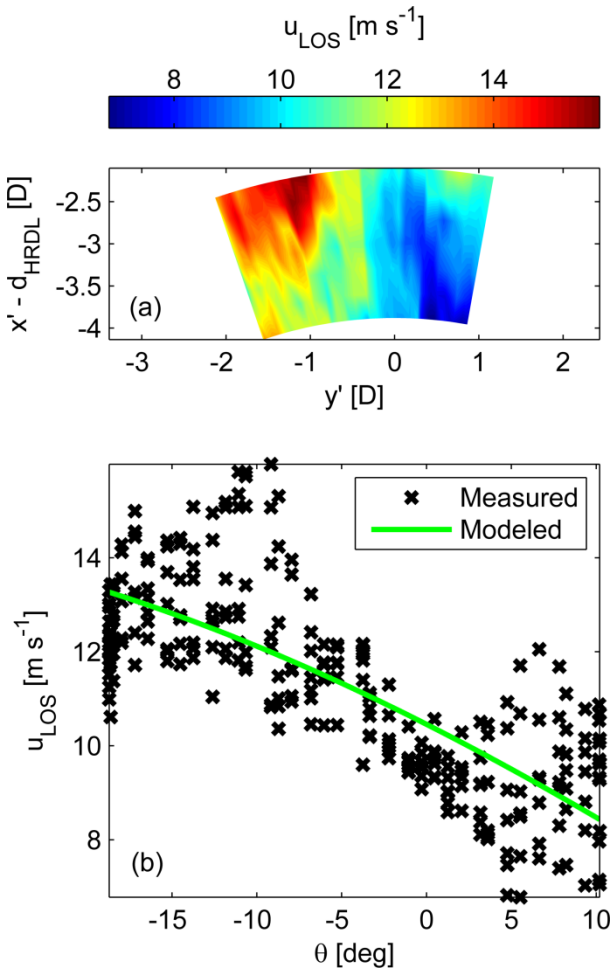

Fig. 4.7. (a) The inflow to the turbine in the same PPI scan as that depicted in Fig. 4.5 and (b) the best-fit model of the measured LOS velocity, assuming uniform wind speed and direction.

A similar procedure was used to determine the spatial turbulence from the inflow measurements of the RHI scans (see, for example, Fig. 4.8a), whereas in this case the wind speed is assumed to increase logarithmically with height:

$$u_{\mathrm{LOS}}(z,\delta) = \frac{u_*}{k}\ln\left[\frac{z-d}{z_0}\right]\cos\delta\,, \tag{4.3}$$

where δ is the beam elevation angle, u_* is the friction velocity, $k = 0.4$ is the von Kármán constant, z_0 is the roughness length (Stull 1988), and d is an offset factor to account for the complex terrain. The vertical coordinate z is measured with respect to the ground elevation at HRDL, where $z = 0$. From the wind speed profiles measured by the met tower, z_0 was empirically determined to be 0.01 m for west-northwesterly winds at the site. After a series of trial and error, the inclusion of stability corrections to the logarithmic profile was rejected because they were found to be particularly ill-suited for describing the flow at the NWTC. The incorporation of the parameter d essentially allows the model to control the height at which the wind speed goes to zero, since the flow often did not neatly conform to the terrain. As shown in the elevation profile of Fig. 4.9, the slope along the line-of-sight from HRDL to the turbine is quite modest, but afterward there exists a sequence of steep gullies. To be clear, the parameter d is traditionally included to account for obstacles, such as trees or buildings, to the flow, but this is not the sense in which it is used here. With k and z_0 as fixed constants and u_* and d as adjustable parameters, nonlinear regression is used to acquire the best fit to the measured wind speed profile, an example of which is given in Fig. 4.8b. In the case of the RHI scans, the spatial turbulence intensity is calculated by dividing the RMSD of the fit by the modeled wind speed at hub height, which also corresponded roughly to

the average measurement height of the scans. For the example in Fig. 4.8, RMSD = 1.58 m s^{-1} and u = 8.24 m s^{-1} at hub height, such that I_{space} = 19%.

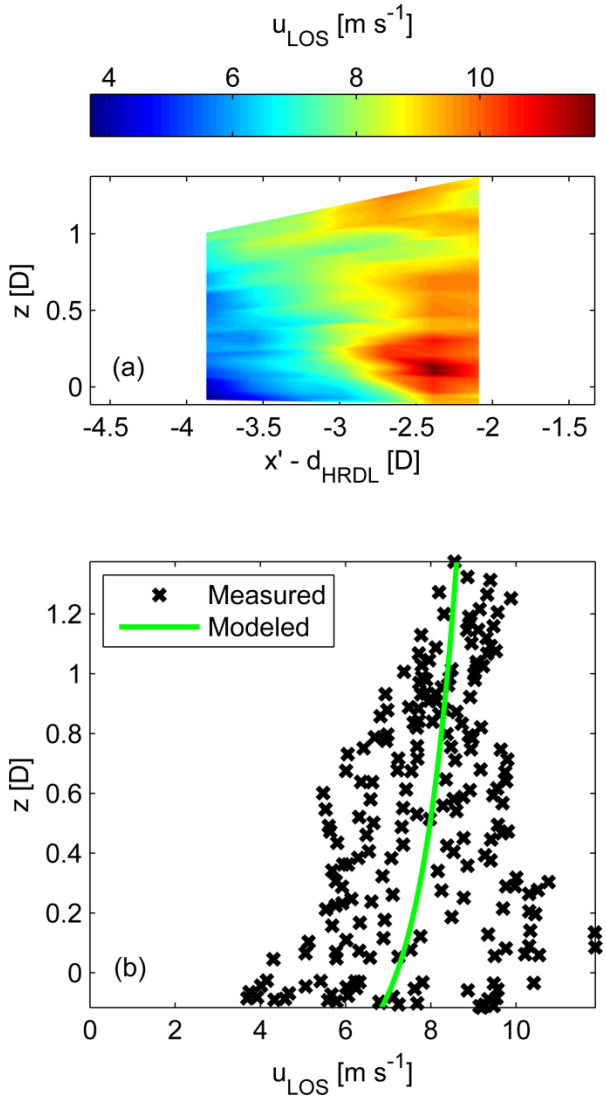

Fig. 4.8. (a) The inflow to the turbine in the same RHI scan as that depicted in Fig. 4.6 and (b) the best-fit model of the measured wind speed profile, which is assumed to be logarithmic.

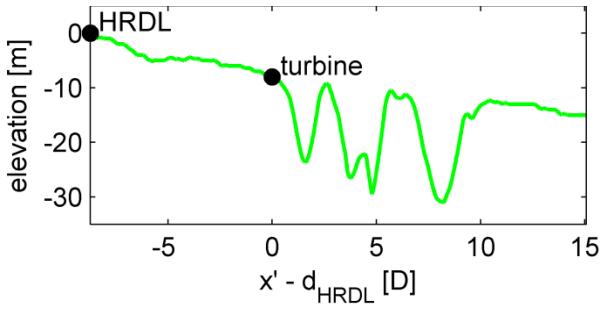

Fig. 4.9. Elevation profile along the LOS from HRDL to the turbine.

The distributions of spatial turbulence intensity for the PPI and RHI scans over the duration of the experiment are shown in Fig. 4.10. The RHI scans feature relatively lower spatial turbulence according to the definition given here—note that the distribution peaks around $I_{space} = 30\%$ for the PPI scans, and $I_{space} = 10\%$ for the RHI scans. In the following discussion, low (high) spatial turbulence intensity is defined as being less (greater) than 30% for the PPI scans, whereas $I_{space} = 10\%$ is taken to be the value separating these two categories for the RHI scans.

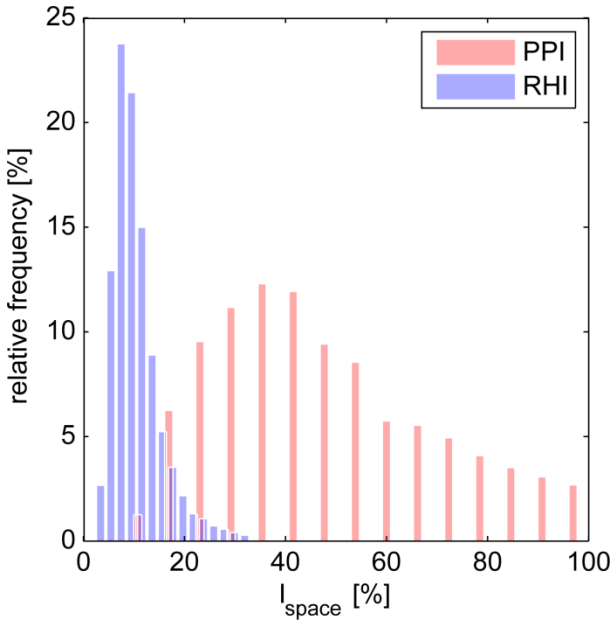

Fig. 4.10. Distribution of spatial turbulence intensity measurements throughout the course of the TWICS campaign for the PPI (red) and RHI (blue) scans.

4.3.2 Windcube lidar

Positioned about 300 m to the west-northwest of the turbine, the Windcube collected wind speed and direction profiles from 40 m up to 200 m above ground level (AGL), depending on atmospheric conditions (Cariou 2011; Chapter 3). Technical specifications are given in Table 4.3. Windcube measurements were used to seed and check the accuracy of the wake detection algorithms described in Section 4.3.4.

Table 4.3. Windcube technical specifications.

Laser wavelength	1.54 μm
Pulse energy	10 μJ
Pulse rate	20 kHz
Data output frequency	1 Hz

Range min-max	40–200 m
Probed volume	20 m
Measurement heights	10
Scanning cone angle	30°
Speed accuracy	0.2 m s^{-1}
Direction accuracy	1.5°

4.3.3 Meteorological tower

The met tower is located about 1 km to the west-northwest of the turbine, as shown in Fig. 4.3. Wind speed and direction data were collected at 2, 5, 10, 20, 50, and 80 m AGL on the met tower using Met One SS-201 cup anemometers and Met One SD-201 wind vanes, respectively. Wind speeds were measured with an accuracy of the greater of 2% of reading or 0.5 m s^{-1}, while wind directions were measured with an accuracy of 3.6°. Additionally, air temperature was measured with an accuracy of 0.1 °C using Met One T200A platinum resistance thermometers at 2, 50, and 80 m AGL. Measurements of dew point and barometric pressure were also taken at 2 m AGL. At each measurement height, data were collected at 1 Hz and then stored as 10-min averages (Johnson and Kelley 2000). The met tower data and instrumentation documentation are publicly available and can be downloaded from <http://www.nrel.gov/midc/nwtc_m2/>.

Met tower observations were used to calculate the bulk Richardson number, defined as

$$\mathrm{Ri}_B = \frac{g}{\overline{\theta_v}} \frac{\Delta\theta_v \Delta z}{(\Delta u)^2}, \tag{4.4}$$

where g is gravitational acceleration, $\overline{\theta_v}$ is mean virtual potential temperature, $\Delta\vartheta_v$ is the virtual potential temperature difference across a layer of thickness Δz, and Δu is the change in horizontal wind speed across that same layer (Stull 1988). Atmospheric stability was determined using calculations of Ri_B between 2 and 80 m AGL, with $\mathrm{Ri}_B <$ -0.03, $|\mathrm{Ri}_B| < 0.03$, and $\mathrm{Ri}_B > 0.03$ indicating unstable, neutral, and stable conditions, respectively (see Fig. 4.11 for the distribution of Ri_B during the experiment). Given the accuracy of the temperature and wind speed sensors, the uncertainty in Ri_B is estimated to be about 0.02 on average. The stability classifications were chosen to divide the amount of data roughly into thirds and to avoid overlap between the unstable and stable categories arising from the uncertainty in Ri_B. The 2–80 m layer—as opposed to the 2–50 m or 50–80 m layers—was chosen to maximize the $\Delta\vartheta_v$ measurement (and therefore minimize the uncertainty in Ri_B) and because measurements of conditions near the surface are important for characterizing atmospheric stability.

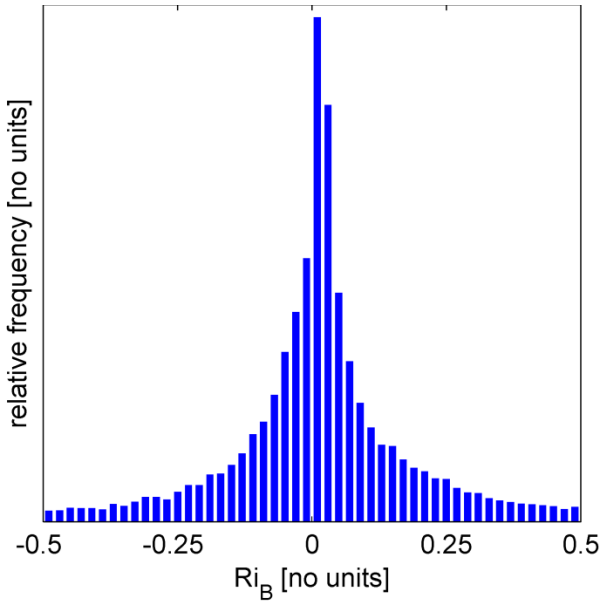

Fig. 4.11. Distribution of Ri_B for the duration of the TWICS campaign.

4.3.4 HRDL data processing

HRDL LOS velocity measurements were disregarded when the corresponding SNR was less than -15 dB. In addition, for each scan, measurements that did not lie within three standard deviations of the median were identified as outliers and removed from the analysis (W. A. Brewer 2011, personal communication). Most outliers were the result of hard target strikes—such as the laser beam hitting the wind turbine tower or rotor blades—or signal drop off. Expanding upon the work of Bingöl et al. (2010) and Trujillo et al. (2011), a set of statistical models is developed below to extract various wake attributes from the HRDL measurements using weighted nonlinear regression, in which observation weights are specified using the Cramér-Rao lower bound, as discussed previously.

4.3.4.1 One-dimensional PPI algorithm

As depicted in Fig. 4.12, a coordinate system centered at HRDL is defined with longitudinal axis x' pointing from HRDL to the turbine and transverse axis y', which is perpendicular to the x'-axis. The polar coordinates of a point in the field are specified by (r,ϑ), with $r=\sqrt{x'^2+y'^2}$ as the HRDL range gate and $\theta=\arctan(y'/x')$ as the HRDL azimuth angle, whereby $\vartheta>0$ ($\vartheta<0$) for clockwise (counterclockwise) rotations.

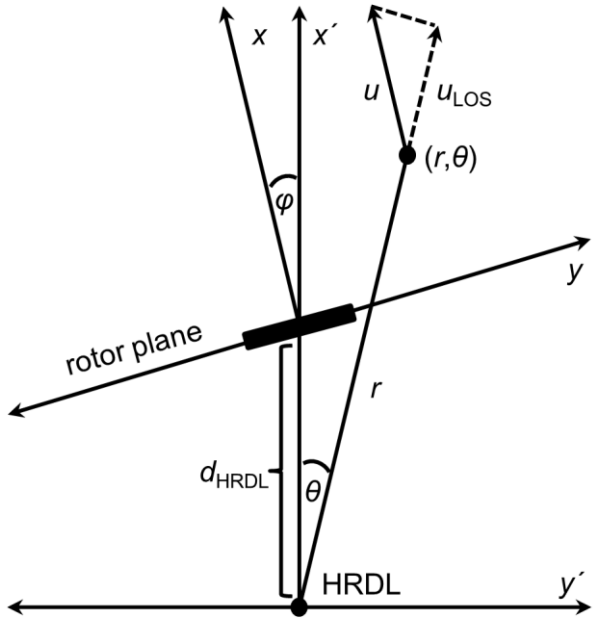

Fig. 4.12. Plan view of the coordinate systems used for the PPI models.

To determine the horizontal structure of the wake from the PPI scans, the ambient wind is modeled with uniform speed u and direction φ, an angle with the same conventions as ϑ. Because the angle between the HRDL LOS and the vector describing

the flow field at a given point is $|\vartheta - \varphi|$, the HRDL-measured LOS velocity is the actual wind speed modified by the function $\cos(\vartheta - \varphi)$, which can be rewritten as

$$\begin{aligned}\cos(\theta - \phi) &= \cos\theta\cos\phi + \sin\theta\sin\phi \\ &= \frac{\sqrt{r^2 - y'^2}}{r}\cos\phi + \frac{y'}{r}\sin\phi\,.\end{aligned} \tag{4.5}$$

The wake itself is modeled as either a single- or symmetric double-Gaussian function subtracted from the uniform background flow, in an attempt to account for the difference between the shape of the VD profile in the near and far wake. For each sweep of the beam, and at each range gate r, three models were fit to the LOS velocity data to identify the wake, if any: a wake-free model

$$u_{\mathrm{LOS}}(y', r) = u\left(\frac{\sqrt{r^2 - y'^2}}{r}\cos\phi + \frac{y'}{r}\sin\phi\right), \tag{4.6}$$

a single-Gaussian wake model

$$u_{\mathrm{LOS}}(y', r) = \left(u - a\exp\left[\frac{-(y' - y_c)^2}{2s_w^2}\right]\right)\left(\frac{\sqrt{r^2 - y'^2}}{r}\cos\phi + \frac{y'}{r}\sin\phi\right), \tag{4.7}$$

and a double-Gaussian wake model

$$\begin{aligned}u_{\mathrm{LOS}}(y', r) = &\left(u - a\left\{\exp\left[\frac{-(y' - y_l)^2}{2s_w^2}\right] + \exp\left[\frac{-(y' - y_r)^2}{2s_w^2}\right]\right\}\right) \\ &\times\left(\frac{\sqrt{r^2 - y'^2}}{r}\cos\phi + \frac{y'}{r}\sin\phi\right).\end{aligned} \tag{4.8}$$

In both Eqs. (4.7) and (4.8), a denotes the amplitude of the Gaussian and s_w is a parameter controlling the width of the wake. In Eq. (4.7), y_c denotes the location of the

wake center, whereas y_l and y_r are used to distinguish the locations of the left and right local minima in Eq. (4.8), respectively. For a given range gate r, y' is the only independent variable. All other variables appearing on the right-hand sides of Eqs. (4.6–4.8) are parameters, whose best-fit values were obtained using nonlinear regression. An extra sum-of-squares F-test was used to determine the simplest model (i.e., the model with the least number of parameters) to fit the data, in which the threshold p-value was set to 0.05. If the p-value was less than 0.05, the simpler model was rejected and the more complicated model was deemed to fit the data significantly better (Kleinbaum et al. 2007).

Traditionally, the velocity deficit has been defined as the percentage difference between the ambient wind speed and that inside the wake (Vermeer et al. 2003):

$$\mathrm{VD} = \frac{u_{ambient} - u_{wake}}{u_{ambient}} \times 100\% = \frac{u - u_{wake}}{u} \times 100\% \,. \tag{4.9}$$

For the single-Gaussian wake, $u_{wake} = u - a$, so the velocity deficit is given by

$$\mathrm{VD} = \frac{u - (u - a)}{u} \times 100\% = \frac{a}{u} \times 100\% \,. \tag{4.10}$$

In addition, the single-Gaussian wake width is defined to be the size of the 95% confidence interval of the velocity deficit profile,

$$w = 4s_w \,, \tag{4.11}$$

as mentioned in Section 4.2.3. On the other hand, for the double-Gaussian wake, VD is calculated by taking u_{wake} to be the minimum modeled wind speed inside the wake, while the wake width is calculated as

$$w = (y_r + 2s_w) - (y_l - 2s_w) = y_r - y_l + 4s_w \,. \tag{4.12}$$

Using the subscript "0" to denote initial coefficient estimates, seeding for the regression algorithm proceeded for each range gate r as follows: φ_0 was set to correspond to the median Windcube-measured wind direction at hub height (80 m) over the duration of the beam sweep (~20 s), u_0 to the median HRDL-measured LOS velocity for the range gate of interest, a_0 to the difference between u_0 and the minimum HRDL-measured LOS velocity, y_{c0} to the y-coordinate of the minimum HRDL-measured LOS velocity (in the double-Gaussian case, y_{l0} and y_{r0} were set to the y-coordinates of the two smallest HRDL-measured LOS velocities), and s_{w0} to 0.25D (a value corresponding to a wake width of one rotor diameter).

An example model fit at a distance of 2D behind the turbine is shown in Fig. 4.13, in which the parameters were estimated as φ = -26.6 deg, u = 14.5 m s^{-1}, a = 7.2 m s^{-1}, y_c = -0.99D, and s_w = 0.42, such that VD = 49.6% and w = 1.7D. Furthermore, the ability of the one-dimensional PPI algorithm to capture the meandering of the wake centerline is demonstrated in the top panel of Fig. 4.14, in which the black line indicates the estimates of y_c for all range gates included in the scan.

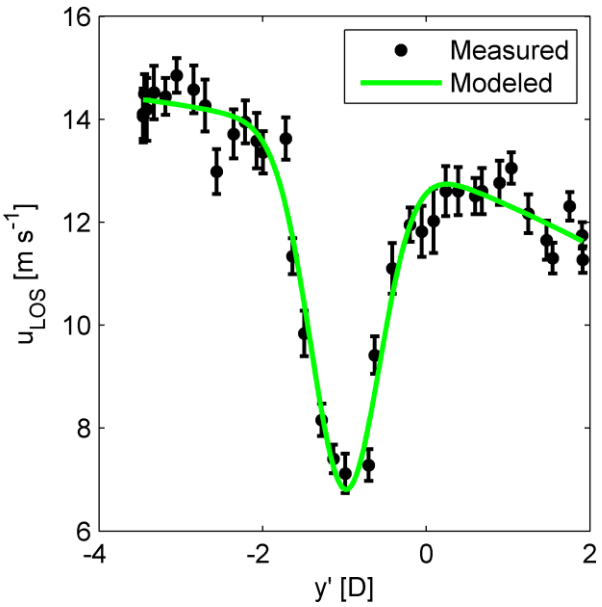

Fig. 4.13. The one-dimensional PPI model of the flow at a downstream distance of 2D in the scan of Fig. 5. The discrete points and the line indicate actual HRDL measurements and the curve of best-fit, respectively.

4.3.4.2 Two-dimensional PPI algorithm

A quicker (but perhaps less robust) method for determining the horizontal wake structure from the PPI scans is to fit all of the LOS measurements from a single beam sweep to a two-dimensional model, in which the ambient flow is assumed to have uniform speed u and direction φ, as before. Letting $d_{\mathrm{HRDL}} = 880$ m $= 8.8$D be the distance between HRDL and the wind turbine, a new unprimed coordinate system is defined to be related to the primed coordinate system of the previous section through the following transformation

$$\begin{bmatrix} x \\ y \end{bmatrix} = \begin{bmatrix} \cos\phi & \sin\phi \\ -\sin\phi & \cos\phi \end{bmatrix} \begin{bmatrix} x' - d_{\mathrm{HRDL}} \\ y' \end{bmatrix}. \tag{4.13}$$

Note that the unprimed coordinate system is centered at the turbine and rotated from the primed system by the angle φ, such that, ignoring yaw misalignment and wake meandering, the x-axis is aligned with the wake centerline (see Fig. 4.12). As before, the wake is represented as having a Gaussian profile, with the velocity deficit and width following the power laws

$$\mathrm{VD}(x) = \mathrm{VD}_0 \left(\frac{x}{D}\right)^n \text{ and} \tag{4.14}$$

$$s(x) = s_0 \left(\frac{x}{D}\right)^m, \tag{4.15}$$

where VD is written as a decimal and not a percentage, and VD_0, s_0, n, and m are parameters. Similar to the one-dimensional PPI case, two models were fit to the LOS velocity data to identify the wake, if any: a wake-free model

$$u_{\mathrm{LOS}}(x,y) = u\cos(\theta - \phi) \tag{4.16}$$

and a wake model

$$\begin{aligned} u_{\mathrm{LOS}}(x,y) &= u\left(1 - \mathrm{VD}(x)\exp\left[-\frac{y^2}{2\left(s(x)\right)^2}\right]\right)\cos(\theta-\phi) \\ &= u\left(1 - \mathrm{VD}_0\left(\frac{x}{D}\right)^n \exp\left[-\frac{y^2}{2s_0^2(x/D)^{2m}}\right]\right)\cos(\theta-\phi)\,. \end{aligned} \tag{4.17}$$

Note that $\theta = \arctan(y'/x')$ is an implicit function of x and y, since the primed coordinates are related to the unprimed coordinates via the inverse of Eq. (4.13)

$$\begin{bmatrix} x' \\ y' \end{bmatrix} = \begin{bmatrix} d_{\mathrm{HRDL}} \\ 0 \end{bmatrix} + \begin{bmatrix} \cos\phi & -\sin\phi \\ \sin\phi & \cos\phi \end{bmatrix} \begin{bmatrix} x \\ y \end{bmatrix}, \tag{4.18}$$

so that x and y are the independent variables in Eq. (4.17). As before, an extra sum-of-squares F-test was used to determine the most appropriate model to fit the data, with the threshold p-value = 0.05.

As in the one-dimensional PPI model, for each beam sweep, φ_0 was set such that the wake centerline was aligned with the median Windcube-measured wind direction at 80 m during the duration of the sweep, and u_0 was set to the median HRDL-measured LOS velocity. The other initial coefficient estimates were $\mathrm{VD}_{00} = 0.56$, $s_{00} = 0.33\mathrm{D}$, $n_0 = -0.57$, and $m_0 = 0.33$, values corresponding to the fits of previous wake measurements from Section 4.2. An example model fit is shown in Fig. 4.14b, in which the parameters were estimated as $\varphi = -28.3$ deg, $u = 15.6$ m s^{-1}, $\mathrm{VD}_0 = 0.81$, $s_0 = 0.37\mathrm{D}$, $n = -0.79$, and $m = 0.37$. While of course not capturing any wake meandering, the model reasonably estimates the mean features of the ambient flow and wake.

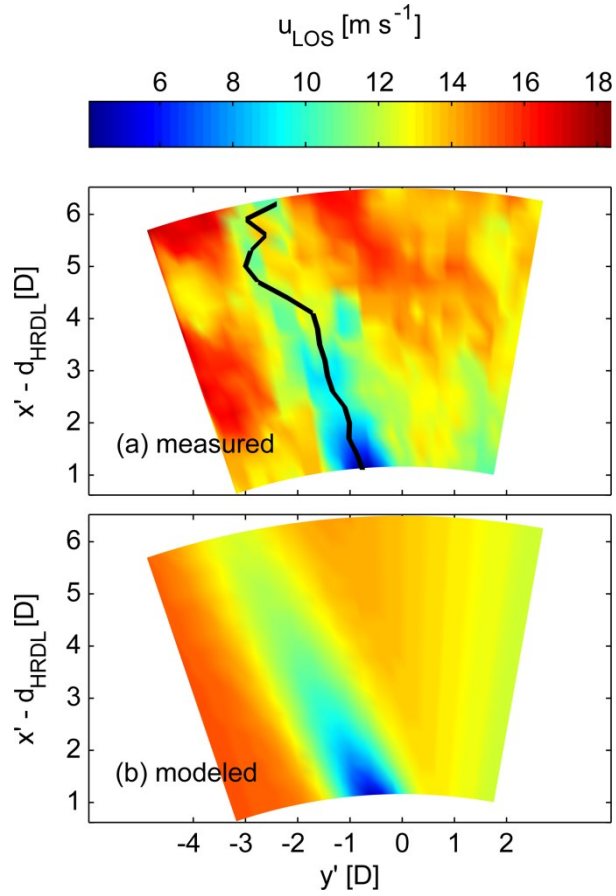

Fig. 4.14. The two-dimensional PPI model (b) of the flow in the scan of Fig. 5, which is repeated here for comparison (a). The black line in the top panel denotes the location of the wake centerline as captured by the one-dimensional PPI algorithm.

4.3.4.3 RHI algorithm

A diagram of the coordinate systems used to analyze the vertical structure of the wake from the RHI scans is shown in Fig. 4.15. As before, r denotes the HRDL range gate, while δ specifies the HRDL elevation angle. Similar to the one-dimensional PPI case, the wake is modeled as either a single- or symmetric double-Gaussian function subtracted from the background flow, which is taken to follow the logarithmic profile of

Eq. (4.3). For each sweep of the beam, and at each range gate r, three models were fit to the LOS velocity data to determine the structure of the wake, if any: a wake-free model

$$u_{\mathrm{LOS}}(z,r) = \frac{u_*}{k}\ln\left[\frac{z-d}{z_0}\right]\cos\delta = \frac{u_*}{k}\ln\left[\frac{z-d}{z_0}\right]\sqrt{1-\left(\frac{z}{r}\right)^2}, \tag{4.19}$$

a single-Gaussian wake model

$$u_{\mathrm{LOS}}(z,r) = \left(\frac{u_*}{k}\ln\left[\frac{z-d}{z_0}\right] - a\exp\left[\frac{-(z-z_c)^2}{2s_h^2}\right]\right)\sqrt{1-\left(\frac{z}{r}\right)^2}, \tag{4.20}$$

and a double-Gaussian wake model

$$u_{\mathrm{LOS}}(z,r) = \left(\frac{u_*}{k}\ln\left[\frac{z-d}{z_0}\right] - a\left\{\exp\left[\frac{-(z-z_l)^2}{2s_h^2}\right] + \exp\left[\frac{-(z-z_u)^2}{2s_h^2}\right]\right\}\right) \times\sqrt{1-\left(\frac{z}{r}\right)^2}. \tag{4.21}$$

Similar to the PPI models, a denotes the amplitude of the Gaussian and the parameter s_h controls the height of the curve. In the single-Gaussian case, z_c denotes the vertical location of the wake center, whereas z_l and z_u are used to distinguish the locations of the lower and upper local minima for the double-Gaussian case, respectively. Here, z is the independent variable, whereas all other variables appearing on the right-hand sides of Eqs. (4.19–4.21) are parameters, with the exception of k and z_0, which are fixed. An extra sum-of-squares F-test was used to determine the simplest model to fit the data, again with the threshold p-value = 0.05.

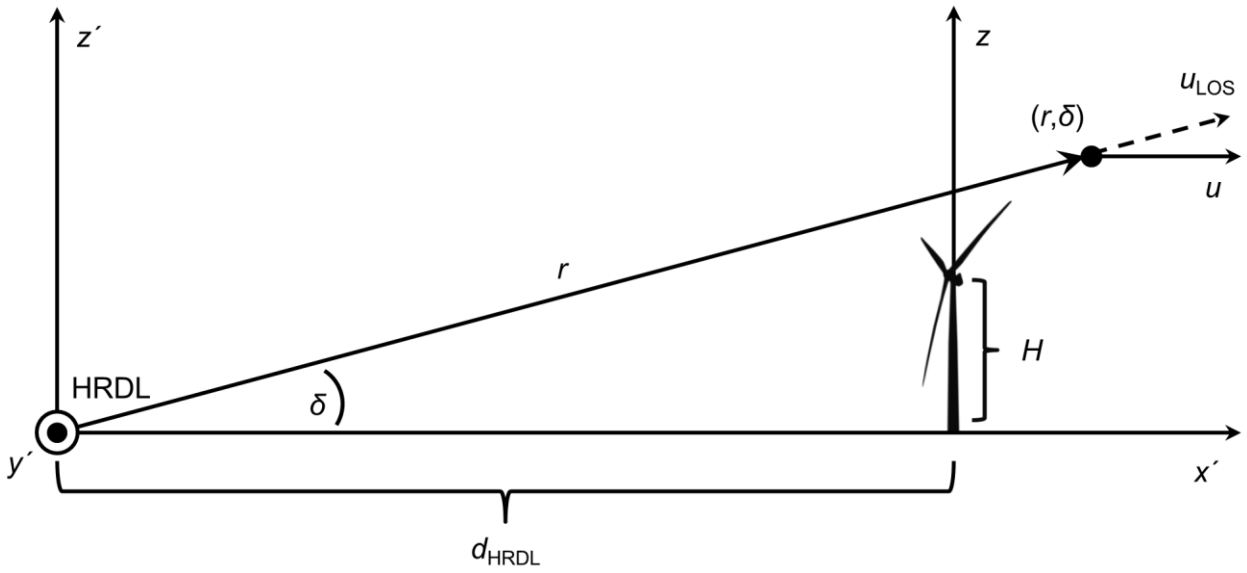

Fig. 4.15. Side view of the coordinate systems used for the RHI model.

For each beam sweep, the initial estimate for u_* was set equal to the modeled value as determined by the HRDL freestream measurements (see Section 4.3.1), and d_0 was set equal to -10 m, which corresponds roughly to the elevation of the terrain at the turbine relative to HRDL. Furthermore, a_0 was set to the difference between the median and minimum HRDL-measured LOS velocities, z_{c0} to $H = 0.8\text{D} = 80$ m (in the double-Gaussian case, z_{l0} and z_{u0} were set to $H - 0.25\text{D} = 0.55\text{D} = 55$ m and $H + 0.25\text{D} = 1.05\text{D} = 105$ m, respectively), and s_{h0} to $0.25\text{D} = 25$ m.

Similar to the PPI case, the velocity deficit for the RHI scans is calculated using Eq. (4.9), in which

$$u_{ambient} = \frac{u_*}{k} \ln\left[\frac{z_c - d}{z_0}\right] \tag{4.22}$$

is the estimated ambient wind speed at the vertical location of the wake center. For the single-Gaussian wake, $u_{wake} = u_{ambient} - a$, so the velocity deficit is given by

$$\mathrm{VD} = \frac{a}{u_{ambient}} \times 100\% \,. \tag{4.23}$$

In addition, the single-Gaussian wake height is defined to be the size of the 95% confidence interval of the velocity deficit profile:

$$h = 4s_h \,. \tag{4.24}$$

On the other hand, for the double-Gaussian wake, the velocity deficit is calculated by taking u_{wake} to be the minimum modeled wind speed inside the wake, while the wake height is defined as

$$h = (z_u + 2s_h) - (z_l - 2s_h) = z_u - z_l + 4s_h \tag{4.25}$$

The effective vertical location of the wake center in the double-Gaussian case is taken to be $z_c = (z_l + z_u)/2$.

An example model fit at a distance 1D behind the turbine is shown in Fig. 4.16, in which the parameters were estimated as $u_* = 0.493$ m s^{-1}, $d = 35.9$ m, $a = 8.10$ m s^{-1}, $z_c = 40.4$ m $= 0.505H$, and $s_h = 38.4$ m, such that VD = 70% and $h = 154$ m $= 1.54$D. Note that z_c is normalized by H, since the maximum velocity deficit is expected to occur near hub height, and that h is normalized by D, to facilitate comparison to the wake width.

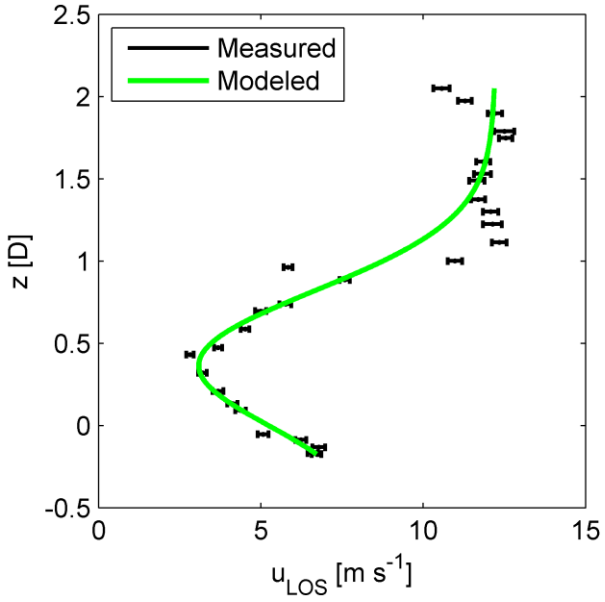

Fig. 4.16. The RHI model of the flow at a downstream distance of 1D in the scan of Fig. 6. The discrete points and the line indicate actual HRDL measurements and the curve of best-fit, respectively.

4.3.4.4 Model acceptance criteria

Using the above algorithms, wake parameters were determined for every beam sweep in the HRDL dataset. In addition to the extra sum-of-squares F-test used to find the best-fit models, some models were rejected for having unusual parameter estimates. If, for a particular model fit, any parameter or confidence interval fell outside three standard deviations of the respective median value, the fit was deemed an outlier and disregarded. Moreover, model fits with unphysical parameter estimates were also eliminated from the analysis. Specifically, in both the one-dimensional PPI and RHI algorithms, a wake is necessarily characterized by $0 < a < u_{ambient}$ because $0\% <$ VD $<$

100% by definition. Because of unusually large ambient variability, undetected hard target strikes, or signal dropout, the algorithms could occasionally determine a to be outside of the valid range; such unphysical model fits were excluded from consideration.

4.4 Results

4.4.1 Velocity deficit profile

A total of 5971 (3926) beam sweeps were evaluated using the one-dimensional PPI (RHI) algorithms. Figs. 4.17a and 4.17b show, as a function of downwind distance, the percentage of scans for which a physical wake was modeled with sufficient goodness-of-fit—as determined by the F-test—by these respective algorithms. (As an aside, the two-dimensional PPI algorithm detected a wake in about 20% of the scans.) In both cases, the number of detected wakes decreased with downwind distance, as the velocity deficit scaled more with the variability in the ambient flow. The scans, moreover, eventually sampled the flow outside the wake at longer range gates due to the geometrical constraints mentioned earlier, so wakes were detected on average out to about $x = 7$D, although longer wakes were certainly identified on an individual basis. Surprisingly, the PPI algorithm detected far more single-Gaussian than double-Gaussian wakes even at short distances just behind the turbine, suggesting that the azimuth scan rate was slightly too fast to resolve the double-Gaussian structure of the near wake in many cases. This deficiency could perhaps be corrected in a future study by slowing the

PPI scan azimuth rate, such that more measurements are taken in a single beam sweep. Because the beam azimuth had to be more or less aligned with the wake centerline for an RHI scan to capture a meaningful portion of the wake, the RHI algorithm detected relatively fewer overall wakes than the PPI algorithm. With finer angular resolution, however, the RHI scans seem to do a better job of detecting the double-Gaussian shape in the near wake. In general, the ratio of single- to double-Gaussian wakes was measured to generally increase with downwind distance, as turbulent mixing caused the two troughs in the initial velocity profile to later merge into a single trough. A well-defined demarcation of the near and far wake was not observed, and a small number of double-Gaussian wakes are detected at longer range gates. Again, the shape of the velocity deficit profile in both the near and far wake is expected to be better resolved by slowing the lidar scan rate.

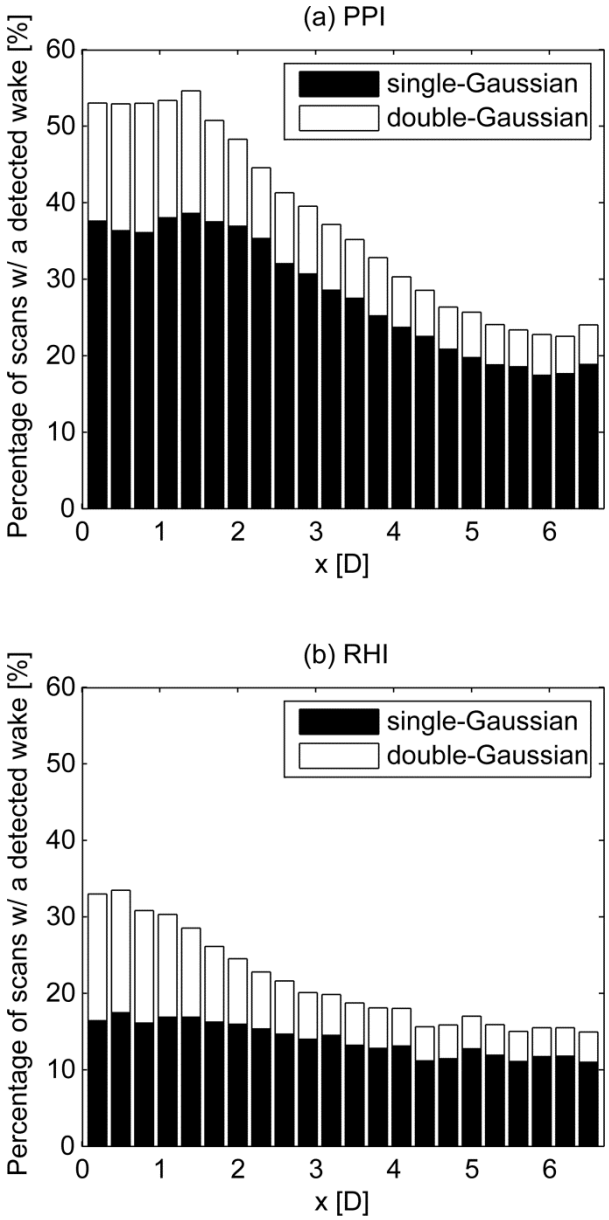

Fig. 4.17. Percentage of scans for which a physical wake was modeled with sufficient goodness-of-fit by (a) the one-dimensional PPI algorithm and (b) the RHI algorithm, as a function of downwind distance.

4.4.2 Velocity deficit attenuation

In Figs. 4.18–4.20, velocity deficit is plotted as a function of downwind distance, as determined by the one-dimensional PPI, two-dimensional PPI, and RHI algorithms,

respectively. Here, the shaded error bars in each plot encompass both (1) inherent inter-individual variability in the parameter estimates, since lidar scans were taken under a range of wind speeds, turbulence levels, and stability conditions, and (2) error in the estimation procedure itself. This stipulation is true of the error bars in later figures, as well. In general, the deficit was found to decrease as faster moving air was entrained within the wake, as expected. Notably, significant velocity deficits were still apparent even as far as 6–7D behind the turbine. The RHI scans measured a somewhat lower velocity deficit than the PPI scans, presumably because the RHI scans did not transect the central part of the wake as often.

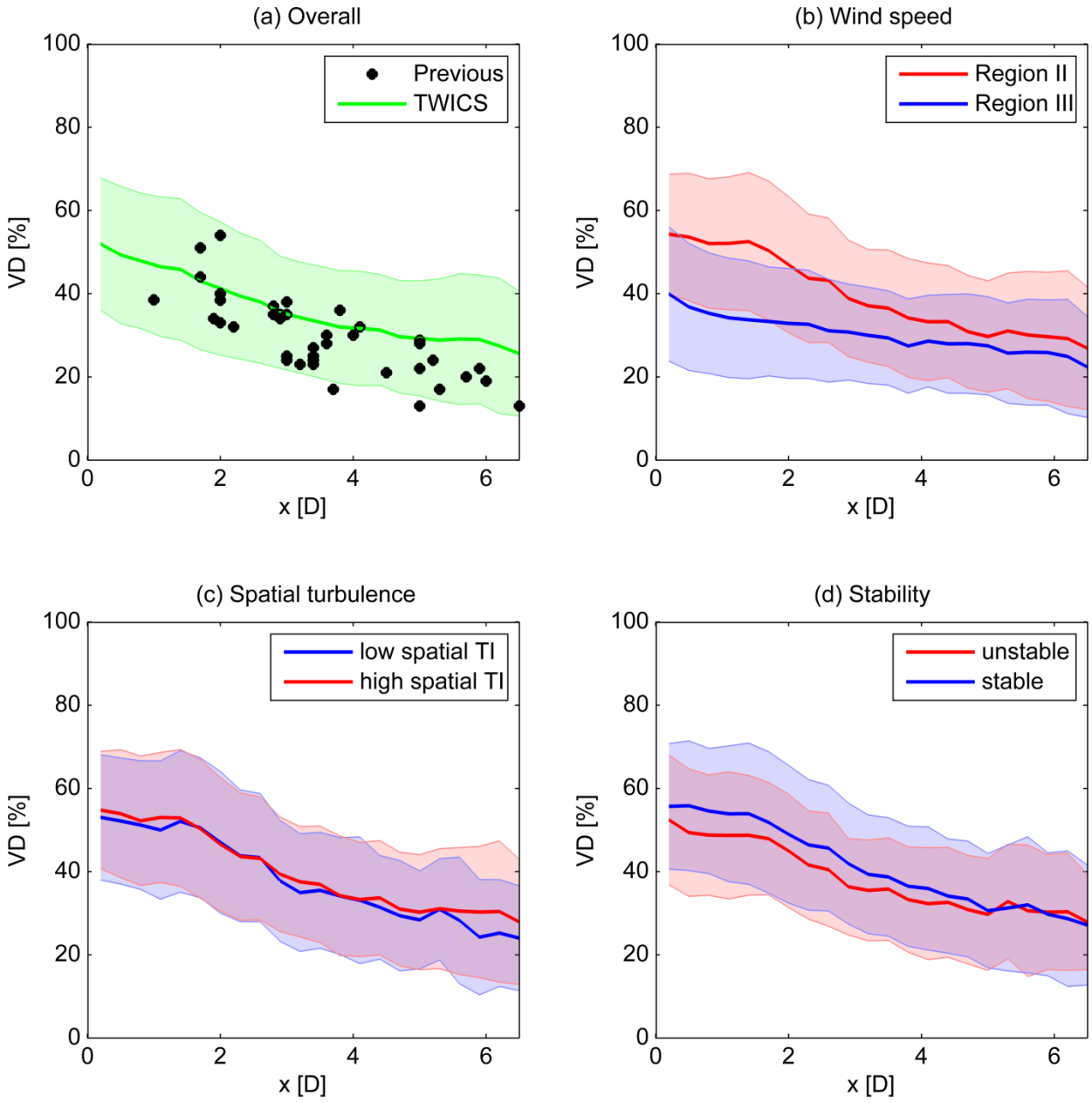

Fig. 4.18. Velocity deficit versus downwind distance, as determined by the one-dimensional PPI algorithm. In each subplot, the bold central lines indicate median values, while the symmetric shaded error bars represent the standard deviation of the measurements. TWICS results are compared to those of previous studies (see Fig. 1) in (a), while velocity deficit measurements are further categorized by (b) ambient wind speed, (c) spatial turbulence, and (d) atmospheric stability.

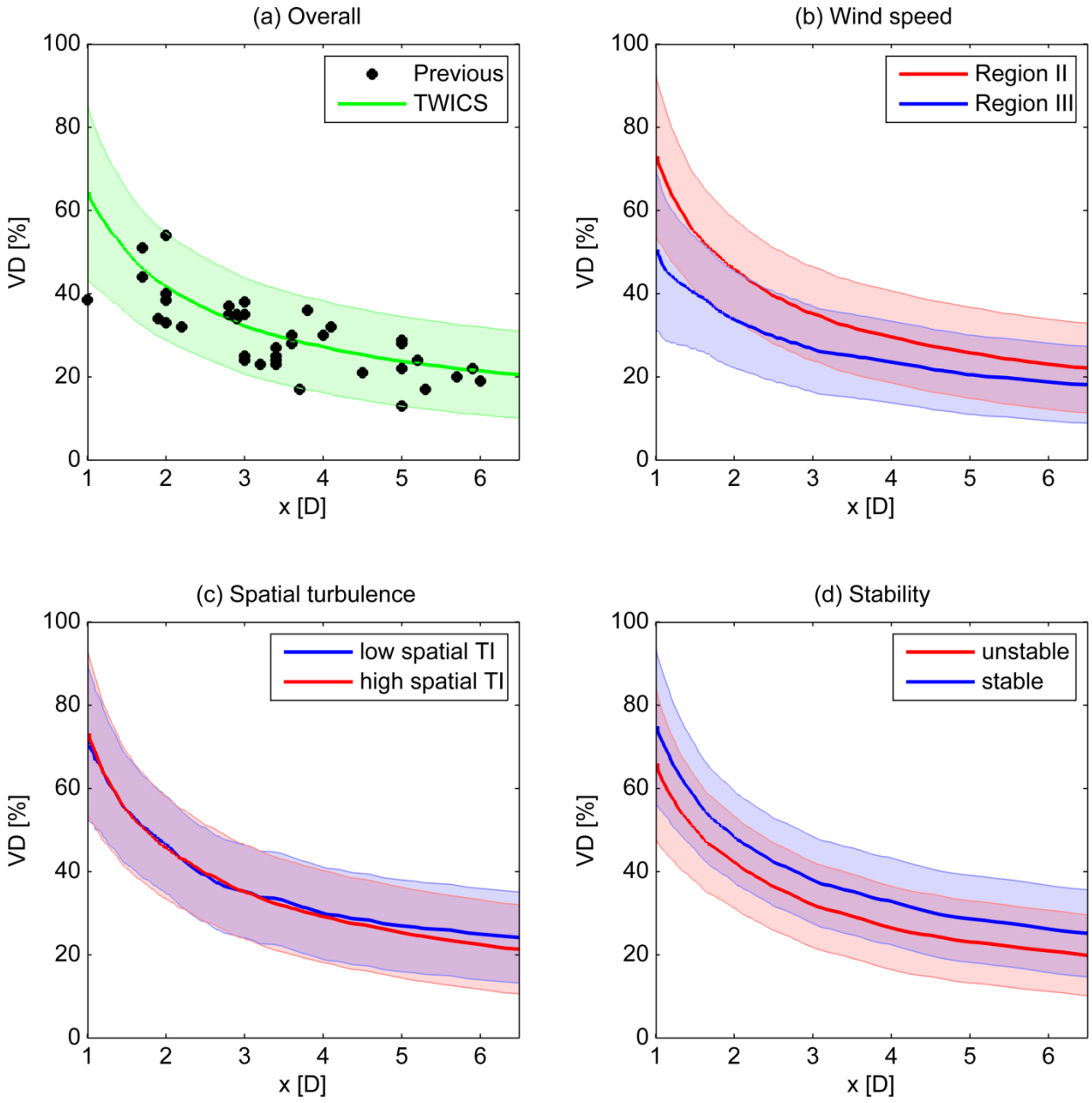

Fig. 4.19. Velocity deficit versus downwind distance, as determined by the two-dimensional PPI algorithm. In each subplot, the bold central lines indicate median values, while the symmetric shaded error bars represent the standard deviation of the measurements. TWICS results are compared to those of previous studies (see Fig. 1) in (a), while velocity deficit measurements are further categorized by (b) ambient wind speed, (c) spatial turbulence, and (d) atmospheric stability.

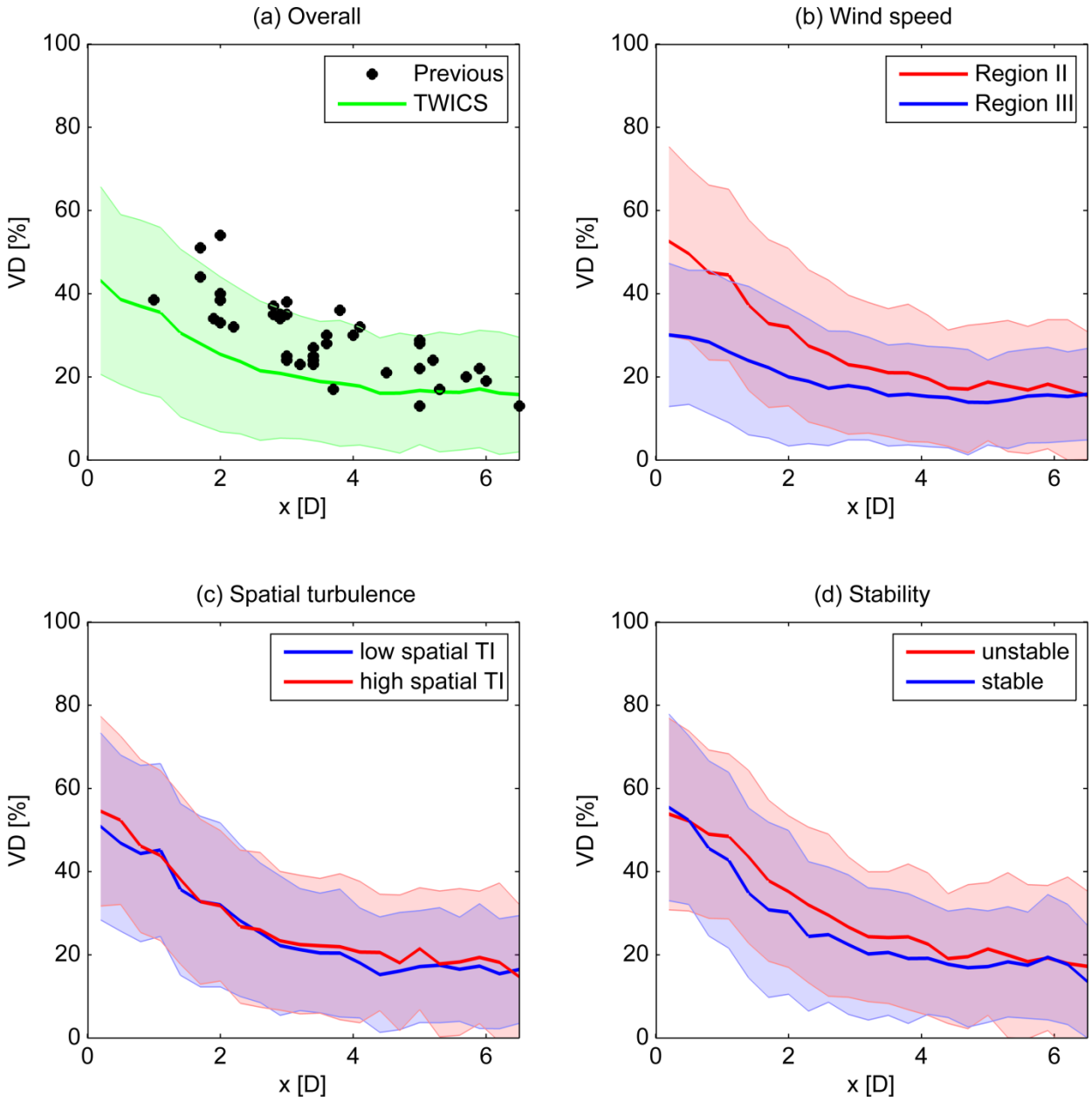

Fig. 4.20. Velocity deficit versus downwind distance, as determined by the RHI algorithm. In each subplot, the bold central lines indicate median values, while the symmetric shaded error bars represent the standard deviation of the measurements. TWICS results are compared to those of previous studies (see Fig. 1) in (a), while velocity deficit measurements are further categorized by (b) ambient wind speed, (c) spatial turbulence, and (d) atmospheric stability.

Despite significant overlap between subgroups when categorizing the results by ambient conditions, it is perhaps instructive to qualitatively examine the median results. As seen in Figs. 4.18–4.20b, wind speed—as measured at 80-m by the Windcube—had the most pronounced effect on controlling the magnitude of the velocity deficit, especially in the near wake, with differences of 10–20% between Region II (below rated power; $4 < u < 12$ m s^{-1}) and Region III (at rated power; $u > 12$ m s^{-1}) of the power curve. The initial velocity deficit is a function of the amount of momentum extracted by the turbine from the ambient flow, and therefore of the turbine thrust coefficient, which is usually highest at cut-in and decreases with wind speed (Emeis 2013). In the case of turbulence (Figs. 4.18–4.20c), there are two competing influences: higher turbulence levels should (1) cause the velocity deficit to recover more quickly, but (2) preclude the detection of relatively small velocity deficits. These two effects seem to more or less cancel out. The influence of stability on the rate of velocity deficit attenuation (Figs. 4.18–4.20d) is similarly difficult to discern from the results here, likely because of the physical setup at the site: typically, flow originating at a glacier passes down a mountain over a forest, and then spends just a few minutes of transit time over some rolling grassland before landing at the NWTC. The effect of local stability on the flow is probably rather weak in this situation.

Simply to check the accuracy of the ambient wind direction and speed estimates by the two-dimensional PPI algorithm (and to perhaps inspire confidence in the estimated wake parameters), the corresponding Windcube measurements at hub height are compared in Fig. 4.21. Here, an individual dot represents the measurements for a single beam sweep. The abscissa is the average Windcube measurement over the duration of the sweep (~20 s), while the ordinate is the corresponding parameter, as estimated by the algorithm, for that sweep. Given the algorithm's assumption of flow uniformity and, moreover, the spatial separation between the different regions of flow sampled by HRDL and the Windcube, the parameter estimates agree quite well with the Windcube measurements: the correlation coefficient for wind direction (speed) is 0.90 (0.79).

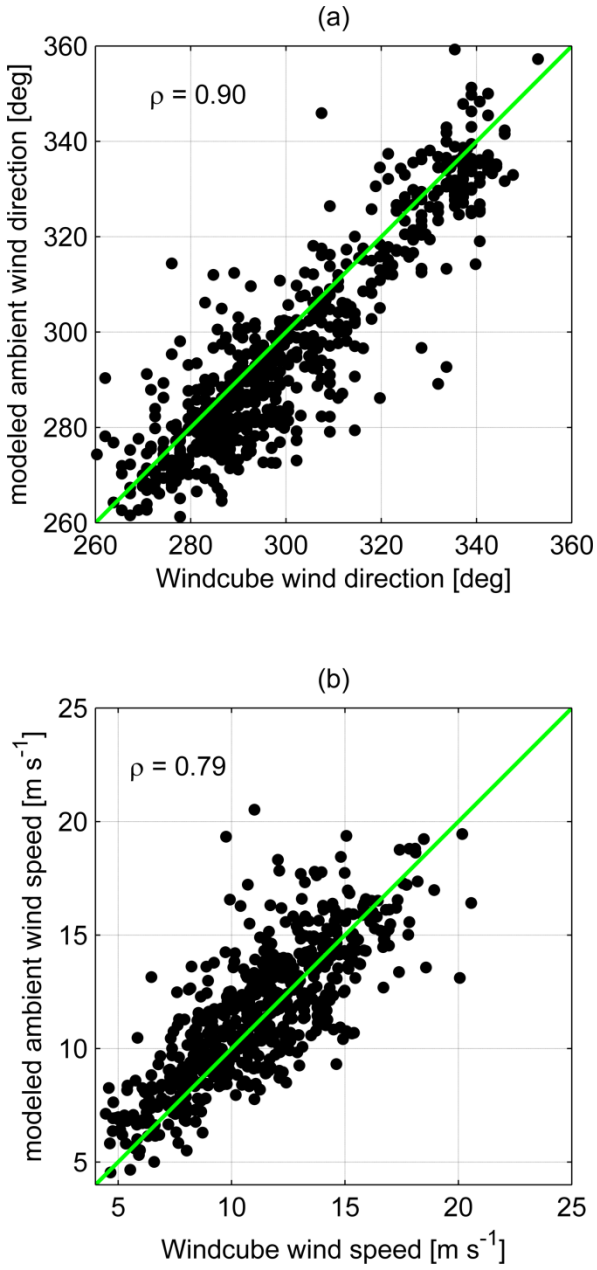

Fig. 4.21. Comparison of (a) wind direction and (b) wind speed measured by the Windcube at hub height and the corresponding ambient values determined by the two-dimensional PPI algorithm. The correlation coefficients for both measurements are given in the upper left of each plot, while the 1:1 line is shown in green.

4.4.3 Wake boundary expansion

Figs. 4.22–4.24 illustrate the growth of the wake boundary with downwind distance, as determined by the one-dimensional PPI, two-dimensional PPI, and RHI algorithms, respectively. Median wake width observations agree well with previous experiments. It is interesting to note that the wake width prediction by the industry-standard Park model (Barthelmie et al. 2006)—using the onshore value for the wake decay constant $k = 0.075$—is not in good agreement with TWICS median results nor those of previous field experiments. Although wind speed did not seem to exhibit much influence on the expansion of the wake, higher turbulence levels and unstable conditions modestly increased the rate at which the wake width expanded in an average sense, owing to more effective mixing between the wake and ambient flow and greater wake meandering.

The standard deviation of the wake width is a result of (1) inherent variability, (2) measurement uncertainty, and (3) wake meandering. For more turbulent conditions and for regions in the far wake, the wake boundary is more diffuse and its detection is therefore less precise. In addition, because each scan took almost one-half minute to complete, the wake width estimate is somewhat influenced by meandering, in which the wake oscillates randomly with amplitude proportional to the magnitude of atmospheric

turbulence (España et al. 2011). Accordingly, the standard deviation of the wake width is greater for high spatial TI and unstable conditions and also increases with x.

Because of the presence of the ground and because of smaller velocity fluctuations—and therefore less meandering—in the vertical plane, the expansion of the wake in the vertical direction was very slight and certainly much less pronounced than in the horizontal. Turbulence and stability did not have as much impact on the wake height, because the wake was not able to expand much at all in the vertical direction.

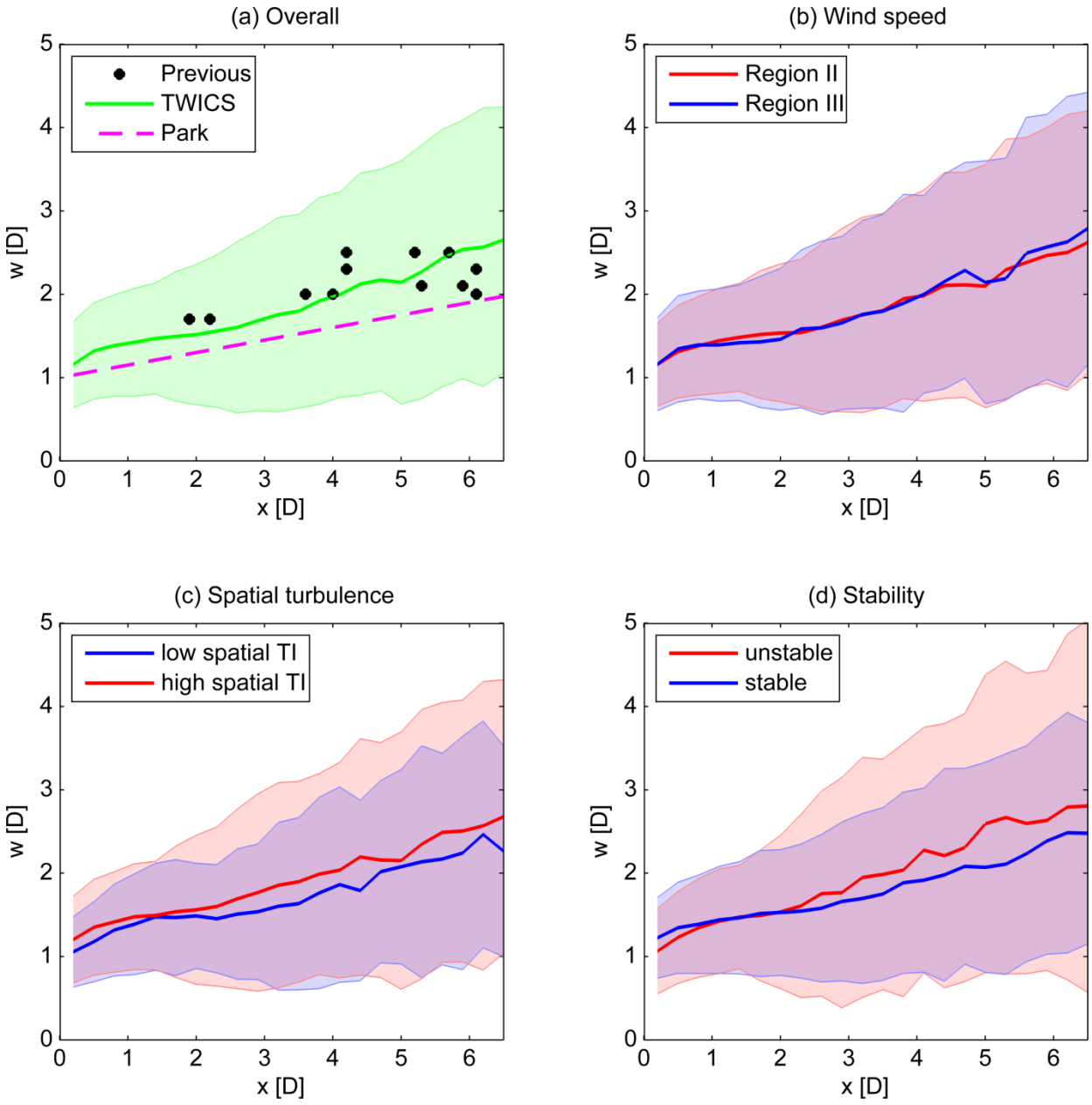

Fig. 4.22. Wake width versus downwind distance, as determined by the one-dimensional PPI algorithm. In each subplot, the bold central lines indicate median values, while the symmetric shaded error bars represent the standard deviation of the measurements. TWICS results are compared to those of previous studies (see Fig. 2) and to the Park wake model in (a), while wake width measurements are further categorized by (b) ambient wind speed, (c) spatial turbulence, and (d) atmospheric stability.

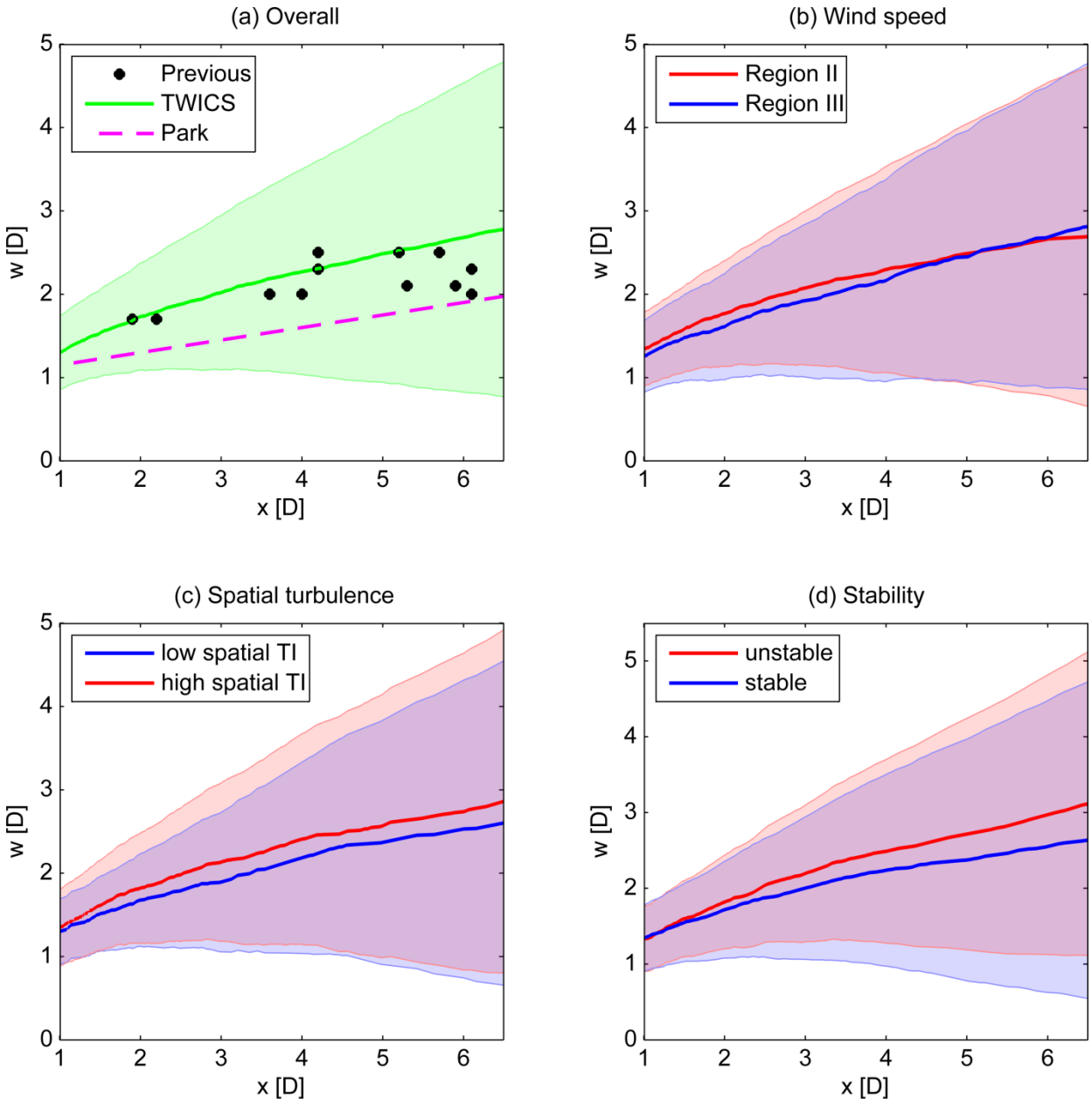

Fig. 4.23. Wake width versus downwind distance, as determined by the two-dimensional PPI algorithm. In each subplot, the bold central lines indicate median values, while the symmetric shaded error bars represent the standard deviation of the measurements. TWICS results are compared to those of previous studies (see Fig. 2) and to the Park wake model in (a), while wake width measurements are further categorized by (b) ambient wind speed, (c) spatial turbulence, and (d) atmospheric stability.

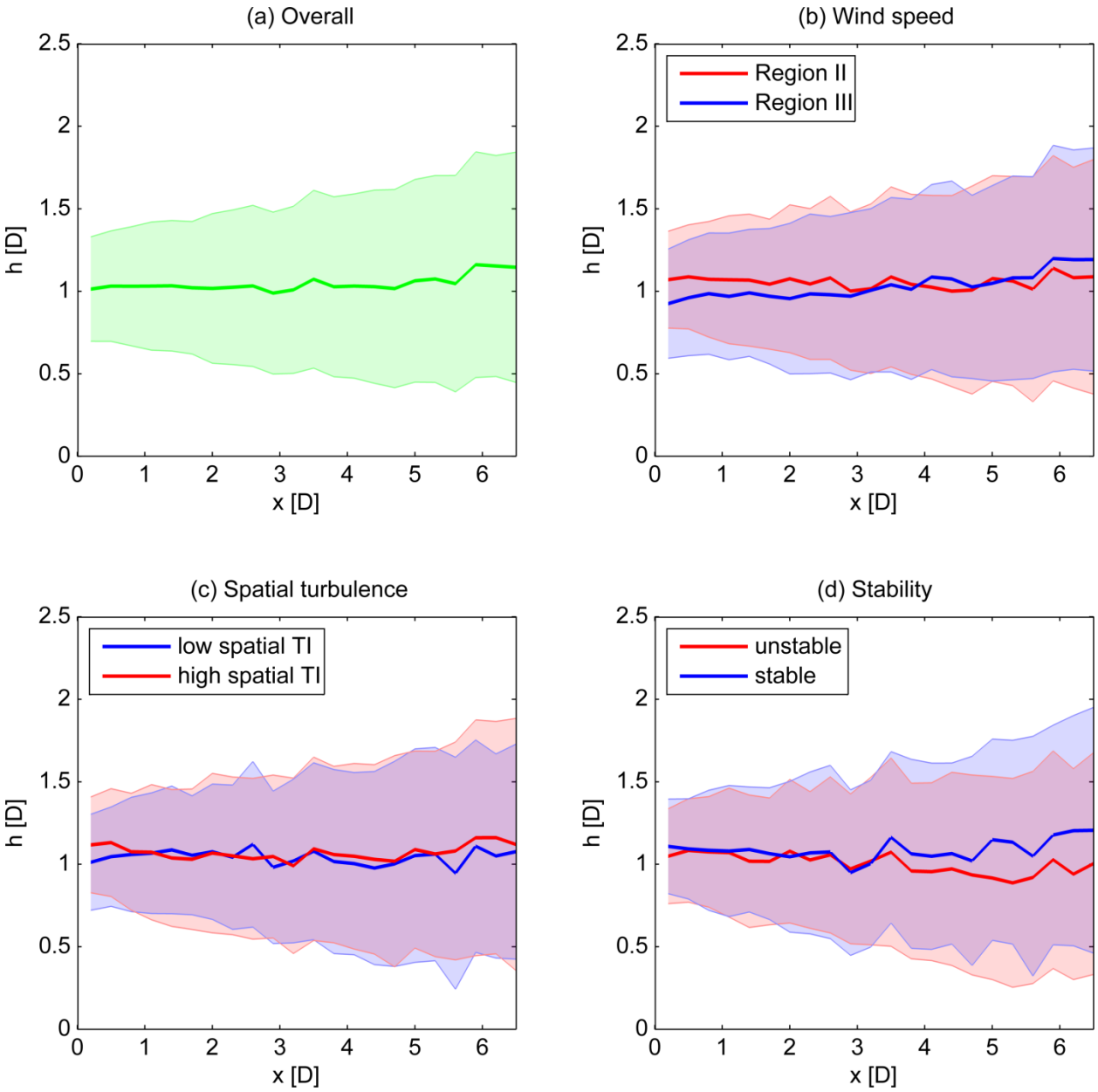

Fig. 4.24. Wake height versus downwind distance, as determined by the RHI algorithm. In each subplot, the bold central lines indicate median values, while the symmetric shaded error bars represent the standard deviation of the measurements. Overall results are shown in (a), while wake height measurements are further categorized by (b) ambient wind speed, (c) spatial turbulence, and (d) atmospheric stability.

4.4.4 Vertical wake structure

Fig. 4.25 shows the estimate of the terrain offset by the RHI algorithm decreasing with distance behind the turbine and following the average overall slope of the terrain. The elevation of the actual terrain was slightly underestimated by the model; a series of simulated RHI scans determined that the model underestimates (overestimates) the elevation of the ground when the wind shear is low (high). Here, the terrain elevation was underestimated on average because the median wind shear exponent, as measured by the Windcube, was just 0.085, less than the value of $1/7 = 0.14$ generally considered to represent neutral conditions.

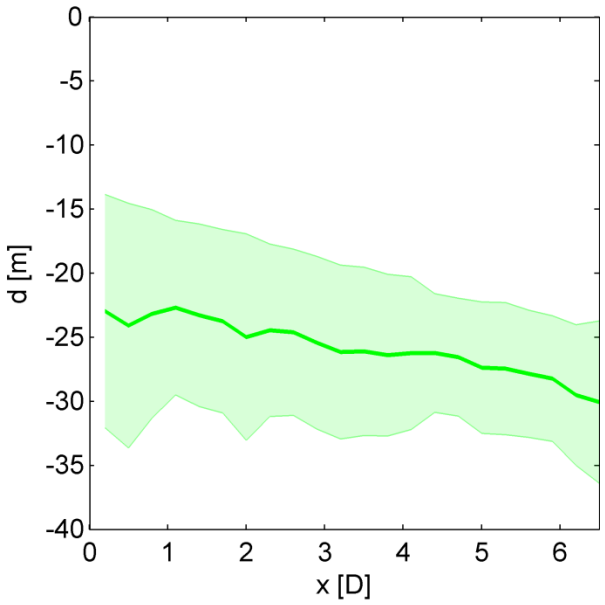

Fig. 4.25. Terrain offset versus downwind distance, as determined by the RHI algorithm. The bold central line indicates median values, while the symmetric shaded error bars represent the standard deviation of the measurements.

The vertical location of the wake center relative to the base of the turbine, as determined by the RHI algorithm, is shown in Fig. 4.26. As expected, the maximum velocity deficit occurred very close to hub height immediately behind the turbine. Similar to the observation in Trujillo et al. (2011), an upward shift in the center of the wake deficit was measured, which can be attributed to a superposition of the effects on the flow by the tilt of the rotor and the grade of the terrain. With the upward rotor tilt being 6 deg and the average downward slope of the ground being less than 1 deg, the result was a net upward shift of the wake centerline.

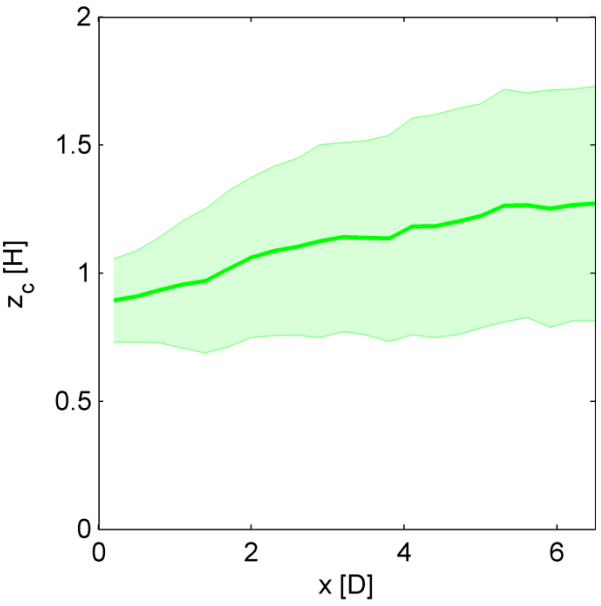

Fig. 4.26. Vertical location of the wake center relative to the base of the turbine (normalized by the hub height H) versus downwind distance, as determined by the RHI algorithm. The bold central line indicates median values, while the symmetric shaded error bars represent the standard deviation of the measurements.

4.5 Summary and conclusions

A set of statistical models has been developed for the characterization of wind turbine wakes from scanning remote sensor measurements, with particular reference here to the TWICS experiment performed at NREL near Boulder, Colorado using the High Resolution Doppler Lidar developed by NOAA. The models are parameterized to discern the dependence of various wake features—such as the velocity deficit, the lateral and vertical dimensions of the wake, and the horizontal and vertical locations of the wake centerline—on variations in atmospheric conditions. TWICS observations, which were classified according to ambient wind speed, turbulence, and atmospheric stability, agree well with those from previous field experiments. Initially about 50–60% immediately behind the turbine, the velocity deficit decreased with downwind distance to a value of 15–25% at $x = 6.5$D. The wake also expanded as it moved downwind of the turbine, albeit less so in the vertical direction because of the presence of the ground: initially the same size as the rotor immediately behind the turbine, the extent of the wake swelled to 2.7D in the horizontal at $x = 6.5$D, but only to 1.2D in the vertical at the same distance. Although the ambient wind speed was not seen to significantly influence the expansion of the wake, the difference in velocity deficit between Regions II and III of the power curve was found to be 10–20% on average, depending on downwind distance.

Improved understanding of wake formation and propagation is essential for optimizing wind turbine layouts, and in turn, power production and profits at wind farms. Although turbines are conventionally spaced at about 6–10D along the prevailing wind direction and 1.5–3D along the crosswind direction (Ammara et al. 2002), computational studies based on large eddy simulation have found that optimal turbine spacing—in terms of power production and overall cost—may be considerably higher, on the order of 15D (Meyers and Meneveau 2012). Still, comparison with data from field tests is necessary to verify the quality of such CFD models, as discussed in Chapter 6.

Whereas the approach developed here can be generally applied to extract wake characteristics from both scanning remote sensor datasets and CFD model output, the specific quantitative results presented in this paper are unique to the turbine, site, and inflow conditions considered herein. To expand upon these results and those of previous studies, additional wake experiments will need to be conducted for a variety of locations and turbine models. In particular, long-range Doppler lidar units would ideally be mounted on the nacelles of utility-scale turbines in future field tests, as in the following chapter. Such an arrangement is advantageous because PPI scans can sample the wake at a zero elevation angle and, moreover, RHI scans would more often transect the wake centerline because the lidar yaws, along with the turbine, according to the ambient wind direction. Preferably, these experiments would be conducted in low-turbulence

environments, where the assumption of ambient flow uniformity would apply and where velocity deficits in the wake would scale with ambient variability farther behind the turbine. In addition, the lidar scan rate should likely be reduced to better resolve the shape of the velocity deficit profile and therefore to determine a clearer distinction between the near and far wake. The procedure would ideally incorporate dual- or triple-Doppler lidar to map the vector, and not LOS, velocities in the flow field (Newsom et al. 2005). Future researchers may also wish to include additional features in the statistical wake models, such as the speed-up around the edge of the wake boundary resulting from flow blockage by the rotor (Bingöl et al. 2010; Rajewski et al. 2013) and/or stability corrections to the logarithmic vertical wind speed profile (Stull 1988). The basic procedure developed here is well-suited to quantify wake characteristics from experiments that incorporate these suggested modifications.

Author contributions

The bulk of this chapter is reproduced from Aitken et al. (2014a). M.L.A. wrote the manuscript, conducted the literature review, developed the wake characterization algorithms, and performed the data analysis. R.M.B., Y.L.P., and J.K.L. designed the experiment, acquired the field data, and revised the manuscript. J.K.L. provided general supervision of the research.

Chapter 5

Utility-Scale Wind Turbine Wake Characterization with Nacelle-based Long-range Scanning Lidar

If I have seen further, it is by standing on the shoulders of giants.

–Isaac Newton

5.1 Introduction

Because of the inherent limitations of conventional anemometry, full-scale measurements of wind turbine wake dynamics are only possible with scanning remote sensors. Previously, ground-based long-range systems with maximum ranges of several kilometers have been used to study the wakes of utility-scale turbines (Käsler et al. 2010; Hirth et al. 2012; Hirth and Schroeder 2013; Iungo et al. 2013; Smalikho et al. 2013; Chapter 4) with hub heights ranging from 80–102 m and rotor diameters from 71–116 m. In addition, Bingöl et al. (2010) and Trujillo et al. (2011) collected wake measurements by mounting a continuous wave ZephIR lidar with a maximum range of 200 m on the nacelle of a stall-regulated 95-kW test turbine with a 29-m hub height and 19-m rotor diameter. Such nacelle-based systems are advantageous over ground-based ones in that scans can more closely transect the wake centerline. Yet, while scaled

models are informative, a comprehensive understanding of wake losses at modern wind farms necessitates observations from pitch-regulated multi-MW turbines. To the best of my knowledge, the work outlined here represents the first analysis in the published literature of a utility-scale wind turbine wake using nacelle-based long-range scanning lidar.

In particular, results are presented for a field experiment conducted in the fall of 2011 at a wind farm in the western United States, in which a Galion G4000 Lidar with a maximum range of 4000 m was used to sample wakes from the nacelle of a utility-scale wind turbine. (Because of confidentiality requirements, certain details about the wind farm and turbine cannot be disclosed.) To quantify wake attributes—such as the velocity deficit (VD), centerline location, and wake width—we apply the procedure described in detail in Section 4.3.4.1. In what follows, Section 5.2 provides an overview of the experimental setup and methodology. Results and a summary are presented in Sections 5.3 and 5.4, respectively.

5.2 Data and methods

5.2.1 Instrumentation

Located in the western United States, the wind farm under consideration comprises turbines with rotor diameter $D \approx 100$ m and hub height $H \approx 80$ m, in addition to cut-in, rated, and cut-out speeds of about 4 m s^{-1}, 13 m s^{-1}, and 25 m s^{-1}, respectively.

With strong winds typically channeled from the south-southwest, the wind farm is arranged in a series of rows spaced 15D along the prevailing wind direction (north-south) and 3D along the transverse direction (east-west), as seen in Fig. 5.1.

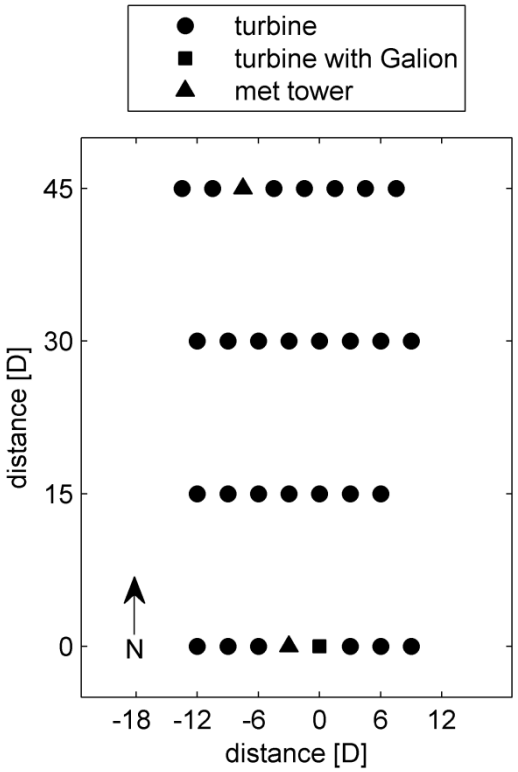

Fig. 5.1. Map of the wind farm, to scale.

During the experiment, wind speed and direction data were collected at hub height with a Risø P2546A cup anemometer and Met One 020C wind vane mounted on a meteorological (met) tower located in the southernmost row of turbines. Wind speed was measured with an accuracy of 1% of reading and wind direction with an accuracy of 3°. As illustrated in Fig. 5.2a, most winds were fairly light during the experiment, with

a median wind speed of about 5 m s^{-1}, just above cut-in. The Weibull fit to the wind speed distribution (Justus et al. 1978) has scale parameter $\lambda = 5.87$ and shape parameter $k = 1.70$. The histogram in Fig. 5.2b shows a bimodal wind direction distribution, the fit to which is a finite von Mises mixture distribution (Masseran et al. 2013) with one mode at 17° and another, more prominent mode at 190°. In Fig. 5.2c, the turbulence intensity (TI) is defined as the ratio of the horizontal wind speed standard deviation to the mean horizontal wind speed, taken over a 10-min interval. The log-normal fit to the TI distribution (Larsen 2001) has location parameter μ = -2.34 and scale parameter $\sigma = 0.51$. The median TI during the experiment was 0.096, similar to values measured in the midwestern United States (Elliott et al. 2009), where much of the nation's wind power capacity is located. Turbulence intensity can be used as a measure of atmospheric stability, with lower (higher) values generally indicating stable (unstable) conditions (Wharton and Lundquist 2012), and the effect of stability on wake characteristics is examined in Section 5.3.

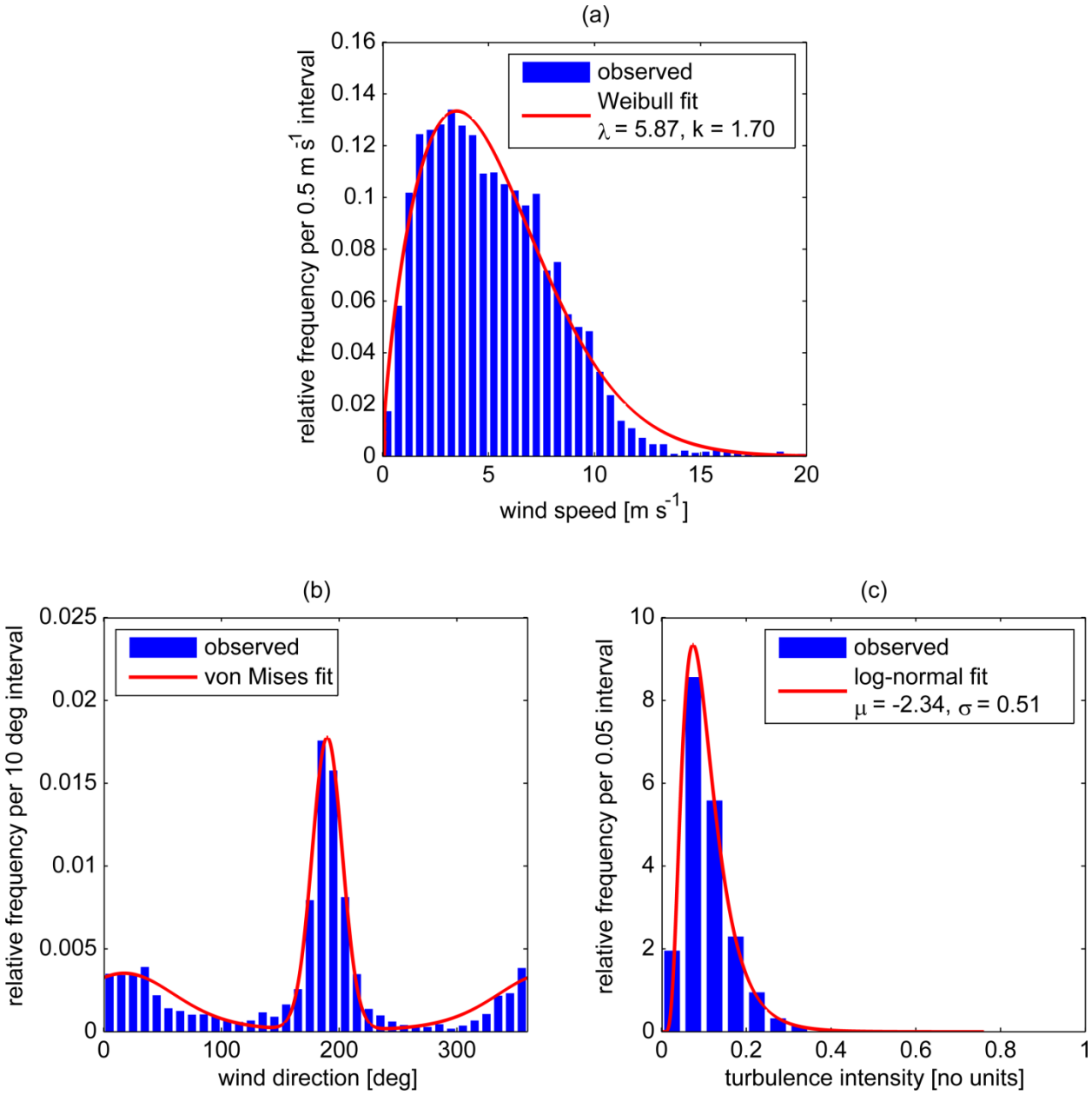

Fig. 5.2. Wind resource characteristics of the site from 14 September 2011 to 12 October 2011, as measured at hub height by the met tower: (a) wind speed, (b) wind direction, and (c) turbulence intensity.

The Galion—a pulsed laser device for wind speed and direction measurement—was placed on the nacelle of one of the turbines adjacent to the met tower in the

southernmost row. Pulsed lidar is advantageous in that multiple measurements can be taken simultaneously along a single line-of-sight. Moreover, pulsed systems are well-suited for long-distance measurements, as the probe length is constant at all range gates. By comparison, continuous wave systems tend to be limited to ranges well below 1 km because the probe length scales as the square of the focus distance (Werner 2005). Lidar data were collected continuously from 14 September 2011 to 12 October 2011, up to a maximum range of 4000 m and with a velocity precision as great as 0.1 m s^{-1}, depending on atmospheric conditions. The signal-to-noise ratio (SNR) of the lidar depends on various environmental factors, such as atmospheric extinction and aerosol concentration, which in turn affects the maximum range and velocity precision (Rye and Hardesty 1993; Chapter 3). Lidar data was recorded when the SNR exceeded a preset threshold of -20 dB. Plan position indicator (PPI) scans—in which the azimuth angle of the beam is swept while holding the elevation angle fixed—were used to sample the flow field in and around the wake, with measurements taken at 67 range gates r separated from one another by 60 m. In each scan, the azimuth was swept through an angle of 84°—symmetric about the longitudinal axis of the turbine—with azimuthal resolution $\Delta\vartheta = 3°$, while holding the elevation angle fixed at 0°. Each scan lasted approximately 4 min, which is long enough for meandering to influence estimation of the wake characteristics, as discussed in Section 5.3.

5.2.2 Wake detection procedure

The procedure used to determine wake parameters from the line-of-sight (LOS) velocity measurements u_{LOS} is based on Section 4.3.4.1. As depicted in Fig. 5.3, the ambient wind is modeled as having uniform speed u and uniform direction. An unprimed coordinate system is centered at the turbine and defined such that the x-axis is aligned with the ambient wind direction. A second, primed coordinate system has the x'-axis (y'-axis) perpendicular (parallel) to the turbine rotor plane and is related to the unprimed system via a rotation matrix

$$\begin{bmatrix} x' \\ y' \end{bmatrix} = \begin{bmatrix} \cos\phi & \sin\phi \\ -\sin\phi & \cos\phi \end{bmatrix} \begin{bmatrix} x \\ y \end{bmatrix} \tag{5.1}$$

to account for the possibility of yaw error. In this formulation, φ is an unknown parameter, whereby $\varphi = 0$ when the rotor plane is perpendicular to the flow and $\varphi \neq 0$ in the case of yaw error. Nominally, the lidar beam should point along the x'-axis when the scanning head is in neutral position, i.e. not rotated. LOS velocity measurements are taken at discrete points in the field, each of which is described by range gate $r = ({x'}^2 + {y'}^2)^{1/2}$ and azimuth angle $\vartheta = \arctan(y'/x')$. For both ϑ and φ, counterclockwise (clockwise) rotations are defined to be positive (negative). Because the angle between the lidar beam and the vector describing the flow field at a given point is $|\vartheta + \varphi|$, the measured LOS velocity is the actual wind speed multiplied by the function $\cos(\vartheta + \varphi)$, which can be rewritten as

$$\begin{aligned}\cos(\theta+\phi) &= \cos\theta\cos\phi - \sin\theta\sin\phi \\ &= \frac{\sqrt{r^2-y'^2}}{r}\cos\phi - \frac{y'}{r}\sin\phi\,.\end{aligned} \tag{5.2}$$

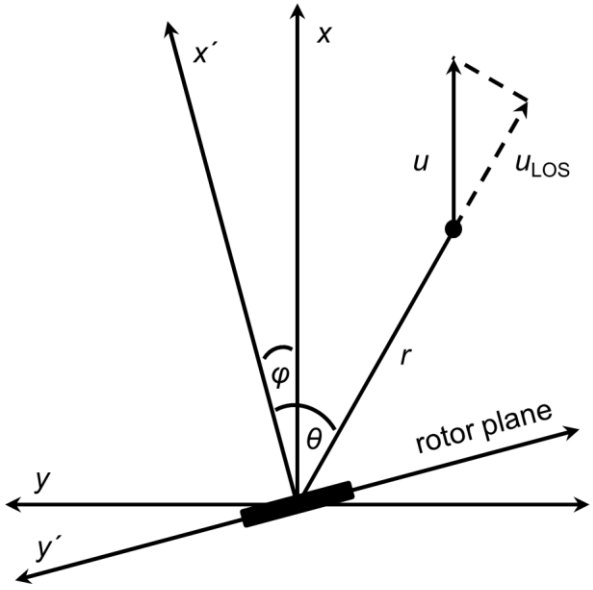

Fig. 5.3. Coordinate systems and variable definitions.

As described in Section 4.2.1, the horizontal cross-section of the velocity deficit profile in the near wake is expected to have a double-Gaussian shape, i.e., the profile contains two local minima corresponding to the points of maximum lift along the blades. On the other hand, in the far wake, turbulent mixing causes the two troughs from the near wake to merge and form a single local minimum, and the profile is Gaussian in shape (Magnusson 1999). The two profiles are sketched in Fig. 5.4. Accordingly, the wake is modeled as either a single- or symmetric double-Gaussian function subtracted from the uniform background flow, in an attempt to account for the

difference between the shape of the VD profile in the near and far wake. For each sweep of the beam, and at each range gate r, three models were fit to the LOS velocity data to identify the wake, if any: a wake-free model

$$u_{\mathrm{LOS}}(y',r) = u\cos(\theta+\phi) = u\left(\frac{\sqrt{r^2-y'^2}}{r}\cos\phi - \frac{y'}{r}\sin\phi\right), \tag{5.3}$$

a single-Gaussian wake model

$$u_{\mathrm{LOS}}(y',r) = \left(u - a\exp\left[\frac{-(y'-y_c)^2}{2s_w^2}\right]\right)\left(\frac{\sqrt{r^2-y'^2}}{r}\cos\phi - \frac{y'}{r}\sin\phi\right), \tag{5.4}$$

and a double-Gaussian wake model

$$\begin{aligned} u_{\mathrm{LOS}}(y',r) = &\left(u - a\left\{\exp\left[\frac{-(y'-y_l)^2}{2s_w^2}\right] + \exp\left[\frac{-(y'-y_r)^2}{2s_w^2}\right]\right\}\right) \\ &\times\left(\frac{\sqrt{r^2-y'^2}}{r}\cos\phi - \frac{y'}{r}\sin\phi\right). \end{aligned} \tag{5.5}$$

In Eqs. (5.3)–(5.5), the variables denote the same physical quantities as in Section 4.3.4.1. For a given range gate r, y' is the only independent variable. All other variables appearing on the right-hand sides of Eqs. (5.3–5.5) are parameters, whose best-fit values are obtained using nonlinear regression. An extra sum-of-squares F-test is used to determine the simplest model (i.e., the model with the least number of parameters) to fit the data, in which the threshold p-value is set to 0.05. That is, if the p-value is less than 0.05, the simpler model is rejected and the more complicated model is deemed to

fit the data significantly better (Kleinbaum et al. 2007). See Section 4.3.4.4 for further details regarding model acceptance criteria.

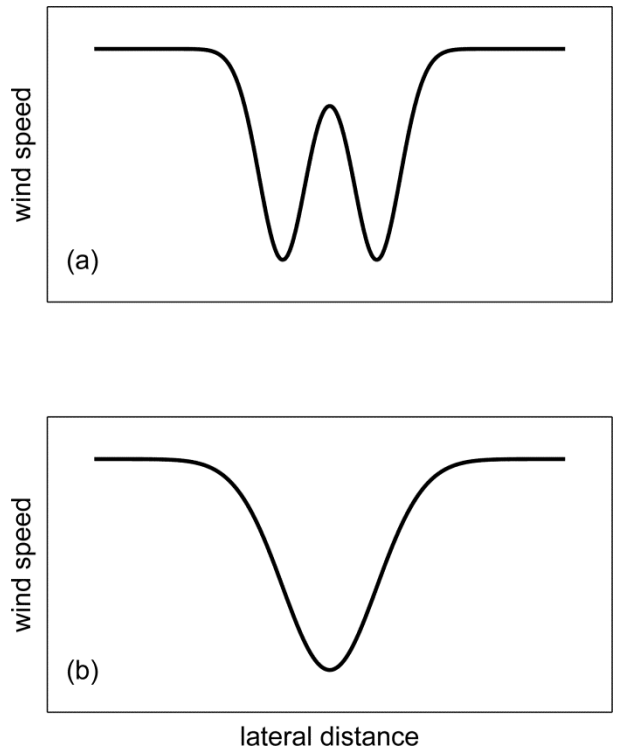

Fig. 5.4. Sketch of the velocity deficit profiles in the (a) near and (b) far wake.

For the single-Gaussian wake, the velocity deficit is given by Eq. (4.10) and the wake width by Eq. (4.11). On the other hand, for the double-Gaussian wake, VD is calculated by taking u_{wake} in Eq. (4.10) to be the minimum modeled wind speed inside the wake, while the wake width is calculated using Eq. (4.12). Using the subscript "0" to denote initial coefficient estimates, seeding for the regression algorithm proceeded for each range gate r as follows: φ_0 was set to zero, u_0 to the median measured LOS velocity for the range gate of interest, a_0 to the difference between u_0 and the minimum

measured LOS velocity, y_{c0} to zero, y_{l0} and y_{r0} to -0.25D and +0.25D (where lift, and therefore the velocity deficit, are expected to be maximum), and s_{w0} to 0.25D (a value corresponding to a wake width of one rotor diameter).

5.3 Results

5.3.1 Wake detection

A total of 11,323 PPI scans were taken over the course of the experiment. Periods for which the turbine was not operating were excluded from the analysis, as determined from the turbine power data. Fig. 5.5 shows, as a function of distance downstream of the turbine x, the percentage of scans for which a wake was determined to be statistically significant in comparison to the background flow. For a wake to be detected, both the entire width of the wake w and an adequate number of points in the ambient flow outside the wake must be sampled. In the case of an 84° sector, the arc length is just 1.8D for the range gate $r = 120$ m $= 1.2$D, and yet the wake width w is expected to be about 1.4D at this distance behind the turbine, based on Eq. (4.2). The relatively low number of detected wakes at the first two range gates suggests that, close to the turbine, the lidar field-of-view (FOV) was not wide enough for both the full width of the wake w and a sufficient portion of the background flow outside the wake to be seen in the scanned velocity profile. However, as the FOV increases, so does the overall number of detected wakes until $x = 3$D, after which wakes are detected with

diminishing frequency because (1) the amplitude of the velocity deficit decreases and therefore scales increasingly with the variability in the ambient flow and (2) velocity measurements become less precise, with lidar SNR falling off as $1/r^2$ (Fujii and Fukuchi 2005). Although a better distinction between the single- and double-Gaussian profiles could likely be made by employing finer azimuthal resolution—$\Delta\vartheta = 3^\circ$ seems to be too coarse—the fraction of double-Gaussian wakes does decrease with downwind distance past $x = 1.8$D, in accordance with expectations.

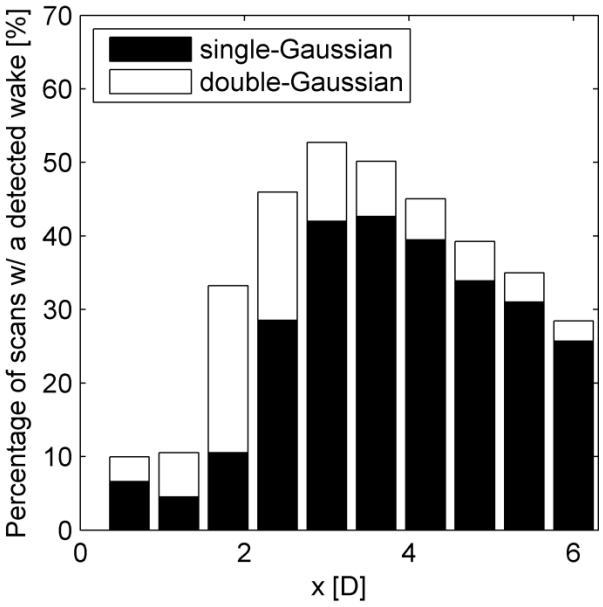

Fig. 5.5. Number of detected wakes versus downwind distance.

Related to the FOV issue in the near wake, the lateral spacing of the turbines influences the maximum distance to which the wake from an individual machine can be reliably discerned. As turbulent mixing causes the wake to expand with downstream

distance, the wakes from lateral-neighbor turbines will eventually merge at some point. Based on the average wake expansion rate from Eq. (4.2) and the lateral spacing of 3D at this particular wind farm, the wake boundaries from lateral-neighbors should intersect at about $x \approx 8\text{D}$. But, similar to the near wake, a sufficient portion of the background flow must also be sampled in the far wake for the wake to be reliably distinguished. Accordingly, wakes were detected on average out to $x = 6\text{D}$ in this particular arrangement. Interestingly, the wake detection rate at intermediate range gates—about 40% on average—agrees quite well with the rejection rate of 60% noted in España et al. (2011), in which instantaneous wakes from porous disks in a wind tunnel were identified using particle image velocimetry.

5.3.2 Velocity deficit

In Fig. 5.6, VD is shown to decrease with x, as faster-moving ambient air is entrained within the wake. From basic one-dimensional momentum theory, the maximum velocity deficit is expected to be 67% at the Betz limit, whereby the turbine operates at peak efficiency (Manwell et al. 2010). On average, then, the initial velocity deficit was quite high, presumably because the average wind speed was just above cut-in, meaning that the turbine was often operating at or near maximum thrust. Notably, a substantial velocity deficit of about 40% was apparent as far as 6D behind the turbine. As in Chapter 4, wind speed had the most pronounced effect on the magnitude

of the velocity deficit, with a consistent difference of about 20%, on average, between Region II (below rated power; $4 < u < 13$ m s^{-1}) and Region III (at rated power; 13 m s^{-1} $< u <$ 25 m s^{-1}) of the power curve. In Fig. 5.6c, low TI corresponds to TI $< 7.5\%$ and high TI corresponds to TI $> 12.5\%$; the categories were chosen to divide the data roughly into thirds and to provide a buffer zone about the median value of 10%. In Fig. 5.6d, "day" ("night") corresponds to 10:00 to 16:00 (21:00 to 6:00) local daylight time, with the intention of capturing periods with unstable (stable) stratification in lieu of detailed temperature profiles that could provide more accurate stability metrics, such as the bulk Richardson number (Friedrich et al. 2012). The average velocity deficit was modestly lower for high TI and daytime conditions, presumably because of more effective mixing between the wake and ambient flow. Let it be noted that there are two competing influences when it comes to turbulence: higher turbulence levels should cause the wind speed inside the wake to recover more quickly, but also preclude the detection of smaller velocity deficits. These two effects seem to more or less cancel out here, and more data will need to be collected in future experiments to reliably discern the influence of turbulence on the wake decay rate.

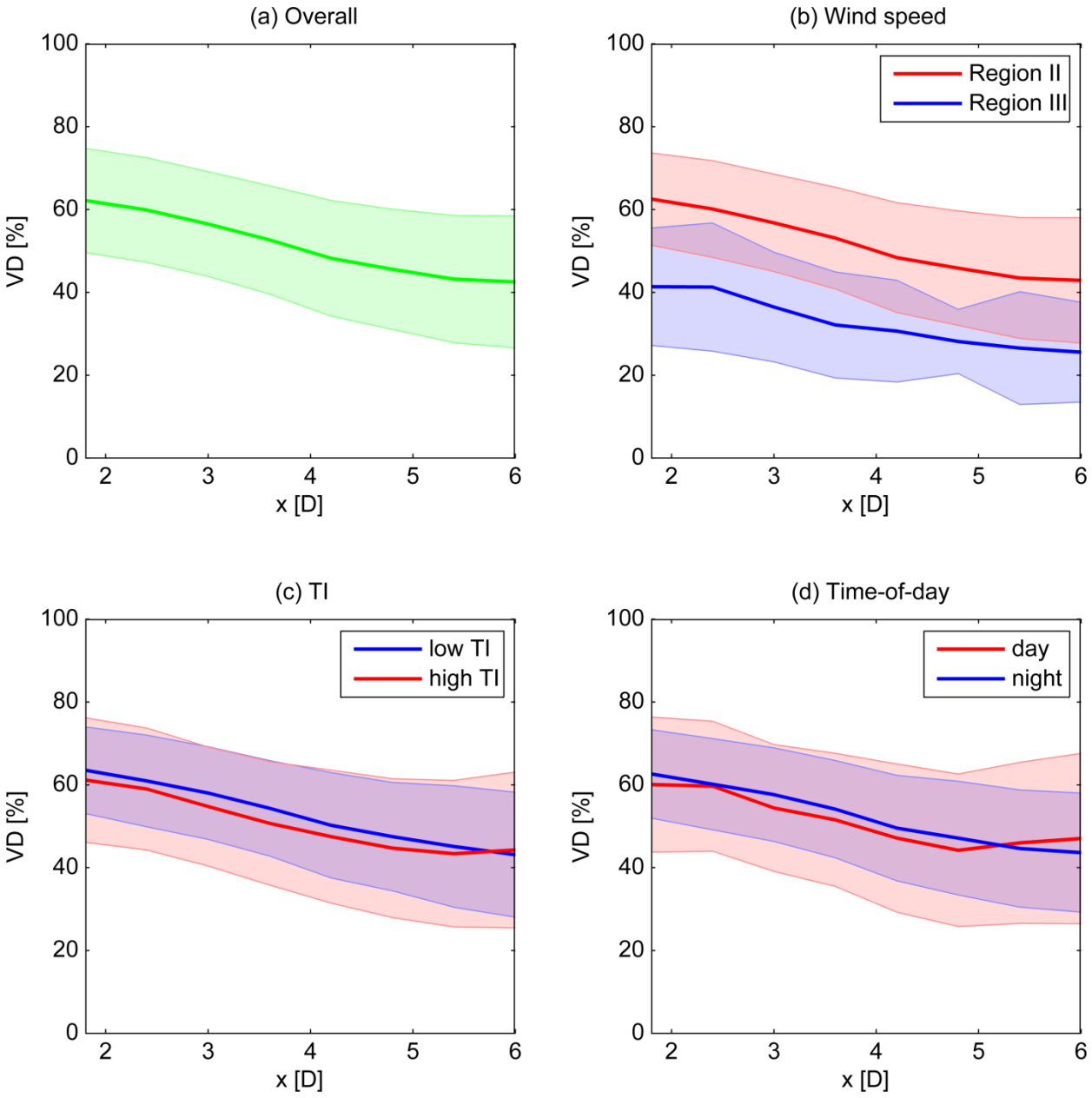

Fig. 5.6. Velocity deficit versus downwind distance. In each subplot, the bold central lines indicate median values, while the symmetric shaded error bars represent the standard deviation of the measurements. Overall results are shown in (a), while velocity deficit measurements are further categorized by (b) ambient wind speed, (c) turbulence intensity, and (d) time-of-day.

5.3.3 Wake meandering and yaw error

In addition to yaw error, the estimate of the parameter φ is influenced by other factors, such as wake meandering and variations in the ambient wind direction. Moreover, misalignment of the lidar beam, which should nominally point perpendicular to the rotor plane when the scanning head is not rotated, also induces systematic error in the estimate of φ. For range gates nearer the turbine, φ should closely approximate the yaw error. As r increases, however, the estimate of φ may gradually diverge somewhat from the actual yaw error because of decreasing correlation between the ambient wind direction at r and that at the turbine. In the case of no yaw error, the effect of meandering is such that the estimate of φ should be zero on average and the variability in φ should be greater when the flow is unstable, i.e., more turbulent, because wake oscillations are random and governed by scales of atmospheric turbulence on the order of the dimension of the wake (España et al. 2011).

As depicted in Fig. 5.7a, the median estimate of φ was found to be slightly negative, presumably because the measured yaw error α—defined here to be the difference between the turbine yaw angle and the hub height wind direction measured by the met tower—had a median value of -0.3° taken over the entire experiment. The median estimate of φ is more negative for low TI and nighttime conditions because the median measured yaw error was -0.5° during these periods, whereas the median α was

almost zero for high TI and daytime conditions. Although there is a small discrepancy between the median values of α and φ at the range gates closest to the turbine—likely explained by the effects of meandering, ambient variability, calibration errors, and lidar misalignment—the wake detection procedure seems capable of quantifying yaw error with reasonable accuracy. Because the standard deviation of α was about 10° during both the day and night, the greater variability in φ for high TI and daytime conditions can be attributed to the larger turbulent structures—and therefore the larger amplitude of wake meandering—experienced during these periods.

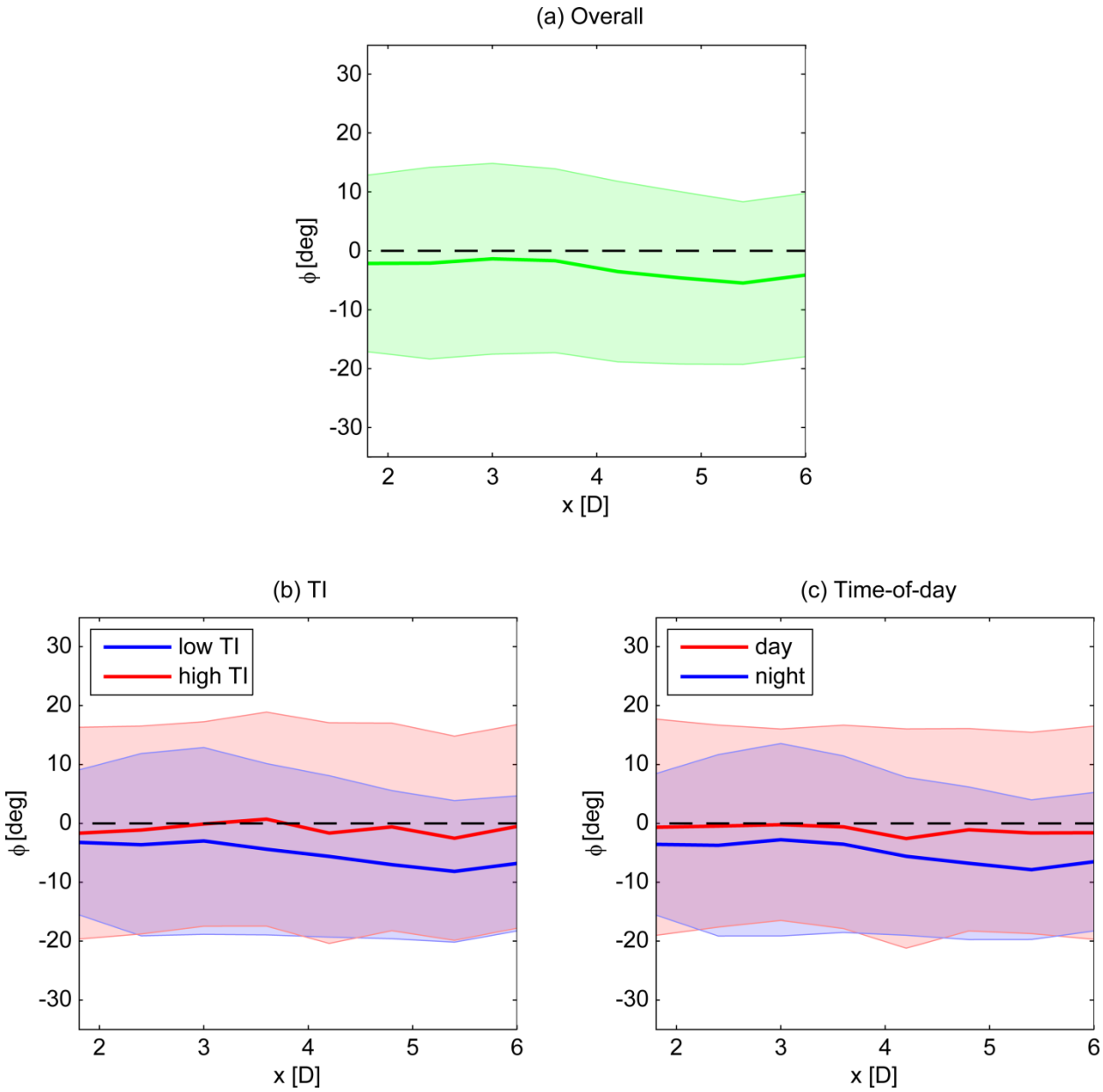

Fig. 5.7. Modeled wind direction relative to the longitudinal axis of the turbine versus downwind distance. In each subplot, the bold central lines indicate median values, while the symmetric shaded error bars represent the standard deviation of the measurements. Overall results are shown in (a), while wind direction measurements are further categorized by (b) turbulence intensity and (c) time-of-day.

Note that the yaw error is a function of wind direction variability, which in turn depends on both wind speed and atmospheric stability, as noted in Mahrt (2011). Wind

direction variability decreases with increasing wind speed because sub-mesoscale motions (on scales of minutes or tens of minutes) significantly enhance wind direction variability for low winds, but cause only small changes of the wind direction for high winds. Moreover, for a given wind speed, wind direction variability is generally larger during the day because of wind direction changes associated with large convective eddies. Mahrt (2011) found greater wind direction variability at night, with the effect of weaker nocturnal winds overwhelming that of daytime convective eddies. Similarly, here the median wind speed measured by the met tower was 7.5 m s^{-1} and 5.4 m s^{-1} during the day and night, respectively. Thus, weaker nocturnal winds are likely responsible for greater wind direction variability, and therefore the larger yaw error observed at night.

The estimate of the horizontal location of the wake centerline y_c is related to the yaw error and the parameter φ. Given the definitions in Section 5.2.2, the force imparted by the turbine on the flow has a component in the $+y$-direction when the yaw error is negative. The median trajectory of the centerline shown in Fig. 5.8a corresponds to a yaw error of about -1°, which agrees fairly well with the median measured value of -0.3°. Similar to φ, the median estimate of y_c trends away from zero for low TI and nighttime conditions because of nonzero yaw error during these periods. Moreover, the variability in y_c is relatively lower for these conditions because the turbulence length scale, and therefore the amplitude of the wake oscillations, is reduced in magnitude.

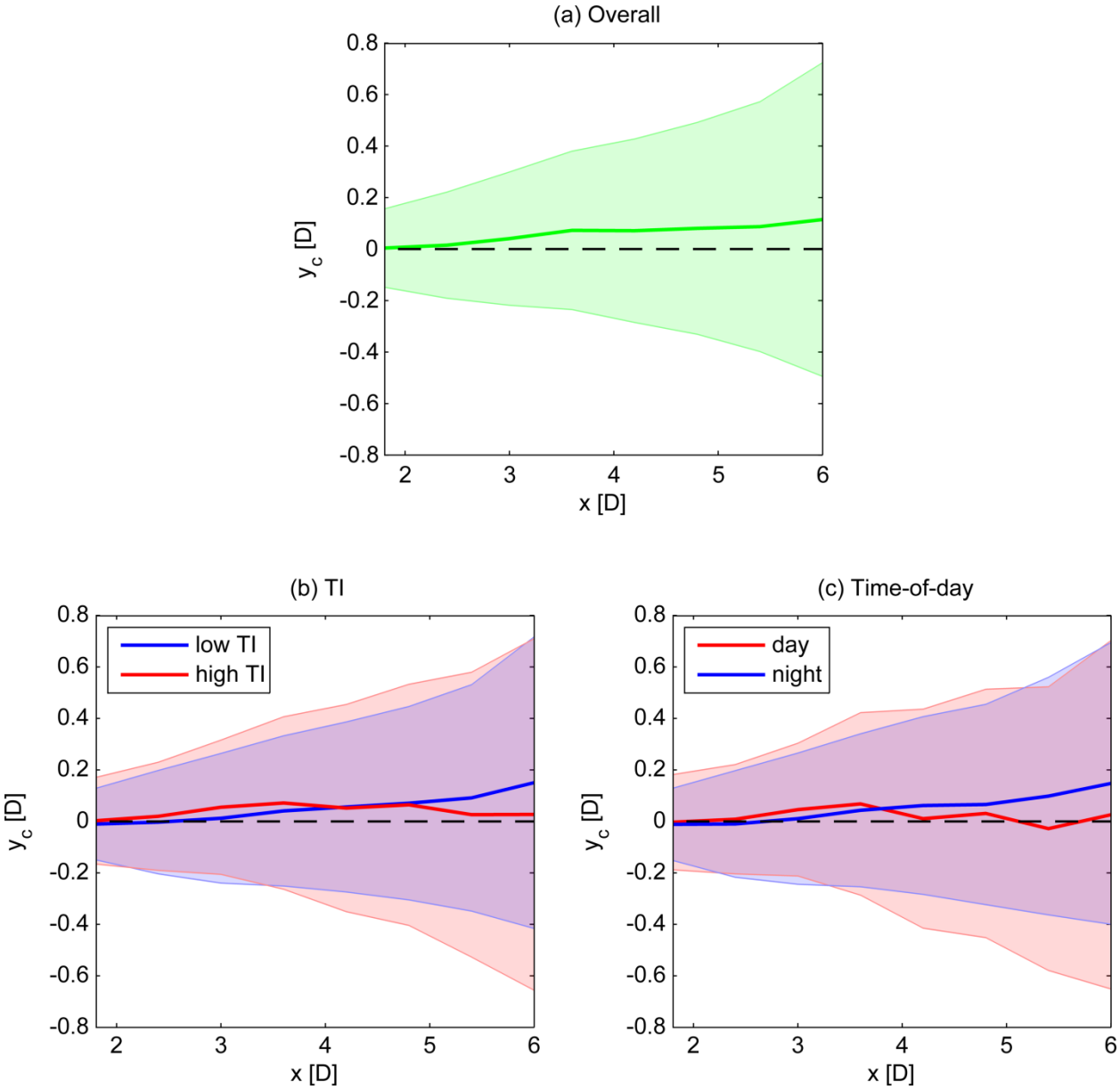

Fig. 5.8. Wake centerline versus downwind distance. In each subplot, the bold central lines indicate median values, while the symmetric shaded error bars represent the standard deviation of the measurements. Overall results are shown in (a), while wake centerline measurements are further categorized by (b) turbulence intensity and (c) time-of-day.

5.3.4 Wake width

Fig. 5.9 illustrates the increase in wake width with downwind distance from 1.5D at $x = 1.8$D to 2.5D at $x = 6$D. Note that, as in Chapter 4, the industry-standard Park model (Barthelmie et al. 2006)—with the typical onshore value for the wake decay constant $k = 0.075$—underestimates the extent of the wake boundary in comparison to the median value. The expansion rate is greater under more turbulent conditions, as represented by TI and time-of-day in Figs. 5.9b and 5.9c, respectively, because of more effective mixing between the wake and ambient flow. The standard deviation of the wake width is a result of: (1) inherent variability, (2) measurement uncertainty, and (3) wake meandering. For more turbulent conditions and regions in the far wake, the wake boundary is more diffuse and its detection is therefore less precise. In addition, because each scan takes several minutes to complete, the wake width estimate is somewhat influenced by the meandering of the wake. Accordingly, the standard deviation of the wake width is greater for high TI and daytime conditions and increases with x.

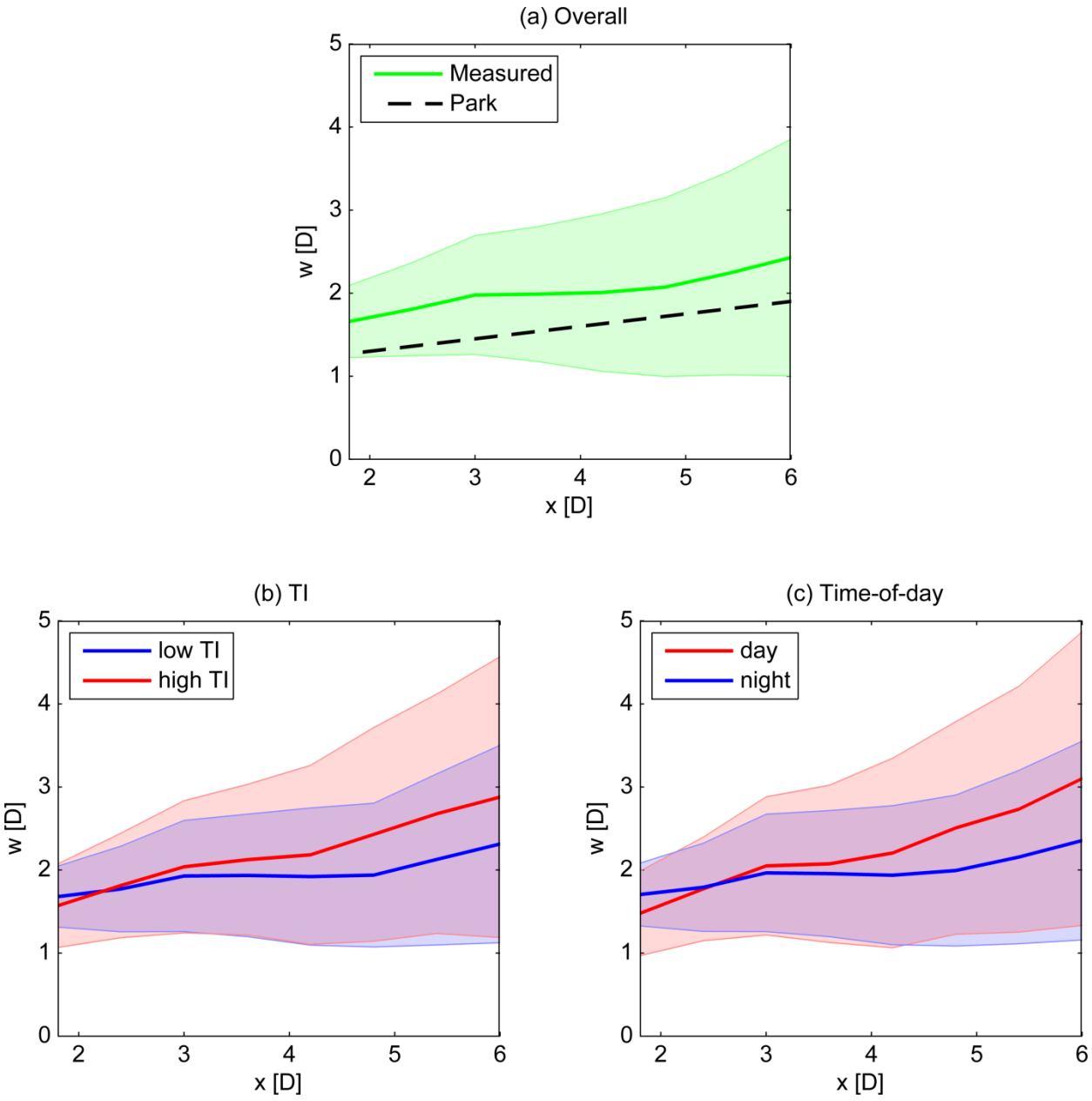

Fig. 5.9. Wake width versus downwind distance. In each subplot, the bold central lines indicate median values, while the symmetric shaded error bars represent the standard deviation of the measurements. Overall results are compared to the Park wake model in (a), while wake width measurements are further categorized by (b) turbulence intensity and (c) time-of-day.

5.4 Summary and conclusions

A nacelle-mounted long-range scanning lidar was used to measure wakes from a utility-scale wind turbine, and wake characteristics from the resulting dataset were quantified with the statistical model developed in Section 4.3.4.1. To the best of my knowledge, this effort represents the first such dataset in the published literature. The wake velocity deficit was observed to depend on ambient wind speed, with the deficit differing by about 20% between Regions II and III of the power curve. The average deficit was large—decreasing from 60% at $x = 1.8$D to 40% at $x = 6$D—as a result of a low average wind speed and therefore high average turbine thrust coefficient. Moreover, the wake width was measured to expand from 1.5D at $x = 1.8$D to 2.5D at $x = 6$D. Both the wake growth rate and the amplitude of wake meandering were observed to be greater for high ambient turbulence intensity and daytime (unstable) conditions. The model is capable of tracking the wake centerline and capturing the yaw error of the turbine with reasonable accuracy.

Up to now, wind farm wake simulations, and hence turbine layout optimization, have suffered from an unacceptable degree of uncertainty, largely because of a lack of adequate experimental data for model verification. To expand upon the results here, additional measurements will need to be taken for a variety of locations and turbine models. Nacelle-based remote sensors are particularly well-suited for such experiments

because scans can more closely transect the wake centerline, as compared to ground-based systems. For future studies involving nacelle-mounted systems, distinct scanning strategies, in which the sensor field-of-view is varied depending on the range of interest, are recommended: the scanned sector should be wider when sampling the near wake, such that the entire extent of the wake can be seen against the background flow, while a relatively narrower sector can be used for scans of the intermediate and far wake. Similarly, the azimuthal resolution ought to be finer for scans of the near wake to facilitate the detection of the velocity deficit profile in that region, while coarser resolution may be more appropriate for scans of the far wake. In addition, faster scan rates would allow for more instantaneous representations of the flow. For studies of the far wake, the turbine of interest should also be relatively isolated, to avoid interference from the wakes of neighboring turbines or other obstacles. Range-height indicator (RHI) scans conducted from the nacelle would provide insight as to the vertical structure of the wake. Methods for quantifying atmospheric stability, such as measurements of both wind speed and temperature at two distinct vertical levels to calculate the Richardson number, would be valuable for categorizing wake characteristics based on stability conditions. The procedure developed in Chapter 4 and applied here should prove useful in the analysis of wind turbine wakes in future field campaigns.

Author contributions

The bulk of this chapter is reproduced from Aitken and Lundquist (2014). M.L.A. wrote the manuscript, conducted the literature review, developed the wake characterization algorithms, and performed the data analysis. J.K.L. revised the manuscript and provided general supervision of the research.

Chapter 6

Large Eddy Simulation of Wind Turbine Wake Dynamics in the Stable Boundary Layer

If it disagrees with experiment, it is wrong.

–Richard Feynman

6.1 Introduction

At utility-scale wind farms, turbine power output and fatigue loading are determined by aerodynamic forces acting on the blades, which vary because of heterogeneity in the ambient flow and because of wakes produced by neighboring turbines. Although often capable of directly resolving large turbulence scales, computational fluid dynamics (CFD) models generally lack many of the important physical processes that influence turbulence dynamics, such as radiation transfer between the surface and the atmosphere, the formation and evolution of clouds, as well as vegetation and soil moisture, which can include snow cover and sea ice. In an effort to predict wind turbine wake behavior in realistic atmospheric boundary layers, a rotating actuator disk model (Mirocha et al. 2014) was recently implemented in the large eddy simulation (LES) package within the Weather Research and Forecasting

(WRF) Model (Skamarock et al. 2008), a numerical weather prediction system with diverse meteorological applications. The actuator disk method incorporates both the conservation of momentum and blade element theory—in which lift and drag are calculated at various sections of the blades—to describe the airflow through the rotor and the resulting wake behind the turbine. By representing the dynamics of the real atmosphere with higher fidelity than current industry standards, the turbine model in WRF-LES, once fully verified, should help to advance the simulations used in wind farm design and operation, leading to more efficient and cost-effective turbine layouts and controls.

The nature of the atmospheric boundary layer varies over a wide range of timescales, including, but not limited to, diurnal, seasonal, and annual cycles. While unstable conditions—typically occurring during the day—are often characterized by convective cells, stable conditions—typically occurring at night—frequently feature strong shear and intermittent turbulence associated with Kelvin-Helmholtz waves (Blumen et al. 2001; Mahrt 2014). Given the strong dependence of wind turbine performance on turbulence and stability (Kelley et al. 2006; Wagner et al. 2009; Barthelmie and Jensen 2010; Wharton and Lundquist 2012; Churchfield et al. 2012; Hansen et al. 2012; Vanderwende and Lundquist 2012; Sathe et al. 2013), comprehensive verification of the actuator disk model in WRF-LES requires simulating an extensive set

of atmospheric conditions. Whereas Mirocha et al. (2014) evaluated simulations of a wind turbine wake against a subset of ground-based lidar measurements taken in convective conditions during the Turbine Wake and Inflow Characterization Study (Smalikho et al. 2013; Chapter 4), the present work compares simulations to nacelle-based lidar wake measurements of a different turbine operating in a stable boundary layer (SBL) during a separate field experiment described in Chapter 5. Moreover, new features—namely, rotor tilt and drag from the nacelle and tower—are added to the existing actuator disk framework.

Of course, the SBL is important to study but also notoriously difficult to simulate (Mahrt 2014). The length scale of turbulent motions is relatively small in stable conditions, such that higher grid resolution is required in comparison to neutral and convective conditions. In LES, the effects of sub-filter scale (SFS) motions on the resolved scales are represented with a turbulence closure scheme, which must be selected carefully to sustain resolved turbulence. Coarse grid resolution and dissipative SFS models can cause boundary layer turbulence to collapse in SBL simulations, resulting in a false laminar flow field and runaway cooling at the surface. Because of the challenges involved, LES of the SBL has been mostly limited to idealized conditions with high geostrophic forcing or weak to moderate stability (Saiki et al. 2000; Kosović and Curry 2000; Basu and Porté-Agel 2006; Mirocha and Kosović 2010; Zhou and Chow 2011; Park

et al. 2014). Here, a preliminary study of a wind turbine operating in an idealized SBL is presented, to lay the groundwork for the addition of more realistic features—such as terrain and inflow conditions from parent mesoscale models—in future work.

In what follows, Section 6.2 provides an overview of both the experimental and computational methodology. Results and conclusions are presented in Sections 6.3 and 6.4, respectively.

6.2 Data and methods

6.2.1 Field experiment

Results from the LES were compared to the observations from Chapter 5, which outlines the experimental details. In addition to the onsite measurements described in Section 5.2.1, atmospheric stability was determined using temperature data at 2 m and at hub height from another offsite met tower located approximately 10 km to the north of the onsite tower. Temperature was measured using Met One 083E-1-35 sensors to an accuracy of 0.1 K.

6.2.2 Case study

The dataset was searched for a time period of sufficient duration and featuring quasi-steady flow conditions—i.e., nearly constant wind speed and direction—to allow representative averages of the wake parameters to be determined. One such interval occurred on 2 October 2011 between 02:30 and 07:30 local daylight time (LDT). Fig. 6.1

shows the wind speed and direction measured at hub height by the onsite tower, as well as the two temperature readings from the offsite tower, from this period. Note that the wind speed fluctuated between 4 and 8 m s^{-1} with an average value of 6.5 m s^{-1}, while the wind direction varied over a range of about 20 degrees. The time-of-day, temperature profile, and surface cooling are consistent with stable atmospheric conditions, and there was no cloud cover or precipitation according to National Weather Service records. Whereas temperature exhibited a decreasing trend with time, the lack of corresponding trends in the wind speed and direction suggests relatively constant large-scale forcing. When a line of best fit is applied to the 2-m temperature measurements (Fig. 6.1c), the slope indicates that the average cooling rate over the 5-hour period was about 0.2 K h^{-1}.

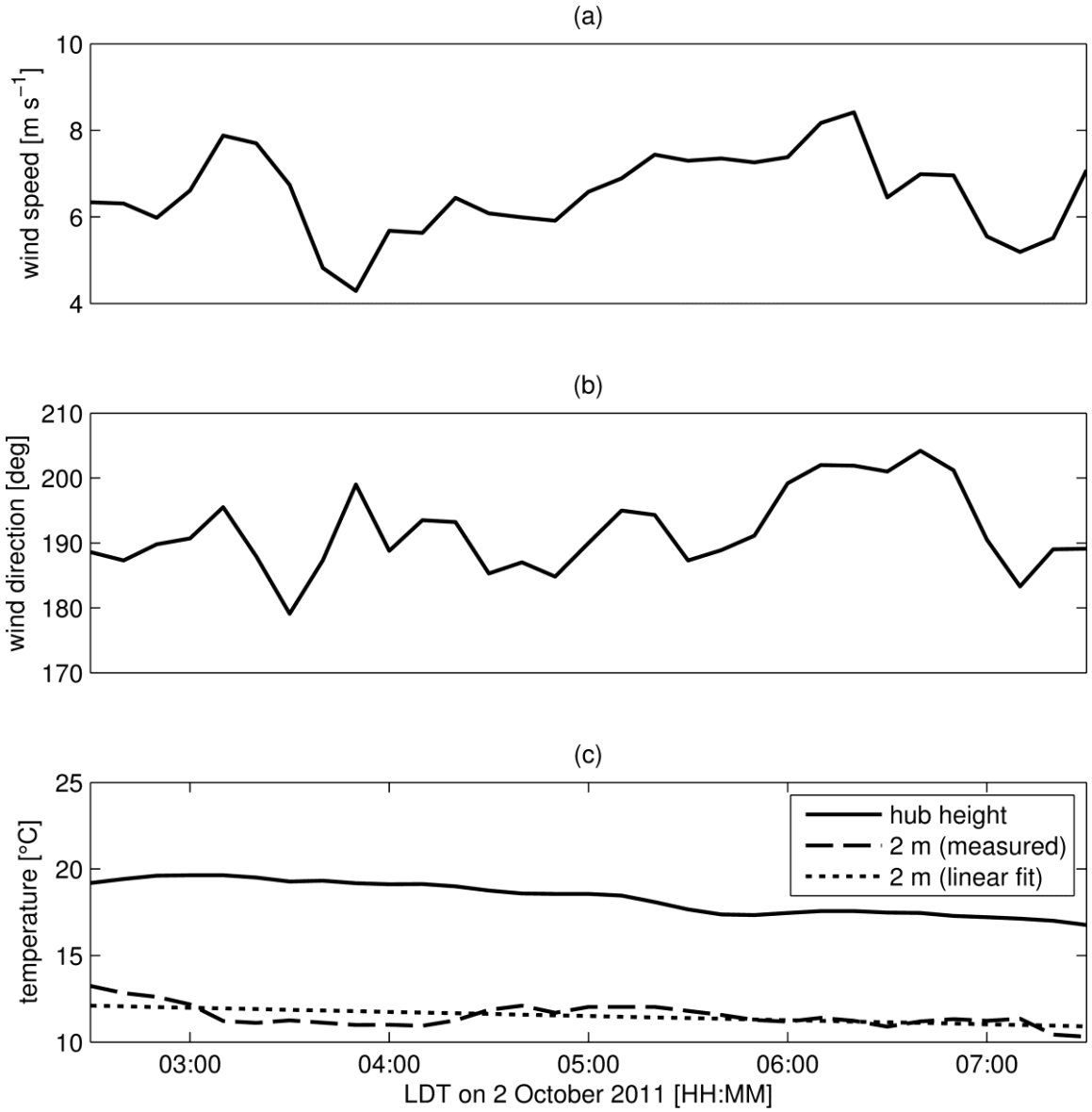

Fig. 6.1. (a) Wind speed and (b) direction measured at hub height by the onsite met tower during the case study period on 2 October 2011. (c) The offsite temperature reading at hub height, as well as the 2-m temperature measurement and corresponding line of best fit.

6.2.3 Simulation setup

Following Mirocha et al. (2014), the simulation was carried out using the

idealized LES framework within WRF, with a fine-scale inner domain (2400 m × 1000

m) nested one-way within a coarser outer domain (3600 m × 1500 m). Lateral grid spacing was set as $dx = dy = 15$ m on the outer domain and $dx = dy = 5$ m on the inner domain. The pressure-based vertical coordinate in WRF allows for an approximate specification of the vertical mesh resolution dz, which was set to 5 m up to a height of 200 m and then stretched by 5% per grid level up to the model top (650 m) for both domains. The actuator disk was placed 7.5D (16.5D) from the inflow (outflow) boundary of the inner domain and centered in the transverse direction. The setup was designed to allow smaller turbulence structures consistent with the finer grid spacing to develop upstream of the turbine. Furthermore, with velocity deficits usually observed to be almost negligible once the wake is 10–12D downwind of the turbine (Vermeer et al. 2003; Smalikho et al. 2013), the entire wake ought to be contained within the inner domain, a fact confirmed upon examination of the WRF-LES output files.

The computational setup was simplified by orienting the predominant inflow direction at hub height to be parallel to the x-axis. A geostrophic wind with $u = 6.80$ m s^{-1} and $v = -3.17$ m s^{-1} was specified to yield an average wind speed at hub height approximately equal to the mean value of 6.5 m s^{-1} measured by the onsite met tower over the case study period. In addition, a uniform initial potential temperature profile was specified, with $\vartheta = 300$ K for $z < 150$ m and $d\vartheta/dz = 0.01$ K m^{-1} for $z > 150$ m, creating a capping inversion to prevent turbulence from reaching the model top.

Random perturbations were imposed at the outset on the mean temperature field up to $z = 150$ m to initiate the turbulent motion.

The simulation was initialized dry with zero latent flux. No cloud, radiation, or land surface models were used, and surface boundary conditions were specified using Monin-Obukhov similarity theory. Basu et al. (2008) demonstrated that the surface cooling rate—as opposed to the surface heat flux—should be prescribed as the lower boundary condition when simulating the SBL under moderate to strong stratification. Accordingly, the surface cooling rate was set uniformly in both space and time to the measured value of 0.2 K h^{-1} to simulate the stable conditions. A Rayleigh damping layer with a coefficient of 0.003 s^{-1} was applied to the upper 150 m of each domain to avoid spurious wave reflection from the model top. Because the excessive mean dissipation of the Smagorinsky model limits its applicability in SBL simulations (Kosović and Curry 2000; Zhou and Chow 2011), the nonlinear backscatter and anisotropy (NBA) model (Kosović 1997; Mirocha et al. 2010) was chosen as the sub-grid scale closure scheme.

Periodic lateral boundary conditions were specified for the outer domain, which was run for 9 hours to spin-up turbulence consistent with the geostrophic wind and surface forcing. After starting the inner domain with the actuator disk at the beginning of hour 9, the simulation continued to run for another 5.5 hours, with the first half hour of the inner domain solution discarded due to spin-up of turbulence. Instantaneous

velocity fields were saved at an interval of 8 s, corresponding to the discretization of the measured lidar data.

6.2.4 Modifications to the actuator disk model in WRF-LES

Lookup tables for the blade characteristics and control schedule were changed in the actuator disk module to correspond to the turbine in Chapter 5. In addition, the effects on the flow by the nacelle and tower were added to the existing wind turbine formulation. Namely, the nacelle is represented as a permeable disk normal to the inflow with radius R_{nac} and area $A_{\text{nac}} = \pi {R_{\text{nac}}}^2$. The drag force exerted by the nacelle on the flow is given by

$$F_{\text{nac}} = \frac{1}{2} C_{D,\text{nac}} \rho A_{\text{nac}} V_{nac}^2 \,, \tag{6.1}$$

where $C_{D,\text{nac}}$ is the drag coefficient of the nacelle, ρ is air density, and V_{nac} is the component of the incident wind velocity normal to the face of the nacelle. Following El Kasmi and Masson (2008), $C_{D,\text{nac}}$ is set to 1. A similar approach is taken to model the effect of the tower, which has a cylindrical shape with radius R_{tower} and area $A_{\text{tower}} = 2R_{\text{tower}}H$ normal to the flow. The drag coefficient of the tower $C_{D,\text{tower}}$ is set to 1.2, after Wu and Porté-Agel (2011).

Additionally, the effect of rotor tilt was also added to the model, following the approach in Mikkelsen (2003). In blade element momentum (BEM) theory, the freestream wind speed V_0 used to calculate the lift and drag forces along the blades is

taken to be the component of the flow normal to the rotor plane of rotation. Following the coordinate system convention in Mirocha et al. (2014)—cf. Fig. 6.2—the vector normal to the rotor plane amounts to a rotation of the unit vector $\hat{\boldsymbol{x}}'' = [1\ 0\ 0]^{\mathrm{T}}$ by the yaw angle Φ about the z''-axis:

$$\hat{\boldsymbol{x}}' = \begin{bmatrix} \cos\Phi & -\sin\Phi & 0 \\ \sin\Phi & \cos\Phi & 0 \\ 0 & 0 & 1 \end{bmatrix} \begin{bmatrix} 1 \\ 0 \\ 0 \end{bmatrix} = \begin{bmatrix} \cos\Phi \\ \sin\Phi \\ 0 \end{bmatrix}. \tag{6.2}$$

If the rotor plane is also tilted—taken to be a rotation by the angle δ about the y'-axis—then the normal vector to the rotor plane becomes

$$\hat{\boldsymbol{x}} = \begin{bmatrix} \cos\delta & 0 & \sin\delta \\ 0 & 1 & 0 \\ -\sin\delta & 0 & \cos\delta \end{bmatrix} \begin{bmatrix} \cos\Phi \\ \sin\Phi \\ 0 \end{bmatrix} = \begin{bmatrix} \cos\Phi\cos\delta \\ \sin\Phi \\ -\cos\Phi\sin\delta \end{bmatrix}. \tag{6.3}$$

With the wind vector at the actuator disk denoted $V = [u\ v\ w]^{\mathrm{T}}$, the freestream wind speed to be used in BEM theory is given by

$$V_0 = \boldsymbol{V} \cdot \hat{\boldsymbol{x}} = u\cos\Phi\cos\delta + v\sin\Phi - w\cos\Phi\sin\delta\,. \tag{6.4}$$

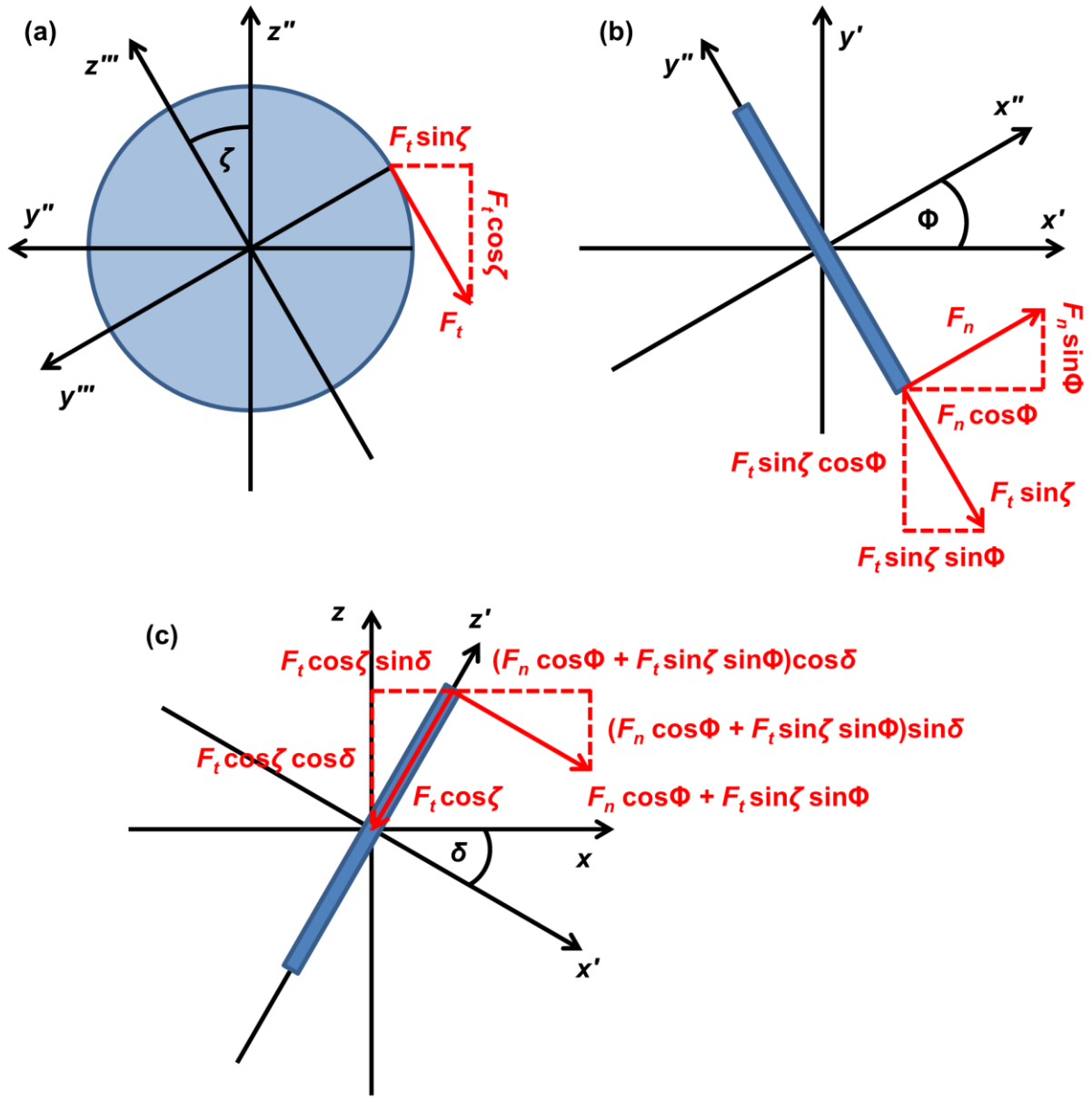

Fig. 6.2. Diagram of the coordinate system convention and components of the force acting on the actuator disk. Axes and angles are shown in black, forces in red, and the disk in blue. (a) The view upwind of the rotor along the longitudinal axis, (b) a bird's-eye view looking down at the rotor along the vertical axis, and (c) a side view of the rotor along the transverse axis.

In the case of no rotor tilt, the components of the force F exerted on the actuator disk by the flow were found in Equations (A20–A22) of Mirocha et al. (2014) by applying successive rotations, one by the angle -ζ about the x'''-axis and another by the angle Φ about the z''-axis:

$$\boldsymbol{F} = \begin{bmatrix} \cos\Phi & -\sin\Phi & 0 \\ \sin\Phi & \cos\Phi & 0 \\ 0 & 0 & 1 \end{bmatrix} \begin{bmatrix} 1 & 0 & 0 \\ 0 & \cos\zeta & \sin\zeta \\ 0 & -\sin\zeta & \cos\zeta \end{bmatrix} \begin{bmatrix} F_n \\ 0 \\ -F_t \end{bmatrix} = \begin{bmatrix} F_n\cos\Phi + F_t\sin\zeta\sin\Phi \\ F_n\sin\Phi - F_t\sin\zeta\cos\Phi \\ -F_t\cos\zeta \end{bmatrix}, \quad (6.5)$$

where F_n and F_t are the normal and tangential forces, respectively, acting at a point on the disk. In the case of nonzero rotor tilt, on the other hand, a third rotation by the angle δ about the y'-axis must be applied to the vector in Eq. (6.5):

$$\begin{aligned} \boldsymbol{F} &= \begin{bmatrix} \cos\delta & 0 & \sin\delta \\ 0 & 1 & 0 \\ -\sin\delta & 0 & \cos\delta \end{bmatrix} \begin{bmatrix} F_n\cos\Phi + F_t\sin\zeta\sin\Phi \\ F_n\sin\Phi - F_t\sin\zeta\cos\Phi \\ -F_t\cos\zeta \end{bmatrix} \\ &= \begin{bmatrix} F_n\cos\Phi\cos\delta + F_t\sin\zeta\sin\Phi\cos\delta - \mathrm{F_t}\cos\zeta\sin\delta \\ F_n\sin\Phi - F_t\sin\zeta\cos\Phi \\ -F_n\cos\Phi\sin\delta - F_t\sin\zeta\sin\Phi\sin\delta - \mathrm{F_t}\cos\zeta\cos\delta \end{bmatrix}. \end{aligned} \quad (6.6)$$

Simulations were performed after incorporating the above modifications and results are presented below.

6.3 Results

Prior to verifying the simulated wake characteristics, the WRF-LES inflow must first be compared to the observations. Statistics for the simulated inflow were gathered by sampling the hub height wind speed and direction over the course of the 5-hour run

at a point located 2.5D upwind of the turbine, which corresponds to the recommended distance for measuring freestream winds in the determination of wind turbine power performance (International Electrotechnical Commission 2005). As seen in the histograms in Fig. 6.3, the wind speed varies over a range of 4 to 8 m s^{-1} with an average of 6.4 m s^{-1}, and almost all of the wind direction values are contained within a 20° range about the predominant value of 270°, very closely matching the measured inflow conditions in both cases. Note that, as mentioned previously, the computational setup was simplified by orienting the predominant inflow direction at hub height to be parallel to the x-axis, such that individual simulated wind direction values are not meant to match their measured counterparts. The relative wind direction *ranges*, however, are in very good agreement, as intended.

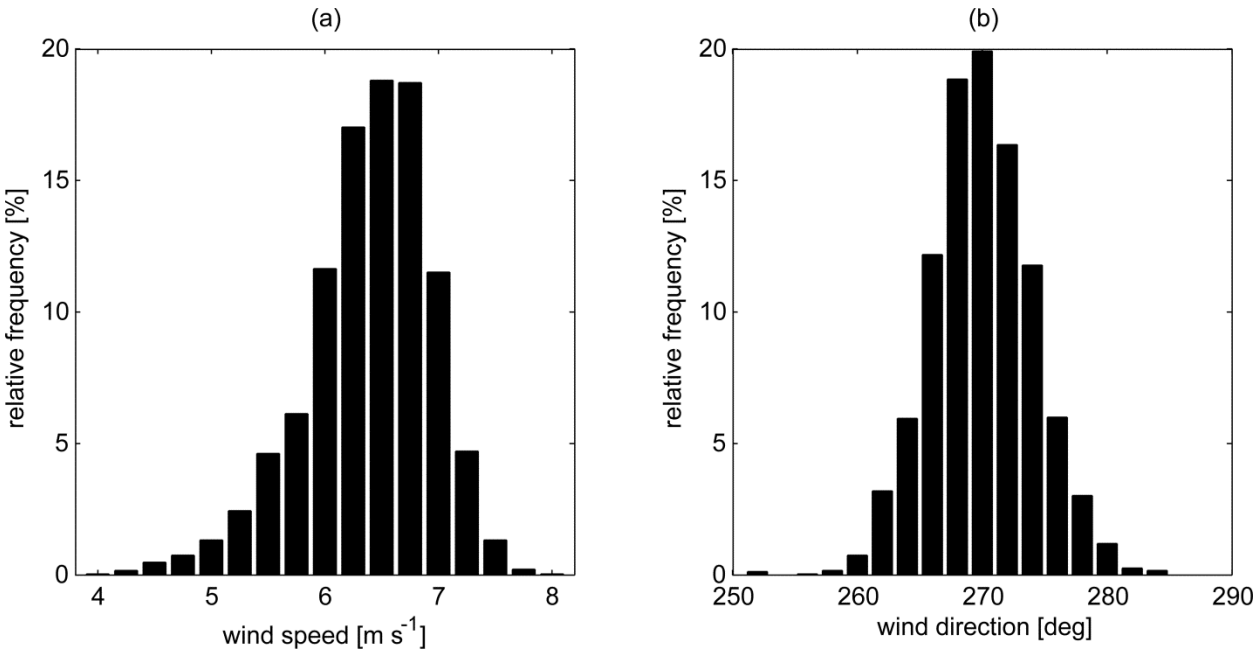

Fig. 6.3. Histograms of the simulated hub height (a) wind speed and (b) direction at a point located 2.5D upwind of the turbine.

The instantaneous contours of wind speed in Fig. 6.4 indicate the turbulent nature of the both the background flow field and the wake itself. Close to the turbine, the wake is relatively coherent and the wind speeds inside the wake are noticeably smaller than in the surrounding flow. Farther downwind, on the other hand, the wake is more diffuse and the wind speeds inside the wake are comparable to that of lulls in the ambient flow. Moreover, meandering behavior is apparent in the far wake region of Fig. 6.4a as ambient turbulence causes the wake to move randomly about the prevailing wind direction.

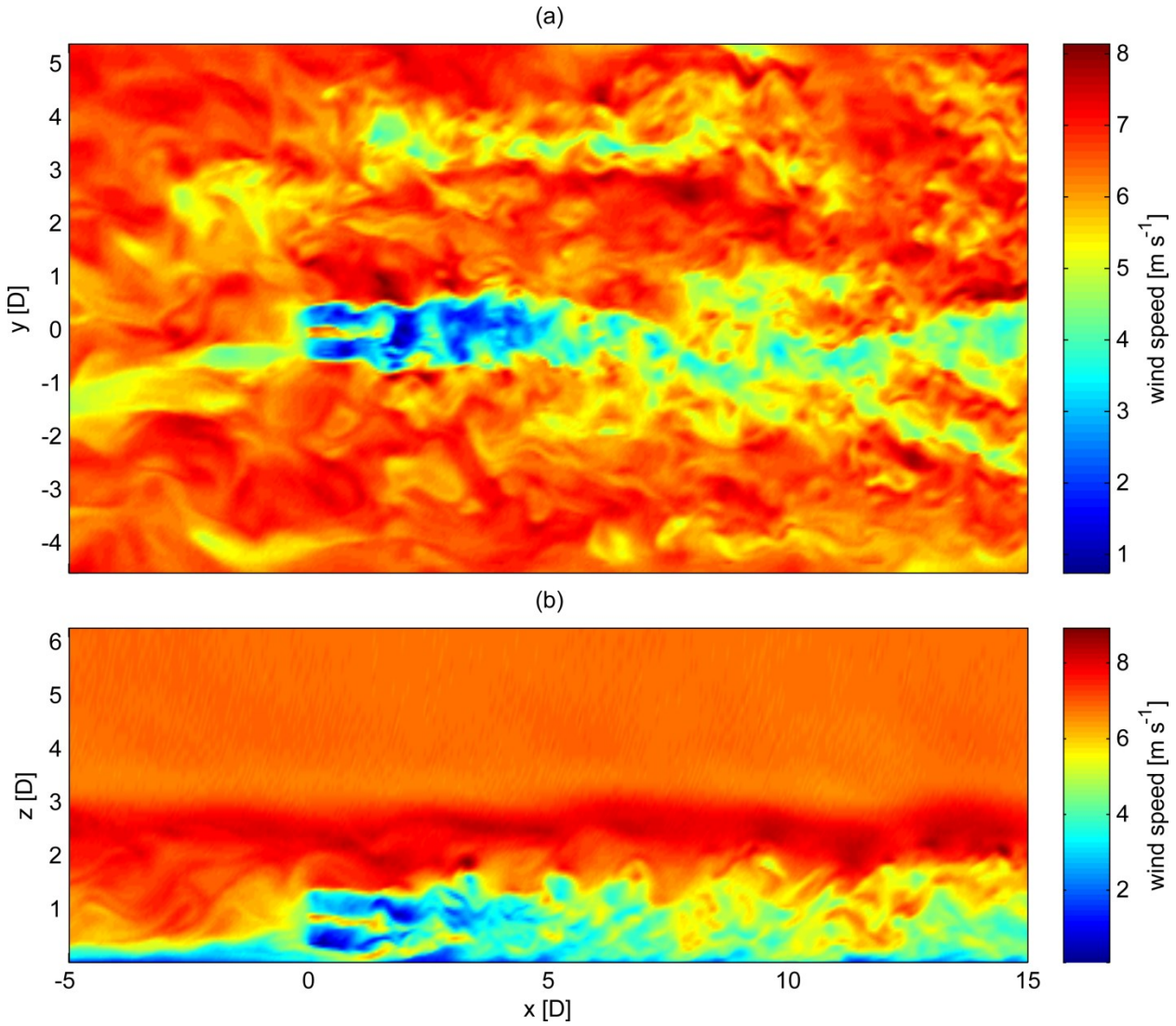

Fig. 6.4. Instantaneous contours of wind speed in the (a) x-y plane and (b) x-z plane at the center of the disk at hour 12 in the simulation. The turbine is located at $x = y = 0$.

To enable the comparison between computational and experimental results, the procedure outlined in Section 5.2.2 for quantifying wake characteristics was adopted, in which unknown parameters in a nonlinear statistical model are estimated using successive wind speed profiles. The procedure is justified when the residuals are independent, which is certainly true in the real world where various forcings—such as

terrain features and obstacles, as well as heterogeneous land cover and surface conditions—serve to break up correlations in the turbulence structure. In the case of the measured data, a model fit is made to each lidar scan, which can be thought of as a quasi-instantaneous representation of the flow. On the other hand, the idealized setup in the simulations includes flat terrain along with uniform forcing at the surface and in the geostrophic wind, leading the turbulence structure to contain more robust correlations than would otherwise occur in nature. As a result, the wake detection algorithm cannot be applied to the instantaneous WRF-LES output in this case, or else the estimated wake parameters would be biased, and—more concerning—the model could potentially mistake a lull in the ambient flow for a wake. To avoid these issues, the WRF-LES output is first averaged in time before performing the model fit. The wake detection procedure will be applied to instantaneous WRF-LES output in future simulations that incorporate terrain and more realistic boundary conditions, facilitating the comparison between measured and simulated results.

With these caveats in mind, a comparison of the velocity deficit (VD) as a function of downwind distance x is shown in Fig. 6.5a. The blue central line depicts the median measured value, and the shaded region indicates one standard deviation on either side. The red line, on the other hand, indicates VD values computed from the mean LES field. Moreover, a comparison of the wake width w vs. x is shown in Fig.

6.5b, which shares the same color scheme as Fig. 6.5a. In the case of the velocity deficit, the simulation results are within the uncertainty in the experiment. The simulated wake width is also in good agreement with the measurements, aside from the two range gates at $x = 2.4$D and $x = 3$D. Compared to the wake width measurements taken over the entire field campaign (see Section 5.3.4), the average wake width estimates at these two range gates were unusually high for the 5-hour period considered here, which could be related to the small sample size of the case study. Given the constraints in both the experiment and the simulation—including 4-min lidar scans, a limited sample size, and an idealized simulation setup—the actuator disk model in WRF-LES adequately reproduces the measured wake characteristics. Even closer agreement is expected to be seen in future work by making use of higher resolution lidar data and more realistic simulations.

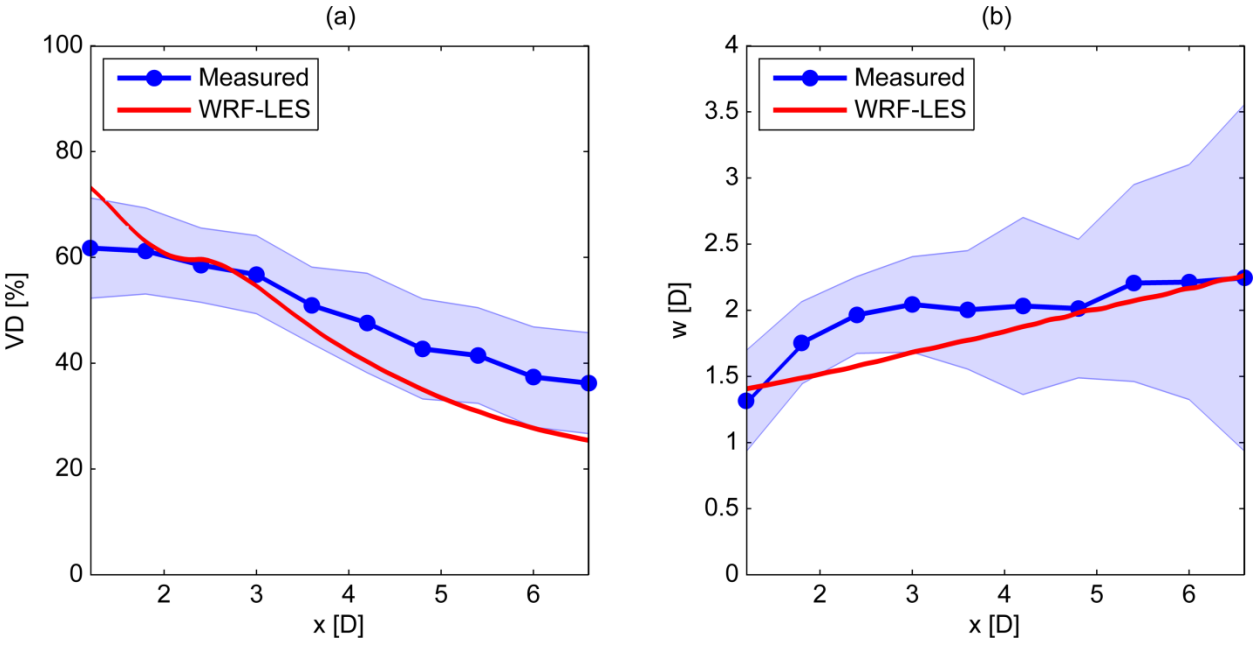

Fig. 6.5. (a) Velocity deficit and (b) wake width versus downwind distance. In each subplot, the blue central lines indicate median measured values, whereas the symmetric shaded error bars represent the standard deviation of the measurements. Simulation results are plotted in red.

In the near wake—within a few rotor diameters downstream of the turbine—the velocity deficit profile is expected to have a double-Gaussian shape, i.e., the profile contains two local minima corresponding to the points of maximum lift along the blades. On the other hand, in the far wake, turbulent mixing causes the two troughs from the near wake to merge and form a single local minimum, and the profile is Gaussian in shape (Magnusson 1999; Chapters 4 and 5). Fig. 6.6 shows, as a function of x, the percentage of scans for which a wake was determined from the measured data to be statistically significant in comparison to the background flow. The total number of detected wakes increases from $x = 1.8$D to $x = 3$D as the lidar field-of-view increases,

allowing a wider portion of the flow to be captured in the scan. However, wakes are detected with diminishing frequency after $x = 3$D because (1) the amplitude of the velocity deficit decreases and therefore scales increasingly with the variability in the ambient flow and (2) velocity measurements become less precise, with lidar SNR falling off as $1/r^2$ (Fujii and Fukuchi 2005). As expected, a large fraction of the wakes were seen to have a double-Gaussian velocity deficit profile close to the turbine, and hardly any double-Gaussian wakes were detected after $x = 3$D, which may be considered the division between the near and far wake. Interestingly, $x = 3$D is the same distance at which the average simulated flow field transitions from a double-Gaussian to a single-Gaussian velocity deficit profile, indicating that the actuator disk model in WRF-LES is also capable of representing a realistic progression from the near wake to the far wake.

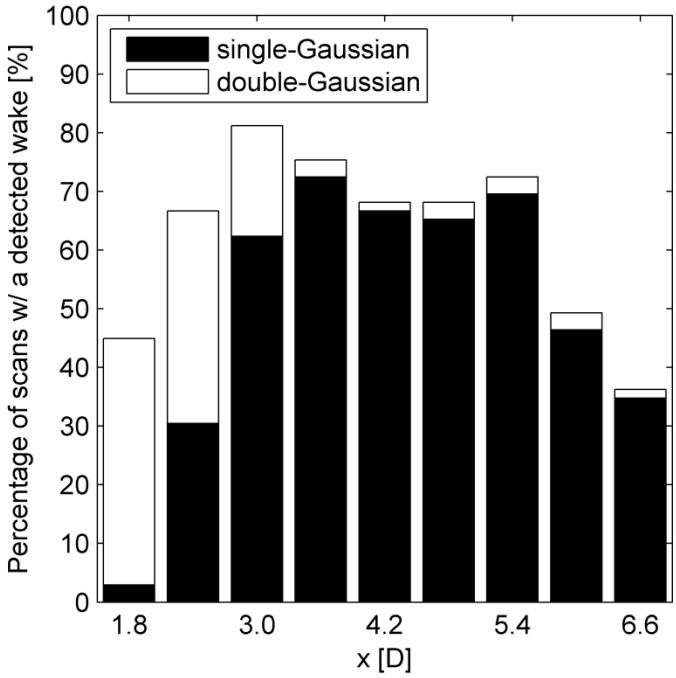

Fig. 6.6. Percentage of wakes detected from the measured data versus downwind distance.

One of the new contributions to the turbine model in WRF-LES is the inclusion of rotor tilt, which affects the vertical location of the wake centerline z_c, defined to be the height at which the velocity deficit inside the wake is maximum. The evolution of this parameter, which was determined using the vertical scan (or RHI) algorithm from Section 4.3.4.3, appears in Fig. 6.7 as simulated both with and without rotor tilt. With the rotor thought of as an actuator disk, the net force on the flow by the turbine has a small component in the $+z$-direction when the rotor is tilted away from vertical (see Fig. 6.2c, noting that the force on the flow is equal to and opposite that on the disk), resulting in an upward shift of the wake center comparable to the horizontal displacement of the wake in the case of yawed flow. This upward shift is qualitatively similar to that measured in Fig. 4.26.

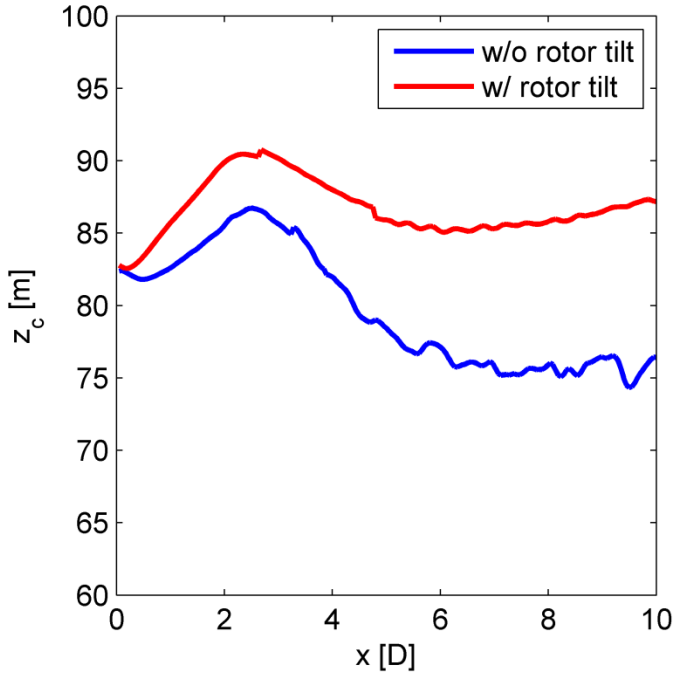

Fig. 6.7. Vertical location of the wake centerline versus downwind distance for simulations with and without rotor tilt.

6.4 Conclusion

To expand upon the convective case study in Mirocha et al. (2014), numerical simulations of a wind turbine wake using the actuator disk model in WRF-LES were compared to nacelle-based scanning lidar measurements taken in stable atmospheric conditions. Moreover, new features—namely rotor tilt and drag from the nacelle and tower—were added to the existing actuator disk framework. Using the velocity deficit and wake width as metrics for model verification, the simulations show good agreement with the observations. Notable results include a high average velocity deficit, decreasing

from 73% at $x = 1.2$D to 25% at $x = 6.6$D, resulting from a low average wind speed and therefore high average turbine thrust coefficient, in addition to the low background turbulence characteristic of stable conditions. Moreover, the wake width was seen to expand from 1.4D at $x = 1.2$D to 2.3D at $x = 6.6$D. Compared to the rotor, the effect of the tower and nacelle on the flow is relatively small but nevertheless important for an accurate representation of the entire wake. The inclusion of rotor tilt in the model causes the vertical location of the wake center to shift upward, which has important implications for the design of turbine layouts and controls at wind farms. It would be interesting to study in future experiments and simulations how this upward shift is influenced by atmospheric stability.

Further verification of the actuator disk model in WRF-LES will require that simulations of various types of turbines and atmospheric conditions be evaluated against corresponding experimental data. In addition to comparison with wake observations aloft, LES results should also be compared to the measured effects of turbines on wind speed, turbulence, and temperature at the surface (Rajewski et al. 2013). An extension of the stable boundary layer case presented here would be to simulate a turbine operating in a low-level jet (Blackadar 1957; Bonner 1968; Banta et al. 2002; Lundquist and Mirocha 2008). Moreover, future simulations ought to incorporate both terrain features and more realistic inflow from mesoscale models to better represent turbulence.

Several turbulence closure schemes—such as the dynamic reconstruction model (Chow et al. 2005) and the locally averaged scale-dependent dynamic model (Basu and Porté-Agel 2006)—should be tested under various atmospheric conditions to determine the most appropriate model for each scenario. Using the actuator disk model developed in Mirocha et al. (2014) and expanded upon here, more detailed features may be added, such as the blade coning angle (Mikkelsen 2003). Once computing resources allow WRF-LES to be run at sufficiently high resolution, actuator line techniques (Mikkelsen 2003; Churchfield et al. 2012) may eventually be implemented to complement the existing actuator disk model in cases requiring higher fidelity representations of turbine physics.

Still, there are many practical applications for the current framework in the meantime. For example, modeling an array of turbines within a single domain could be used to verify the mesoscale wind farm parameterization in WRF (Fitch et al. 2012) under changing stability conditions (Fitch et al. 2013). Furthermore, the actuator disk model could be used to study optimal turbine configurations within wind farms, as in Meyers and Meneveau (2012) and Archer et al. (2013), helping to minimize wake effects and thus the cost of energy.

Author contributions

The bulk of this chapter is reproduced from Aitken et al. (2014b). M.L.A. wrote the manuscript, conducted the literature review, added new features to the actuator disk model in WRF-LES, ran the simulation, and performed the data analysis. All authors helped to design the simulation, debug errors, and interpret the results. B.K., J.D.M., and J.K.L. revised the manuscript, and J.K.L. provided general supervision of the research.

Chapter 7

Conclusion

There are those who look at things the way they are and ask, "Why?" I dream of things that never were and ask, "Why not?"

–Robert Kennedy

Climate change is one of the foremost challenges of our time, and common sense demands action. Just as insurance is used to hedge against the risk of contingent and uncertain losses, developing new technologies and improving existing ones to mitigate the potential adverse effects of climate change would appear to be the prudent choice. At its core, climate change mitigation is fundamentally about economics: currently, clean energy technologies are simply too expensive in comparison to fossil fuels. To be viable, renewables must be made more valuable than conventional energy sources via economies of scale, research and development, expanded transmission, and energy storage. Because the free market tends to be unable to solve large-scale environmental problems, sound policy support is of paramount importance.

Out of the many technological options for mitigating climate change, wind—as the most mature and cost-effective source of renewable energy—appears poised to be the primary challenger to fossil fuels, at least in the near term. Although revolutionary

discoveries are unlikely at this point, further research is still required to improve efficiencies and drive down costs for wind to compete on an unsubsidized basis. Specifically, one area of improvement involves limiting turbine-to-turbine interactions at wind farms resulting from wake effects. To optimize turbine layouts and controls, computational fluid dynamics models of wind turbine wake dynamics must be developed and then verified using experimental data. With the ability to sample winds over large areas at high temporal and spatial resolution, remote sensing technology is particularly well-suited for the purpose of model verification.

The work presented here has demonstrated a procedure for quantifying wind turbine wake characteristics, including the velocity deficit, the extent of the wake boundary, and the location of the wake centerline. The methodology is intended to be general, in that it can be applied to extract wake characteristics from remote sensor measurements, as well as computational output. Here, experimental results were compared to a large eddy simulation (LES) of a turbine operating in the stable boundary layer using the actuator disk parameterization in the Weather Research and Forecasting (WRF) Model, and simulations showed good agreement with the observations. Continuing work in this area will help lead to improved turbine siting and controls at wind farms, with the ultimate goal being to limit turbine-to-turbine

interactions, thus optimizing plant power performance and minimizing the cost of energy.

References

Advanced Research Projects Agency-Energy, 2013. [Available online at http://arpa-e.energy.gov/]

Aitken, M. L., M. E. Rhodes, and J. K. Lundquist, 2012: Performance of a wind-profiling lidar in the region of wind turbine rotor disks. *J. Atmos. Ocean. Tech.*, 29, 347–355.

Aitken, M. L., R. M. Banta, Y. L. Pichugina, and J. K. Lundquist, 2014a: Quantifying wind turbine wake characteristics from scanning remote sensor data. *J. Atmos. Ocean. Tech.*, 31, 765–787.

Aitken, M. L., and J. K. Lundquist, 2014: Utility-scale wind turbine wake characterization using nacelle-based long-range scanning lidar. *J. Atmos. Ocean. Tech.*, doi:10.1175/JTECH-D-13-00218.1, in press.

Aitken, M. L., B. Kosović, J. D. Mirocha, and J. K. Lundquist, 2014b: Large eddy simulation of wind turbine wake dynamics in the stable boundary layer using the Weather Research and Forecasting Model. *J. Renew. Sust. Energ.*, in review.

Albers, A. and A. W. Janssen, 2008: Evaluation of Windcube. Deutsche WindGuard Consulting GmbH, Internal Project no. VC 08007, Report no. PP 08007. [Available online at: http://www.leosphere.com/file/deusche_windguard_report_windcube_evaluation.pdf]

Aldy, J. E., E. Ley, and I. Parry, 2008. A tax-based approach to slowing global climate change. *Natl. Tax J.*, 56, 493–517.

Alemany, J.,2013: Military readies to integrate women into combat. *CBS News*, 29 June. [Available online at http://www.cbsnews.com/8301-201_162-57591624/]

Alfredsson, P.-H., and J.-Å. Dahlberg, 1981: Measurements of wake interaction effects on the power output from small wind turbine models. The Aeronautical Research Institute of Sweden, Technical Note FFA HU-2189, 58 pp.

American College and University Presidents' Climate Commitment, 2013. [Available online at http://www.presidentsclimatecommitment.org/]

American Council on Renewable Energy and Advanced Energy Economy, 2012: U.S. Department of Defense & Renewable Energy: An Industry Helping the Military Meet Its Strategic Energy Objectives, 9 pp. http://www.acore.org/wp-content/uploads/2012/01/DoD-Renewable-Energy-Primer.pdf

Ammara, I., C. Leclerc, and C. Masson, 2002: A viscous three-dimensional method for the aerodynamic analysis of wind farms. *J. Sol. Energ.-T. ASME*, 124, 345–356.

Andreas, E. L., 1988: Estimating C_n^2 over snow and sea ice from meteorological data. *J. Opt. Soc. Amer. A*, 5 (4), 481–495.

Ansar, A., B. Caldecott, and J. Tilbury, 2013: Stranded assets and the fossil fuel divestment campaign: what does divestment mean for the valuation of fossil fuel assets? Stranded Assets Programme, Smith School of Enterprise and the Environment, University of Oxford, 80 pp.

Augustine, N., U. Burns, J. Doerr, B. Gates, C. Holliday, J. Immelt, and T. Linebarger, 2011: Catalyzing American Ingenuity: The Role of Government in Energy Innovation. American Energy Innovation Council, 37 pp.

Archer, C. L., S. Mirzaeisefat, and S. Lee, 2013: Quantifying the sensitivity of wind farm performance to array layout options using large-eddy simulation. *Geophys. Res. Lett.*, 40, 4963–4970.

Baker, R. W., and S. N. Walker, 1984: Wake measurements behind a large horizontal axis wind turbine generator. *Sol. Energy*, 33, 5–12.

Banta, R. M., L. D. Olivier, W. D. Neff, D. H. Levinson, and D. Ruffieux, 1995: Influence of canyon-induced flows on flow and dispersion over adjacent plains. *Theor. Appl. Climatol.*, 52, 27–42.

Banta, R. M., L. D. Olivier, P. H. Gudiksen, and R. Lange, 1996: Implications of small-scale flow features to modeling dispersion over complex terrain. *J. Appl. Meteorol.*, 35, 330–342.

Banta, R. M., R. K. Newsom, J. K. Lundquist, Y. L. Pichugina, R. L. Coulter, and L. Mahrt, 2002: Nocturnal low-level jet characteristics over Kansas during CASES-99. *Bound.-Lay. Meteorol.*, 105, 221–252.

Barthelmie, R. J., L. Folkerts, F. T. Ormel, P. Sanderhoff, P. J. Eecen, O. Stobbe, and N. M. Nielsen, 2003: Offshore wind turbine wakes measured by sodar. *J. Atmos. Ocean. Tech.*, 20, 466–477.

Barthelmie, R. J., L. Folkerts, G. C. Larsen, K. Rados, S. C. Pryor, S. T. Frandsen, B. Lange, and G. Schepers, 2006: Comparison of wake model simulations with offshore wind turbine wake profiles measured by sodar. *J. Atmos. Ocean. Tech.*, 23, 888–901.

Barthelmie, R. J., S. T. Frandsen, N. M. Nielsen, S. C. Pryor, P.-E. Rethore, and H. E. Jørgensen, 2007: Modelling and measurements of power losses and turbulence intensity in wind turbine wakes at Middelgrunden offshore wind farm. *Wind Energy*, 10, 217–228.

Barthelmie, R. J., S. C. Pryor, S. T. Frandsen, K. S. Hansen, J. G. Schepers, K. Rados, W. Schlez, A. Neubert, L. E. Jensen, and S. Neckelmann, 2010: Quantifying the impact of wind turbine wakes on power output at offshore wind farms. *J. Atmos. Ocean. Tech.*, 27, 1302–1317.

Barthelmie, R. J., and L. E. Jensen, 2010: Evaluation of wind farm efficiency and wind turbine wakes at the Nysted offshore wind farm. *Wind Energy*, 13, 573–586.

Basu, S., and F. Porté-Agel, 2006: Large-eddy simulation of stably stratified atmospheric boundary layer turbulence: a scale-dependent dynamic modeling approach. *J. Atmos. Sci.*, 63, 2074–2091.

Basu, S., A. A. M. Holtslag, B. J. H. Van de Wiel, A. F. Moene, and G.-J. Steeneveld, 2008: An inconvenient "truth" about using sensible heat flux as a surface boundary condition in models under stably stratified regimes. *Acta Geophys.*, 56, 88–99.

Beck, F., and E. Martinot, 2004: Renewable energy policies and barriers. *Encyclopedia of Energy*, 5, 365–383.

Bento, A., R. Kanbur, and B. Leard 2012: Super-Additionality: A Neglected Force in Markets for Carbon Offsets. Center for Economic and Policy Research Discussion Paper 8952, 18 pp.

Bingöl, F., J. Mann, G. C. Larsen, 2010: Light detection and ranging measurements of wake dynamics part I: one-dimensional scanning. *Wind Energy*, 13, 51–61.

Blackadar, A. K., 1957: Boundary layer wind maxima and their significance for the growth of nocturnal inversions. *B. Am. Meteorol. Soc.*, 38, 283–290.

Blumen, W., R. Banta, S. P. Burns, D. C. Fritts, R. Newsom, G. S. Poulos, and J. Sun, 2001: Turbulence statistics of a Kelvin-Helmholtz billow event observed in the night-time boundary layer during the Cooperative Atmosphere-Surface Exchange Study field program. *Dynam. Atmos. Oceans*, 34, 189–204.

Bonner, W. D., 1968: Climatology of the low level jet. *Mon. Wea. Rev.*, 96, 833–850.

Boquet, M., P. Callard, N. Deve, and E. G. Osler, 2010: Return on investment of a lidar remote sensing device. *DEWI Magazin*, 37, 56–61.

Box, G. E. P., J. S. Hunter, and W. G. Hunter, 2005: *Statistics for Experimenters.* Wiley-Interscience, 664 pp.

BP, 2013: BP Statistical Review of World Energy, 45 pp.

Cariou, J. P., 2011: Pulsed lidars. Risø Rep. Risø-I-3184(EN), 17 pp.

Cariou, J. P., L. Sauvage, S. Lolli, R. Parmentier, M. Boquet, and S. Loaec, 2009: Planetary boundary layer dynamic measurements with new compact long range wind lidar Windcube WLS70. Extended abstract, *89th American Meteorological Society Annual Meeting*, Phoenix, AZ, Amer. Meteor. Soc. [Available online at: http://ams.confex.com/ams/89annual/techprogram/paper_149827.htm]

Carr, G., 2012: Sunny uplands. *The Economist*, 21 November.

Chapman, A. W., 2008: Mixed-Gender Basic Training: The U.S. Army Experience, 1973–2004. U.S. Army Training and Doctrine Command, 197 pp.

Charles, L. A., S. Chaw, V. Vladutescu, Y. Wu, F. Moshary, B. Gross, S. D. Gedzelman, S. Ahmed, 2007: Application of CCNY lidar and ceilometers to the study of aerosol transport and $PM_{2.5}$ monitoring. Extended abstract, *87th American*

Meteorological Society Annual Meeting, San Antonio, TX, Amer. Meteor. Soc. [Available online at: http://ams.confex.com/ams/87ANNUAL/techprogram/paper_119919.htm]

Chow, F. K., R. L. Street, M. Xue, and J. H. Ferziger, 2005: Explicit filtering and reconstruction turbulence modeling for large-eddy simulation of neutral boundary layer flow. *J. Atmos. Sci.*, 62, 2058–2077.

Churchfield, M. J., S. Lee, J. Michalakes, and P. J. Moriarty, 2012: A numerical study of the effects of atmospheric and wake turbulence on wind turbine dynamics. *J. Turbul.*, 13, 1–32.

City of Boulder, 2013: Boulder Climate Action Plan. [Available online at https://bouldercolorado.gov/climate]

Clifton, A., and J. K. Lundquist, 2012: Data clustering reveals climate impacts on local wind phenomena. *J. Appl. Meteorol. Clim.*, 51, 1547–1557.

Clive, P. J. M., I. Dinwoodie, and F. Quail, 2011: Direct measurement of wind turbine wakes using remote sensing. *Proc. EWEA 2011*, Brussels, Belgium, European Wind Energy Association, 662.

Coase, R., 1960: The problem of social cost. *J. Law Econ.*, 3, 1–44.

Cowen, T., 1988: *Public Goods and Market Failures*. George Mason University Press, 385 pp.

Crespo, A., J. Hernandez, E. Fraga, and C. Andreu, 1988: Experimental validation of the UPM computer code to calculate wind turbine wakes and comparison with other models. *J. Wind Eng. Ind. Aerod.*, 27, 77–88.

Database of State Incentives for Renewables and Efficiency, 2013. [Available online at http://www.dsireusa.org/]

David Gardiner & Associates, 2012: Power Forward: Why the World's Largest Companies Are Investing in Renewable Energy, 46 pp.

Department of Defense, 2010: Quadrennial Defense Review Report, 105 pp.

Dinan, T., and P. Webre, 2012: Federal Financial Support for the Development and Production of Fuels and Energy Technologies. Congressional Budget Office Issue Brief, 10 pp.

The Economist, 2006: Dismal calculations: the economics of living with climate change—or mitigating it. *The Economist*, 7 September.

El Kasmi, A., and C. Masson, 2008: An extended k-ε model for turbulent flow through horizontal-axis wind turbines. *J. Wind Eng. Ind. Aerod.*, 96, 103–122.

Elliott, D. L., and J. C. Barnard, 1990: Observations of wind turbine wakes and surface roughness effects on wind flow variability. *Sol. Energy*, 45, 265–283.

Elliott, D., M. Schwartz, and G. Scott, 2009: Wind shear and turbulence profiles at elevated heights: Great Lakes and Midwest sites. NREL Rep. NREL/PO-500-45455, 1 p.

Emeis, S., 2013: *Wind Energy Meteorology*. Springer, 196 pp.

España, G. S. Aubrun, S. Loyer, and P. Devinant, 2011: Spatial study of the wake meandering using modelled wind turbines in a wind tunnel. *Wind Energy*, 14, 923–937.

Executive Office of the President, 2013: The President's Climate Action Plan. 21 pp.

Fitch, A. C., J. B. Olson, J. K. Lundquist, J. Dudhia, A. K. Gupta, J. Michalakes, and I. Barstad, 2012: Local and mesoscale impacts of wind farms as parameterized in a mesoscale NWP model. *Mon. Weather Rev.*, 140, 3017–3038.

Fitch, A. C., J. K. Lundquist, and J. B. Olson, 2013: Mesoscale influences of wind farms throughout a diurnal cycle. *Mon. Weather Rev.*, 141, 2173–2198.

Foote, G. B. and P. S. du Toit, 1969: Terminal velocity of raindrops aloft. *J. Appl. Meteor.*, 8, 249–253.

Fossil Free, 2013: Commitments. [Available online at http://gofossilfree.org/commitments/]

Frandsen, S., R. Barthelmie, S. Pryor, O. Rathmann, S. Larsen, J. Højstrup, and M. Thøgersen, 2006: Analytical modelling of wind speed deficit in large offshore wind farms. *Wind Energy*, 9, 39–53.

Frehlich, R., 1996: Simulation of coherent Doppler lidar performance in the weak-signal regime. *J. Atmos. Oceanic Technol.*, 13, 646–658.

Frehlich, R., Y. Meillier, M. L. Jensen, and B. Balsley, 2006: Measurements of boundary layer profiles in an urban environment. *J. Appl. Meteorol. Clim.*, 45, 821–837.

Frehlich, R., 2013: Scanning Doppler lidar for input into short-term wind power forecasts. *J. Atmos. Oceanic Technol.*, 30, 230–244.

Friedrich, K., J. K. Lundquist, M. Aitken, E. A. Kalina, R. F. Marshall, 2012: Stability and turbulence in the atmospheric boundary layer: a comparison of remote sensing and tower observations. *Geophys. Res. Lett.*, 39, L03801, doi:10.1029/2011GL050413.

Fujii, T. and T. Fukuchi, 2005: *Laser Remote Sensing*. Taylor & Francis Group, 912 pp.

Garamone, J., 2008: Former chairman discusses Truman's 1948 integration order. *American Forces Press Service*, 28 July. [Available online at http://www.defense.gov/news/NewsArticle.aspx?ID=50623]

Goldenburg, S., 2013: Voters think Republican climate dissenters crazy, bipartisan poll finds. *The Guardian*, 24 July. [Available online at http://www.theguardian.com/world/2013/jul/25/us-politics-climate-change-scepticism]

Gomes, L., M. Mallet, J. C. Roger, and P. Dubuisson, 2008: Effects of the physical and optical properties of urban aerosols measured during the CAPITOUL summer campaign on the local direct radiative forcing. *Meteor. and Atmos. Phys.*, 102, 289–306.

Gottschall, J. and M. Courtney, 2010: Verification test for three WindCube WLS7 LiDARs at the Høvsøre test site. Risø-R-Report 1732(EN). [Available online at: http://130.226.56.153/rispubl/reports/ris-r-1732.pdf]

Goulder, L.H., and A. Schein, 2013: Carbon Taxes vs. Cap and Trade: A Critical Review. National Bureau of Economic Research, Working Paper 19338, 38 pp.

Grund, C. J., R. M. Banta, J. L. George, J. N. Howell, M. J. Post, R. A. Richter, and A. M. Weickmann, 2001: High-resolution Doppler lidar for boundary layer and cloud research. *J. Atmos. Ocean. Tech.*, 18, 376–393.

Haines, R. S., D. J. Milborrow, D. I. Page, A. D. Scott, W. G. Stevenson and G. J. Taylor, 1986: Wake interactions between the Holden HWP-300 and the WEG MS-1 wind turbine generators on Orkney, U.K. *European Wind Energy Association Conf. and Exhibition*, Rome, Italy, European Wind Energy Association, 435–455.

Hansen, K. S., R. J. Barthelmie, L. E. Jensen, and A. Sommer, 2012: The impact of turbulence intensity and atmospheric stability on power deficits due to wind turbine wakes at Horns Rev wind farm. *Wind Energy*, 15, 183–196.

Harris, M., M. Hand, and A. Wright, 2006: Lidar for turbine control. NREL Technical Report NREL/TP-500-39154, 47 pp.

Heeter, J., P. Armstrong, and L. Bird, 2012: Market brief: status of the voluntary renewable energy certificate market (2011 data). National Renewable Energy Laboratory Tech. Rep. NREL/TP-6A20-56128, 27 pp.

Helmis, C. G., K. H. Papadopoulos, D. N. Asimakopoulos, P. G. Papageorgas, and A. T. Soilemes, 1995: An experimental study of the near-wake structure of a wind turbine operating over complex terrain. *Sol. Energy*, 54, 413–428.

Hirth, B. D., J. L. Schroeder, W. S. Gunter, and J. G. Guynes, 2012: Measuring a utility-scale turbine wake using the TTUKa mobile research radars. *J. Atmos. Ocean. Tech.*, 29, 765–771.

Hirth, B. D., and J. L. Schroeder, 2013: Documenting wind speed and power deficits behind a utility-scale wind turbine. *J. Appl. Meteorol. Clim.* 52, 39–46.

Högström, U., D. N. Asimakopoulos, H. Kambezidis, C. G. Helmis, and A. Smedman, 1988: A field study of the wake behind a 2 MW wind turbine. *Atmos. Environ.*, 22, 803–820.

Holt, C., W. Shobe, D. Burtraw, K. Palmer, and J. Goeree, 2007: Auction Design for Selling CO_2 Emissions Allowances Under the Regional Greenhouse Gas Initiative. New

York State Energy Research Development Authority. [Available online at http://www.rggi.org/docs/rggi_auction_final.pdf]

Im, J-S, V. K. Saxena and B. N. Wenny, 2001: An assessment of hygroscopic growth factors for aerosols in the surface boundary layer for computing direct radiative forcing. *J. Geophys. Res.*, 106 (D17), 20213–20224.

Interagency Working Group on Social Cost of Carbon, 2013: Technical Support Document: Technical Update of the Social Cost of Carbon for Regulatory Impact Analysis Under Executive Order 12866. United States Government, 21 pp. http://www.whitehouse.gov/sites/default/files/omb/inforeg/social_cost_of_carbon_for_ria_2013_update.pdf

International Electrotechnical Commission (IEC), 2005: Wind turbines—Part 12-1: Power performance measurements of electricity producing wind turbines. IEC 61400-12-1 International Standard, 92 pp.

International Energy Agency, 2009: World Energy Outlook 2009. 696 pp.

International Energy Agency, 2011: Deploying Renewables 2011: Best and Future Policy Practice. 186 pp. http://www.iea.org/publications/freepublications/publication/Deploying_Renewables2011.pdf

Iungo, G. V., Y.-T. Wu, and F. Porté-Agel, 2013: Field measurements of wind turbine wakes with lidars. *J. Atmos. Ocean. Tech.*, 30, 274–287.

Jacobson, M. Z., 2009: Review of solutions to global warming, air pollution, and energy security. *Energ. Environ. Sci.*, 2, 148–173.

Jenkins, J., D. Swezey, Y. Borofsky, H. Aki, Z. Arnold, G. Bennett, C. Knight, A. Lin, T. Norris, T. Walton, and A. Zemel, 2010: Where Good Technologies Come From: Case Studies in American Innovation. Breakthrough Institute, 36 pp.

Johansson, P. B., W. K. George, and M. J. Gourlay, 2003: Equilibrium similarity, effects of initial conditions and local Reynolds number on the axisymmetric wake. *Phys. Fluids*, 15, 603–617.

Johnson, W., and N. Kelley, 2000: Design specifications for the development of the initial validation software (version 3.0) for processing of NWTC 80-meter meteorological tower data. National Renewable Energy Laboratory Tech. Rep. NREL/TP-500-27104, 92 pp. [Available online at http://www.nrel.gov/docs/fy00osti/27104.pdf]

Justus, C. G., W. R. Hargraves, A. Mikhail, and D. Graber, 1978: Methods for estimating wind speed frequency distributions. *J. Appl. Meteorol.*, 17, 350–353.

Kambezidis, H. D., D. N. Asimakopoulos, and C. G. Helmis, 1990: Wake measurements behind a horizontal-axis 50 kW wind turbine. *Solar Wind Tech.*, 7, 177–184.

Käsler, Y., S. Rahm, R. Simmet, and M. Kühn, 2010: Wake measurements of a multi-MW wind turbine with coherent long-range pulsed Doppler wind lidar. *J. Atmos. Ocean. Tech.*, 27, 1529–1532.

Kelley, N. D., B. J. Jonkman, and G. N. Scott, 2006: The Great Plains turbulence environment: its origins, impact and simulation. National Renewable Energy Laboratory Conference Paper, NREL/CP-500-40176.

Kleinbaum, D. G., L. L. Kupper, A. Nizam, K. E. Muller, 2007: *Applied Regression Analysis and Other Multivariable Methods*. 4th ed. Duxbury Press, 928 pp.

Komor, P., 2004: *Renewable Energy Policy*. Diebold Institute for Public Policy Studies, 182 pp.

Kosmo, M., 1987: *Money to Burn? The High Costs of Energy Subsidies*. World Resources Institute, 68 pp.

Kosović, B., 1997: Subgrid-scale modelling for the large-eddy simulation of high-Reynolds-number boundary layers. *J. Fluid Mech.*, 336, 151–182.

Kosović, B., and J. A. Curry, 2000: A large eddy simulation study of a quasi-steady, stably stratified atmospheric boundary layer. *J. Atmos. Sci.*, 57, 1052–1068.

LaMonica, M., 2013: Xcel Energy buying utility-scale solar at prices competitive with natural gas. *Greentech Media*, 2 October. [Available online at http://www.greentechmedia.com/articles/read/xcel-energy-buys-utility-scale-solar-for-less-than-natural-gas]

Larsen, G. C., 2001: Offshore fatigue design turbulence. *Wind Energy*, 4, 107–120.

Lawson, J. K. and C. J. Carrano, 2006: Using historic models of C_n^2 to predict r_0 and regimes affected by atmospheric turbulence for horizontal, slant, and topological paths. *Proc. SPIE Optics and Photonics*, San Diego, CA, SPIE, 6303-04. [Available online at https://e-reports-ext.llnl.gov/pdf/335213.pdf]

Levin, K., B. Cashore, S. Bernstein, and G. Auld, 2012: Overcoming the tragedy of super wicked problems: constraining our future selves to ameliorate global climate change. *Policy Sci.*, 45, 123–152.

Lindelöw, P., 2007: Fiber based coherent lidars for remote wind sensing. Ph.D. dissertation, Technical University of Denmark, 186 pp.

Luderer, G., R. C. Pietzcker, C. Bertram, E. Kriegler, M. Meinshausen, and O. Edenhofer, 2013: Economic mitigation challenges: how further delay closes the door for achieving climate targets. *Environmental Research Letters,* 8, 034033, doi:10.1088/1748-9326/8/3/034033

Lundquist, J. K., and J. D. Mirocha, 2008: Interaction of nocturnal low-level jets with urban geometries as seen in Joint Urban 2003 data. *J. Appl. Meteorol. Clim.*, 47, 44–58.

Magnusson, M., and A. S. Smedman, 1994: Influence of atmospheric stability on wind turbine wakes. *Wind Eng.*, 18, 139–151.

Magnusson, M., 1999: Near-wake behaviour of wind turbines. *J. Wind Eng. Ind. Aerod.*, 80, 147–167.

Mahrt, L., 2011: Surface wind direction variability. *J. Appl. Meteorol. Clim.*, 50, 144–152.

Mahrt, L., 2014: Stably stratified atmospheric boundary layers. *Annu. Rev. Fluid Mech.*, 46, 23–45.

Manwell, J. F., J. G. McGowan, and A. L. Rogers, 2010: *Wind Energy Explained: Theory, Design, and Application.* Wiley, 704 pp.

Masseran, N., A. M. Razali, K. Ibrahim, and M. T. Latif, 2013: Fitting a mixture of von Mises distributions in order to model data on wind direction in Peninsular Malaysia. *Energ. Convers. Manage.*, 72, 94–102.

McCarthy, J. E., 2013: EPA Standards for Greenhouse Gas Emissions from Power Plants: Many Questions, Some Answers. Congressional Research Service, 16 pp.

Metcalf, G. E., 2009: Market-based policy options to control U.S. greenhouse gas emissions. *J. Econ. Perspect.*, 23, 5–27.

Metz, B., O. R. Davidson, P. R. Bosch, R. Dave, L. A. Meyer (Eds.), 2007: Climate Change 2007: Mitigation of Climate Change. Contribution of Working Group III to the Fourth Assessment Report of the Intergovernmental Panel on Climate Change. Cambridge University Press, 851 pp.

Meyers, J., and C. Meneveau, 2012: Optimal turbine spacing in fully developed wind farm boundary layers. *Wind Energy*, 15, 305–317.

Mihoces, G., 2013: Go green! Sports stadiums save energy. *USA Today*, 21 April.

Mikkelsen, R., 2003: Actuator disc methods applied to wind turbines. Ph.D. dissertation, Technical University of Denmark.

Mirocha, J. D., and B. Kosović, 2010: A large-eddy simulation study of the influence of subsidence on the stably stratified atmospheric boundary layer. *Bound.-Lay. Meteorol.*, 134, 1–21.

Mirocha, J. D., J. K. Lundquist, and B. Kosović, 2010: Implementation of a nonlinear subfilter turbulence stress model for large-eddy simulation in the Advanced Research WRF Model. *Mon. Weather Rev.*, 138, 4212–4228.

Mirocha, J. D., B. Kosović, M. L. Aitken, and J. K. Lundquist, 2014: Implementation of a generalized actuator disk wind turbine model into the Weather Research and Forecasting Model for large-eddy simulation applications. *J. Renew. Sust. Energ.*, 6, 013104-1–013104-19.

Mufson, S., 2012: With fiscal cliff looming, carbon tax getting closer look. *The Washington Post*, 9 November.

Natural Marketing Institute, 2011: Consumer attitudes about renewable energy: trends and regional differences. National Renewable Energy Laboratory Subcontract Report NREL/SR-6A20-50988, 20 pp.

Newsom, R. K., and R. M. Banta, 2003: Shear-flow instability in the stable nocturnal boundary layer as observed by Doppler lidar during CASES-99. *J. Atmos. Sci.*, 60, 16–33.

Newsom, R. K., D. Ligon, R. Calhoun, R. Heap, E. Cregan, and M. Princevac, 2005: Retrieval of microscale wind and temperature fields from single- and dual-Doppler lidar data. *J. Appl. Meteorol.*, 44, 1324–1345.

Office of Energy Efficiency and Renewable Energy, 2013. [Available online at http://energy.gov/eere/office-energy-efficiency-renewable-energy]

Pachauri, R. K., and A. Reisinger (Eds.), 2007: Climate Change 2007: Synthesis Report. Contribution of Working Groups I, II, and III to the Fourth Assessment Report of the Intergovernmental Panel on Climate Change. Cambridge University Press, 104 pp.

Park, J., S. Basu, and L. Manuel, 2014: Large-eddy simulation of stable boundary layer turbulence and estimation of associated wind turbine loads. *Wind Energy*, 17, 359–384.

Parry, M. L., O. F. Canziani, J. P. Palutikof, P. J. van der Linden, and C. E. Hanson (Eds.), 2007: Climate Change 2007: Impacts, Adaptation, and Vulnerability. Contribution of Working Group II to the Fourth Assessment Report of the Intergovernmental Panel on Climate Change. Cambridge University Press, 976 pp.

Pichugina, Y. L., R. M. Banta, W. A. Brewer, S. P. Sandberg, and R. M. Hardesty, 2012: Doppler lidar-based wind-profile measurement system for offshore wind-energy and other marine boundary layer applications. *J. Appl. Meteor. Climatol.*, 51, 327–349.

Pielke, Jr., R., 2010: *The Climate Fix*. Basic Books, 276 pp.

Porté-Agel, F., Y.-T. Wu, H. Lu, and R. J. Conzemius, 2011: Large-eddy simulation of atmospheric boundary layer flow through wind turbines and wind farms. *J. Wind Eng. Ind. Aerod.*, 99, 154–168.

Porter, E., 2013a: For insurers, no doubts on climate change. *The New York Times*, 14 May.

Porter, E., 2013b: Counting the cost of fixing the future. *The New York Times*, 10 September.

Proctor, C., 2012: EPA approves Colorado's Clean Air-Clean Jobs Act, haze plan. *Denver Business Journal*, 11 September. [Available online at http://www.bizjournals.com/denver/news/2012/09/11/epa-approves-clean-airclean-jobs-act.html]

Rajewski, D. A., E. S. Takle, J. K. Lundquist, S. Oncley, J. H. Prueger, T. W. Horst, M. E. Rhodes, R. Pfeiffer, J. L. Hatfield, K. K. Spoth, and R. K. Doorenbos, 2013: Crop Wind Energy Experiment (CWEX): observations of surface-layer, boundary layer, and mesoscale interactions with a wind farm. *B. Am. Meteorol. Soc.*, 94, 655–672.

Reinsurance Association of America, 2008: Climate Change Policy. [Available online at http://www.forest-trends.org/documents/files/doc_3643.pdf]

Revkin, A., 2009: Industry ignored its scientists on climate. *The New York Times*, 23 April.

Roberts, D., 2012: Why the military is trying to reduce its fossil fuel use. *Grist*, 30 July. [Available online at http://grist.org/climate-energy/why-the-military-is-trying-to-reduce-its-fossil-fuel-use/]

Roberts, D., 2013a: Ending the stupid technology innovation vs. deployment fight once and for all. *Grist*, 11 March. [Available online at http://grist.org/climate-energy/ending-the-stupid-technology-innovation-vs-deployment-fight-once-and-for-all/]

Roberts, D., 2013b: Hope and fellowship. *Grist*, 30 August. [Available online at http://grist.org/climate-energy/hope-and-fellowship/]

Rudolf, J. C., 2011: News Corporation is carbon neutral, Murdoch declares. *The New York Times*, 4 March.

Rye, B. J., and R. M. Hardesty, 1993: Discrete spectral peak estimation in incoherent backscatter heterodyne lidar. I: Spectral accumulation and the Cramer-Rao lower bound. *IEEE Trans. Geosci. Remote Sens.*, 31, 16–27.

Saiki, E., C. Moeng, and P. Sullivan, 2000: Large-eddy simulation of the stably stratified planetary boundary layer. *Bound.-Lay. Meteorol.*, 95, 1–30.

Sathe, A., J. Mann, T. Barlas, W. A. A. M. Bierbooms, and G. J. W. van Bussel, 2013: Influence of atmospheric stability on wind turbine loads. *Wind Energy*, 16, 1013–1032.

Scamarock, W. C., J. B. Klemp, J. Dudhia, D. O. Gill, D. M. Barker, M. G. Duda, X.-Y. Huang, W. Wang, and J. G. Powers, 2008: A description of the advanced research WRF version 3. National Center for Atmospheric Research Technical Note, NCAR/TN-475+STR.

Sharma, R., Y. Pervez, and S. Pervez, 2005: Seasonal evaluation and spatial variability of suspended particulate matter in the vicinity of a large coal-fired power station in India—a case study. *Environ. Monit. Assess.*, 102, 1–13.

Shear, M. D., 2013: Administration presses ahead with limits on emissions from power plants. *The New York Times*, 19 September.

Shellenberger, M., T. Nordhaus, A. Trembath, and J. Jenkins, 2012: Where the Shale Gas Revolution Came From: Government's Role in the Development of Hydraulic Fracturing in Shale. Breakthrough Institute, 25 pp.

Sherlock, M. F., 2011: Energy Tax Policy: Historical Perspectives on and Current Status of Energy Tax Expenditures. Congressional Research Service, 36 pp.

Smalikho, I. N., V. A. Banakh, Y. L. Pichugina, W. A. Brewer, R. M. Banta, J. K. Lundquist, and N. D. Kelley, 2013: Lidar investigation of atmosphere effect on a wind turbine wake. *J. Atmos. Ocean. Tech.*, 30, 2554–2570.

Sonnenschein, C. M., and F. A. Horrigan, 1971: Signal-to-noise relationships for coaxial systems that heterodyne backscatter from the atmosphere. *Appl. Opt.*, 10, 1600–1604.

Stehr, N., and H. von Storch, 2005: Introduction to papers on mitigation and adaptation strategies for climate change: protecting nature from society or protecting society from nature? *Environ. Sci. Policy*, 8, 537–540.

Stern, N., 2006: Stern Review on the Economics of Climate Change. HM Treasury, 579 pp.

Stull, R. B., 1988: *An Introduction to Boundary Layer Meteorology*. Kluwer Academic Publishers, 666 pp.

Swanson, R. M., 2006: A vision for crystalline silicon photovoltaics. *Prog. Photovoltaics*, 14, 443–453.

Taschini, L., S. Dietz, and N. Hicks, 2013: Carbon tax v cap-and-trade: which is better? *The Guardian*, 31 January.

Tillemann, L., F. Beck, J. Brodrick, A. Brown, D. Feldman, T. Nguyen, J. Ward, 2013: Revolution Now: The Future Arrives for Four Clean Energy Technologies. U.S. Department of Energy, 10 pp.

Tol, R. S. J., 2009: The economic effects of climate change. *J. Econ. Perspect.*, 23, 29–51.

Trujillo, J.-J., F. Bingöl, G. C. Larsen, J. Mann, and M. Kühn, 2011: Light detection and ranging measurements of wake dynamics part II: two-dimensional scanning. *Wind Energy*, 14, 61–75.

Tucker, S. C., W. A. Brewer, R. M. Banta, C. J. Senff, S. P. Sandberg, D. C. Law, A. M. Weickmann, and R. M. Hardesty, 2009: Doppler lidar estimation of mixing height using turbulence, shear, and aerosol profiles. *J. Atmos. Ocean. Tech.*, 26, 673–688.

Tunick, A, 2003: CN2 model to calculate the micrometeorological influences on the refractive index structure parameter. *Environmental Modelling & Software*, 18, 165–171.

U.S. Energy Information Administration, 2013a: Annual Energy Outlook 2013 with Projections to 2040. DOE/EIA-0383, 233 pp.

U.S. Energy Information Administration, 2013b: Electric Power Monthly with Data for August 2013. 189 pp.

U.S. Energy Information Administration, 2013c: Status of electricity restructuring by state. [Available online at http://www.eia.gov/electricity/policies/restructuring/restructure_elect.html]

U.S. Environmental Protection Agency, 2010: Our nation's air: status and trends through 2008. Office of Air Quality Planning and Standards EPA Publication No. EPA-454/R-09-002, 54 pp.

U.S. Environmental Protection Agency, 2011: Assessing the multiple benefits of clean energy: a resource for states. EPA-430-R-11-014, 190 pp.

U.S. Environmental Protection Agency, 2013: Climate Change Action Plans. [Available online at http://epa.gov/statelocalclimate/state/state-examples/action-plans.html]

Vanderwende, B. J., and J. K. Lundquist, 2012: The modification of wind turbine performance by statistically distinct atmospheric regimes. *Environ. Res. Lett.*, 7, 034035-1–034035-7.

Vermeer, L. J., J. N. Sørensen, and A. Crespo, 2003: Wind turbine wake aerodynamics. *Prog. Aerosp. Sci.*, 39, 467–510.

Wagner, R., I. Antoniou, S. M. Pedersen, M. S. Courtney, and H. E. Jørgensen, 2009: The influence of the wind speed profile on wind turbine performance measurements. *Wind Energy*, 12, 348–362.

Walmart, 2013: Environmental Sustainability. [Available online at http://corporate.walmart.com/global-responsibility/environmental-sustainability/environmental-sustainability]

Wang, U., 2012: Spain suspends clean power incentive program to rein in costs. *GigaOM*, 27 January. [Available online at http://gigaom.com/2012/01/27/spain-suspends-clean-power-incentive-program-to-reign-in-costs/]

Werner, C., 2005: Doppler wind lidar, *Lidar: Range-Resolved Optical Remote Sensing of the Atmosphere*, C. Weitkamp, Ed., Springer, 325–354.

Wharton, S., and J. K. Lundquist, 2012: Assessing atmospheric stability and its impacts on rotor-disk wind characteristics at an onshore wind farm. *Wind Energy*, 15, 525–546.

Wharton, S., and J. K. Lundquist, 2012: Atmospheric stability affects wind turbine power collection. *Environ. Res. Lett.*, 7, 014005-1–014005-9.

Wiser, R. and M. Bolinger, 2010: 2009 Wind technologies market report. NREL/TP-6A2-48666, 88 pp.

World Bank, 2009: World Development Report 2010: Development and Climate Change, 417 pp.

World Business Council for Sustainable Development, 2013. [Available online at http://www.wbcsd.org/home.aspx]

Wu, Y.-T., and F. Porté-Agel, 2011: Large-eddy simulation of wind-turbine wakes: evaluation of turbine parametrisations. *Bound.-Lay. Meteorol.*, 138, 345–366.

Wulfmeyer, V. and G. Feingold, 2000: On the relationship between relative humidity and particle backscattering coefficient in the marine boundary layer determined with differential absorption lidar. *J. Geophys. Res.*, 105 (D4), 4729–4741.

Yura, H. T., 1979: Signal-to-noise ratio of heterodyne lidar systems in the presence of atmospheric turbulence. *J. Modern Optics*, 26 (5), 627–644.

Zhou, B., and F. K. Chow, 2011: Large-eddy simulation of the stable boundary layer with explicit filtering and reconstruction turbulence modeling. *J. Atmos. Sci.*, 68, 2142–2155.

Zindler, E., M. Di Capua, S. Linder, J. Salvatore, C. Blanchard, A. Grace, A. Kim, A. Zamorano, D. Hostert, M. Taylor, C. Wilson, A. Cheung, S. Sun, T. Rowlands-Rees, A Izadi-Najafabadi, and C. McKerracher, 2013: Sustainable Energy in America 2013 Factbook. Bloomberg New Energy Finance, 94 pp.